Simulation of Neutron Radiation Effects in Silicon Avalanche Photodiodes

Thesis submitted for the degree of Doctor of Philosophy

by

Mark David Osborne

Faculty of Technology, Brunel University

November 2000

Abstract

A new one-dimensional device simulation package developed for the simulation of neutron radiation effects in silicon avalanche photodiodes is described. The software uses a finite difference technique to solve the time-independent semiconductor equations across a user specified structure. Impact ionisation and illumination are included, allowing accurate simulation with minimal assumptions about the device under investigation. The effect of neutron radiation damage is incorporated via the introduction of deep acceptor levels subject to Shockley-Read-Hall statistics.

Two models are presented. A reverse reach through model, based on the EG&G C30626E reverse reach through avalanche photodiode originally proposed for use in the CMS electromagnetic calorimeter, and a reach through model, based on widely available commerical devices. A short experimental study on two commercial silicon avalanche photodiodes, a C30719F reverse reach through APD and a C30916E reach through APD, is presented for comparison with the simulation data. To allow full comparison with the simulated predictions, the commercial devices were irradiated at the Rutherford Appleton Laboratory's ISIS facility.

The simulated data shows good qualitative agreement with the measurements performed on the commercial devices, quantitative predictions would require exact information about the doping profile. The characteristic behaviour of the devices is predicted over a wide range of conditions both before and after neutron irradiation. The effect of ionised deep acceptors in the bulk of the devices is investigated. The simulation package provides a useful tool for the analysis of semiconductor devices, particularly in areas where a non-ionising radiation damage is prevelent e.g. high energy physics, and provides a good basis for further development.

To my family

Acknowledgements

Firstly I would like to thank my supervisors, Peter Hobson and Steve Watts. I appreciate all their efforts, from start to end, in helping to get this work completed and especially the thesis written. Thanks also to PPARC for funding my Ph.D.

I would also like to thank all the other staff who have helped me along the way: Derek, Andrew, Chris ,Barry and of course Sabah!

A special mention to the people who kept me sane at the most insane times: Notably Karl (who I will ring one day), Kate, Mita, Babara, Max, Dave, Jane, Mabu, Hye, Paul and John.

Thankyou to all my family who have helped enormously, especially mum, dad, gran and grandad. An endless thankyou to Clare and the boys for keeping me smiling all the way through.

This thesis is dedicated to the memory of Leonard Childs.

Contents

1 Overview **1**

1.1 Introduction 1

1.1.1 Optical Photo-Detectors 1

1.1.2 The Photomultiplier Tube 2

1.2 PIN Photodiode 4

1.3 Avalanche Photodiode 6

1.3.1 High Energy Physics 8

1.4 The Compact Muon Solenoid Electromagnetic Calorimeter 8

1.4.1 Overview of CMS 8

1.4.2 The ECAL 9

1.4.3 Application of APDs 11

1.4.4 Introducing the Simulation 12

1.5 Overview of Thesis 13

2 APD Device Theory and Operation **15**

2.1 Introduction 15

2.2 The Semiconductor Equations 16

2.2.1 Introduction 16

2.2.2 The Current Equations 17

2.2.3 The Continuity Equations 19

2.2.4 The Poisson Equation 19

2.3 The PN Junction 20

2.3.1 Introduction 20

2.3.2 Thermal Generation and Recombination Processes 21
2.3.3 Indirect Recombination 22
2.3.4 Additional Generation and Recombination Processes 26
2.3.5 Impact Ionisation 26
2.3.6 Excess Noise 31
2.3.7 Ionisation Co-efficients 32
2.4 Photo-detection 32
2.4.1 Photoexcitation 32
2.5 Junction Photodiodes 33
2.5.1 PIN Photodiodes 34
2.5.2 Avalanche Photodiodes 34
2.5.3 Germanium Avalanche Photodiodes 34
2.5.4 Hetero-Junction Avalanche Photodiodes 35
2.5.5 Reach Through Avalanche Photodiodes 36
2.5.6 Reverse Reach Through Avalanche Photodiodes 38
2.6 Fast Neutron Radiation Damage 39
2.7 Macroscopic Effects in Silicon 40
2.8 Damage Mechanism 41
2.9 Annealing 44

3 Experimental Techniques **45**
3.1 Introduction 45
3.2 The Test System 45
3.2.1 Introduction 45
3.2.2 Temperature Control 46
3.2.3 Bias Control 48
3.2.4 Illumination 49
3.3 Experimental Procedures 53
3.3.1 Introduction 53
3.3.2 The Constant Illumination Gain 53

3.3.3 Photosensitivity 55
3.3.4 Excess Noise Factor 55
3.3.5 Errors 56
3.3.6 Post Irradiation 57

4 Simulation of Avalanche Photodiodes. 59

4.1 Introduction 60
4.2 APDSIM 61
4.2.1 Introduction 61
4.2.2 Semiconductor Equations 63
4.2.3 The One-Dimensional Grid 64
4.2.4 Grid Parameter Selection 64
4.2.5 Discretisation Error 67
4.2.6 Application of Finite Differences 67
4.2.7 Linearising the Discretised Equations 69
4.2.8 Solving the Matrix Equation 70
4.2.9 Initialising and Terminating the process 72
4.2.10 Impact Ionisation 75
4.2.11 Illumination 78
4.2.12 Neutron Radiation Damage 80
4.3 APDGAIN 82
4.3.1 Introduction 82
4.3.2 Multiplication Factor 83
4.3.3 Excess Noise Factor 84
4.4 DIFFUSE 85
4.4.1 Introduction 85
4.5 Simulation Limitations 86
4.5.1 Introduction 86
4.5.2 APDSIM 86
4.5.3 APDGAIN 87

4.5.4 DIFFUSE 88
4.6 Conclusions 88

5 Results **89**
5.1 Introduction 89
5.2 Pre-Irradiation 91
5.2.1 Introduction 91
5.2.2 Microscopic Features 92
5.2.3 Dark Current 99
5.2.4 Photocurrent 100
5.2.5 Gain 101
5.2.6 Excess Noise Factor 105
5.2.7 Photosensitivity 109
5.3 Post-Irradiation 112
5.3.1 Reach Through APD 112
5.3.2 Reverse Reach Through APD 119

6 Conclusions **128**

A **142**

B **146**

C **149**

List of Tables

1.1 Table showing typical values of gain and response time for a variety of semiconductor photo-detectors. 5
1.2 Table showing the properties of various scintillating media. 9
1.3 Table showing the desired and measured parameters of the candidate APDs for the CMS ECAL 12

2.1 Table showing the parameters used in the Chenowyth expression for the ionisation co-efficients. 27
2.2 Table showing the stated typical characteristics of the C30916E and C30719F APD at 22°C. 38

4.1 Table showing several types of semiconductor model 61
4.2 Table showing the convergence time and steps for various grid sizes . 66
4.3 Table showing the properties of the deep acceptor level used in the simulation. 81

5.1 Table showing the specifications of each of the diffused implants used to create the reach through model. 89
5.2 Table showing the specifications of each of the diffused implants used to create the reverse reach through APD model. 90

List of Figures

1.1 A figure showing the visible region of the electromagnetic spectrum. . 2
1.2 A schematic of a typical photomultiplier tube. 3
1.3 A simple diagram showing how the valence band electrons are excited into the conduction band by an incident photon. 5
1.4 A simple schematic of a typical silcon PIN photodiode. 6
1.5 A simple schematic of a typical silicon reach through avalanche photodiode. 7
1.6 A figure showing the CMS detector due to start running at the Large Hadron Collider at CERN in 2005. 10
1.7 A simple schematic showing the electric field profiles and gain regions of the EG&G reach through and reverse reach through APDs. 14

2.1 A simple diagram showing indirect recombination. 21
2.2 A simple diagram showing direct recombination. 22
2.3 A diagram showing the processes involved in indirect recombination. . 23
2.4 A band diagram showing the process of impact ionisation. 27
2.5 Figure showing the values of α_e and α_h calculated using the Chenowyth parameterisation. 28
2.6 A diagram showing the formation of an avalanche where k=0. 29
2.7 A diagram showing the formation of an avalanche where k$\neq$0. 30
2.8 A diagram showing the structure of a Germanium diffused avalanche photodiode. 35

2.9 A Schematic showing the structure of an InP-based SAGM avalanche photodiode. 36
2.10 A diagram showing the estimated structure of the C30916E APD used in the reach through APD model. 37
2.11 A diagram showing the estimated structure of the C30719F APD used in the reverse reach through APD model. 38
2.12 A simple schematic of the principal types of radiation induced damage to a semiconductor lattice. 42
2.13 A simple schematic showing the formation of a cluster of defects caused by an incident high energy neutron. 43

3.1 Diagram showing the layout of the APD test box. 46
3.2 Diagram showing the position of the LED and APD in relation to the Aluminium cooling block 47
3.3 Plot showing the short term temperature stability of the temperature control system 48
3.4 Schematic of the APD bias circuit. 49
3.5 Diagram showing the method used to mount the fibre optic cable . . 50
3.6 Schematic of the LED pulser circuit 51
3.7 Figure showing the variation of reach through APD photocurrent with bias. 54

4.1 Schematic of the interaction between the individual programs that are used in the simulation. 62
4.2 A schematic of the grid composition 64
4.3 Figure showing the potential variation at one grid point with increasing grid size. 66
4.4 Figure showing the mean relative shift in solution for each of the fundamental parameters as the grid size is increased from 500 to 3000 grid points. 68

4.5 A diagram showing how the solution procedure is organised. 74

4.6 Figure showing how the electric field is transformed from the half-points to the main grid points. 79

5.1 Doping profile used to simulate a silicon reach through APD. 90

5.2 Doping profile used to simulate a silicon reverse reach through APD. 91

5.3 Variation in free hole concentration with bias for the reach through model. 92

5.4 Variation in free electron concentration with bias for the reach through model. 93

5.5 Variation in free hole concentration with bias for the reach through model as the device undergoes reach-through. 94

5.6 Variation in free electron concentration with bias for the reach through model as the device undergoes reach-through. 94

5.7 Variation in potential and electric field across the reach through model at 50V and 300V. 95

5.8 Variation in free hole concentration with bias for the reverse reach through model. 96

5.9 Variation in free electron concentration with bias for the reverse reach through model. 96

5.10 Variation in free hole concentration with bias for the reverse reach through model as the device undergoes reach-through. 97

5.11 Variation in free electron concentration with bias for the reverse reach through model as the device undergoes reach-through. 97

5.12 Variation in potential and electric field across the reverse reach through model at 50V and 300V. 98

5.13 Comparison of the simulated bulk dark current from the reach through model with the measured total dark current from an EG&G C30916E reach through APD. 99

5.14 Comparison of the simulated bulk dark current from the reverse reach through model with the measured total dark current from an EG&G C30719F reverse reach through APD. 100

5.15 Comparison of the simulated photocurrent due to 650nm illumination calculated for the reach through model with the measured photocurrent from a C30916E APD. 101

5.16 Comparison of the simulated photocurrent due to 650nm illumination calculated for the reverse reach through model with the measured photocurrent from a C30719F APD. 102

5.17 Comparison of the gain measured from an EG&G C30916E reach through APD and the predicted gain from the reach through model, evaluated directly and indirectly. 103

5.18 Comparison of the gain measured from an EG&G C30719F reverse reach through APD and the predicted gain from the reverse reach through model, evaluated directly and indirectly. 104

5.19 Plot showing the simulated variation in k_{eff} with gain for a reach through model. 106

5.20 Plot showing the simulated variation in k_{eff} with gain for a reverse reach through model. 106

5.21 Comparison of the excess noise factor measured for a C30916E APD and the predicted excess noise factor from the reach through APD model. 107

5.22 Comparison of the excess noise factor measured for a C30719F APD and the predicted excess noise factor from the reverse reach through model. 107

5.23 Schematic showing the variation of the gain with position for a reach through and reverse reach through structure superimposed on the peak electric field region. 108

5.24 Comparison of the photosensitivity measured for a C30916E APD and the predicted photosensitivity from the reach through model at 300V. 110
5.25 Comparison of the photosensitivity measured for a C30719F APD and the predicted photosensitivity from the reverse reach through model at 300V. 110
5.26 Plot showing the variation in gain with incident wavelength measured for a C30916E APD and predicted by the reach through model. . . . 111
5.27 Plot showing the variation in gain with incident wavelength measured for a C30719F APD and predicted by the reverse reach through model. 112
5.28 Plot showing the free hole concentration through the reach through model at 50V for several neutron fluences. 113
5.29 Plot showing the free electron concentration through the reach through APD model at 50V for several neutron fluences. 114
5.30 Plot showing the free hole concentration through the reach through model at 300V for several neutron fluences. 114
5.31 Plot showing the free electron concentration through the reach through model at 300V for several neutron fluences. 115
5.32 Plot showing the change in potential through the reach through model for several neutron fluences 115
5.33 Plot showing the distribution of filled acceptors through the reach through model for several neutron fluences. 116
5.34 Plot showing the multiplication factor in the reach through model before and after neutron irradiation. 117
5.35 Plot showing the measured photocurrent in a C30916E APD and predicted by the reach through APD model before and after neutron irradiation. 117

5.36 Plot showing the measured photosensitivity in a C30916E APD and predicted by the reach through model before and after neutron irradiation. 119
5.37 Plot showing the free hole concentration through the reverse reach through model at 50V for several neutron fluences. 120
5.38 Plot showing the free electron concentration through the reverse reach through model at 50V for several neutron fluences. 120
5.39 Plot showing the free hole concentration through the reverse reach through model at 300V for several neutron fluences. 121
5.40 Plot showing the free electron concentration through the reverse reach through model at 300V for several neutron fluences. 121
5.41 Plot showing the change in potential across the reverse reach through model for several neutron fluences at 300V. 122
5.42 Plot showing the potential across the reverse reach through model at 300V before and after neutron irradiation. 123
5.43 Plot showing the distribution of filled acceptors through the reverse reach through model for several neutron fluences. 123
5.44 Plot showing the multiplication factor predicted by the reverse reach through model before and after neutron irradiation. 124
5.45 Plot showing the measured photocurrent in a C30719F APD and predicted by the reverse reach through model before and after neutron irradiation. 125
5.46 Plot showing the change in the measured gain for the C30719F APD and predicted by the reverse reach through model before and after neutron irradiation. 127
5.47 Plot showing the change in the photosensitivity measured for a C30719F APD and predicted by the reverse reach through model. 127

Chapter 1

Overview

1.1 Introduction

The use of light as an optical communication medium by humans pre-dates all the technical advances of the 20th century. A historic account of optical communication, dating from the fifth century BC, is given by Gower [1]. After discussing how Clytemnestra learns of the fall of Troy via beacons of fire, Gower rapidly ascends to the late 20th century to discuss the advent of the modern optical communication system. One of the major steps in the development was the discovery of avalanche muliplication in reversed biased PN junctions [2]. This led to the development of avalanche photodiodes.

1.1.1 Optical Photo-Detectors

The avalanche photodiode is just one of a vast array of optical photo-detectors, including the photomultiplier tube and the PIN photodiode. Before exploring these in more detail it would be prudent to discover the exact definition and purpose of an optical photo-detector.

The optical region of the electromagnetic spectrum comprises a small region between the infra-red and ultraviolet bands, that is visible to the human eye, figure 1.1. Optical photodetection refers to the detection of these electromagnetic waves. By detection we usually mean the conversion of such a wave into an electrical signal.

such that the signal amplitude is proportional to the intensity of the incident wave. A device capable of this task is known as a photo-detector.

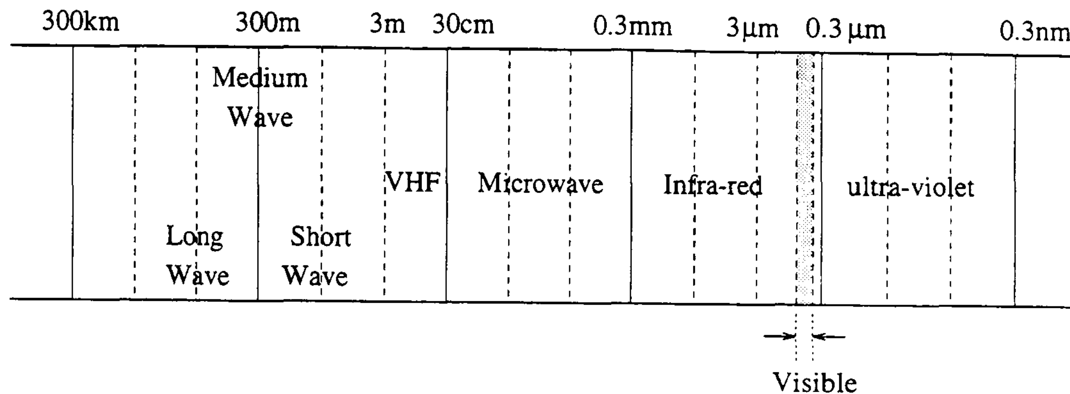

Figure 1.1: A figure showing the visible region of the electromagnetic spectrum.

The three photo-detectors briefly mentioned earlier will now be introduced in more detail. The physics behind the PIN photodiode and the avalanche photodiode will be discussed in detail in Chapter 2, where a more general introduction to semiconductor device physics is given.

1.1.2 The Photomultiplier Tube

The photomultiplier tube (PMT) differs from both the PIN photodiode and the avalanche photodiode (APD) in that it is a vacuum device. As such it will not be discussed again in detail, it is included here due to its popularity and wide range of applications.

A schematic of a typical PMT is shown in figure 1.2. There is enormous variation in the specific design of these devices, but the basic principles apply equally. The device consists of several key components; the photocathode, the dynodes and the collector. These are packaged in an evacuated container, typically glass with an optically transparent faceplate.

The key principle behind the operation of a PMT is the photoelectric effect. An incident photon will excite an electron in the photocathode. If the energy of the incident photon is greater than some threshold value, then the excited electron will be

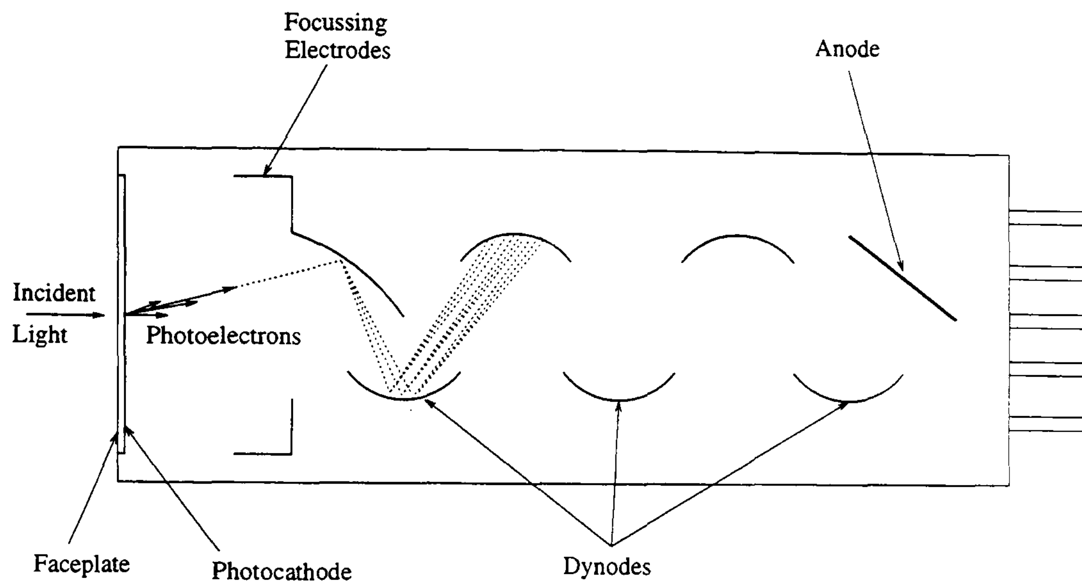

Figure 1.2: A schematic of a typical photomultiplier tube showing the key components of its operation and the path of the secondary electrons.

ejected into the vacuum. Typically the quantum efficiency of the PMT photocathode (~10-20% peak) will be well below that attainable by a photodiode, although improvements in the PMT quantum efficiency are still being actively researched [3].

The photoelectrons generated by the photocathode are now influenced by the internal electric field . This is due to the potential on the dynodes, which becomes progressively more positive along the device. The dynodes are designed to exhibit high secondary electron emission. This can be achieved by coating them with a material that has a negative electron affinity. The purpose of the dynodes is to produce a large number of secondary electrons for every electron incident on them. As the electrons traverse the device via the dynode chain, their number increases significantly until they are collected at the anode. If the secondary electron coefficient, i.e the number of secondary electrons per incident electron, is denoted as δ then for N dynodes the gain is given by equation (1.1).

$$\text{gain} = \delta^N \tag{1.1}$$

Thus if the secondary electron co-efficient,δ, is 5 and there are 12 dynodes then the gain would be approximately 2×10^8.

There exist two main noise processes that degrade the PMT signal. The first is shot noise associated with the quantum conversion of the incident light. This is amplified along with the signal. The second process is due to the statistical nature of the gain process. Secondary emission at the dynodes is a stochastic process, hence the gain can vary in a random way. This leads to an uncertainty in the initial signal, i.e. noise. This muliplication or excess noise can be denoted by a factor F. For the case where the secondary emission co-efficient is much greater than unity the *excess noise factor* is given by equation (1.2).

$$F = \frac{\delta}{\delta - 1} \tag{1.2}$$

If, as in the previous example, $\delta = 5$ then $F = 1.25$, and the excess noise will dominate.

The PMT is an extremely popular choice of photo-detector. This is due to their high gain, high speed and the availability of very large diameter devices. PMTs suffer from mechanical fragility, a high sensitivity to external magnetic fields and the requirement of stable high voltage supply for the dynode chain. Applications range from Positron Emission Tomography (PET) [4] to scintillation detection in High Energy Physics (HEP) [5], although their popularity is being eroded by the use of APDs [6], [7],[8].

1.2 PIN Photodiode

The PIN photodiode is one of the wide range of available semiconductor photo-detectors. The semiconductor photodiode detects light via the excitation of electrons from the valence band to the conduction band, figure 1.3 . In order to excite the electron into the conduction band the incident photon must have an energy greater than the band gap. The threshold wavelength at which light is detectable is therefore given by equation (1.3).

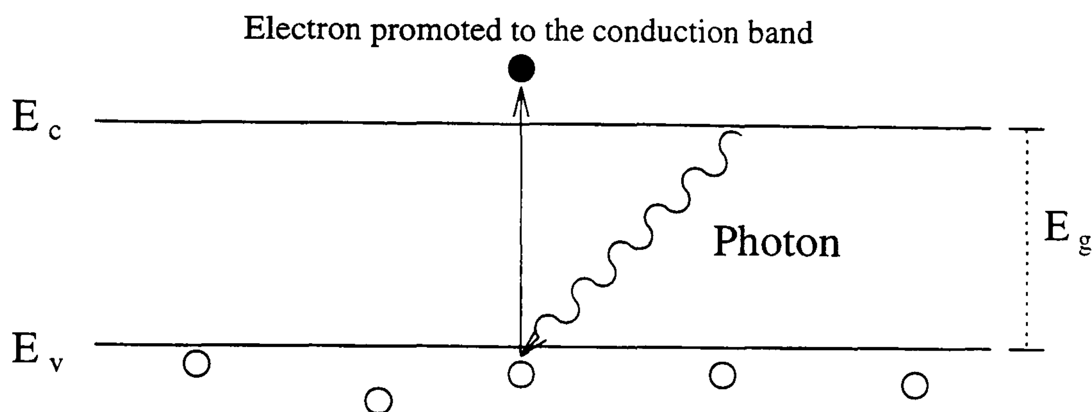

Figure 1.3: A simple diagram showing how the valence band electrons are excited into the conduction band by an incident photon.

$$\lambda_{\text{threshold}} = \frac{hc}{E_g} \tag{1.3}$$

A wide range of semiconductor photodetectors are available, table 1.1 lists a range of devices along with their gain and response time.

Photodetector	**Gain**	**Response Time** /s
Photoconductor	1	10^{-3}
pn Junction	1	10^{-11}
PIN photodiode	1	10^{-10}
Junction Transistor	10^2	10^{-8}
Avalanche Photodiode	10^4	10^{-10}
Metal-Semiconductor Diode	1	10^{-11}
Field-effect Transistor	10^2	10^{-7}

Table 1.1: Table showing typical values of gain and response time for a variety of semiconductor photo-detectors [9].

The PIN structure is commonly used in silicon photodiodes, a schematic of a typical Si PIN photodiode is shown in figure 1.4 . The device consists of several key regions; the anti-reflection coating, the heavily doped p+ layer, the heavily doped n+ layer and the lightly doped ν layer, which results in a wide depletion region. The anti-reflection coating is necessary to prevent Fresnel reflection at the

air-semiconductor interface. Typically the anti-reflection coating consists of a thin film of either SiO_2 or Si_3N_4. The lightly doped ν region becomes fully depleted at operating bias, presenting a large detection volume to an incident signal. This increases the quantum efficiency at longer wavelengths, where the absorption length in silicon can reach $10\mu m$. It also significantly reduces the device capacitance due to the wide depletion region.

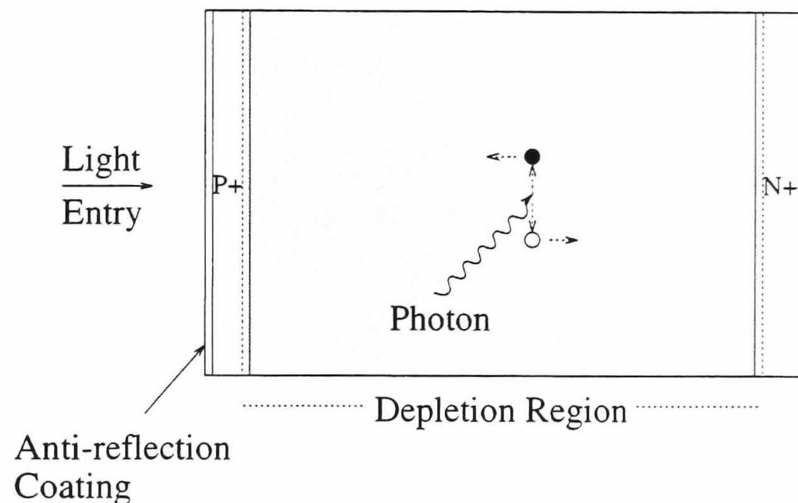

Figure 1.4: A simple schematic of a typical silcon PIN photodiode, showing the incident photon being collected in the depletion region.

The PIN photodiode has found use in a wide variety of applications ranging from data buses [10] to pressure sensing applications in the automotive industry [11]. The PIN photodiode has such versatility due to its ruggedness, compact size, good temperature and bias stability, low operating bias and good linearity. The main disadvantage of the PIN structure is the lack of an internal gain mechanism, which almost always makes the use of an external amplifier mandatory. They are also efficient detectors of electrons and x-rays, which can seriously degrade an optical signal if present.

1.3 Avalanche Photodiode

The avalanche photodiode is a semiconductor photo-detector that encompasses most of the advantages of the PIN structure but has the additional benefit of an internal

gain mechanism. A schematic of a typical silicon reach through APD structure is shown in figure 1.5. The APD shares many features with the PIN photodiode. The key regions of the APD are the anti-reflection coating, the highly doped n+ region, the p region, the lightly doped π region and finally the p+ region. The lightly doped π region gives rise to a wide depletion region that increases the quantum efficiency for longer wavelengths. The electric field in the device is at its maximum at the junction between the highly doped n+ and p layers. This is where the gain of the device is generated.

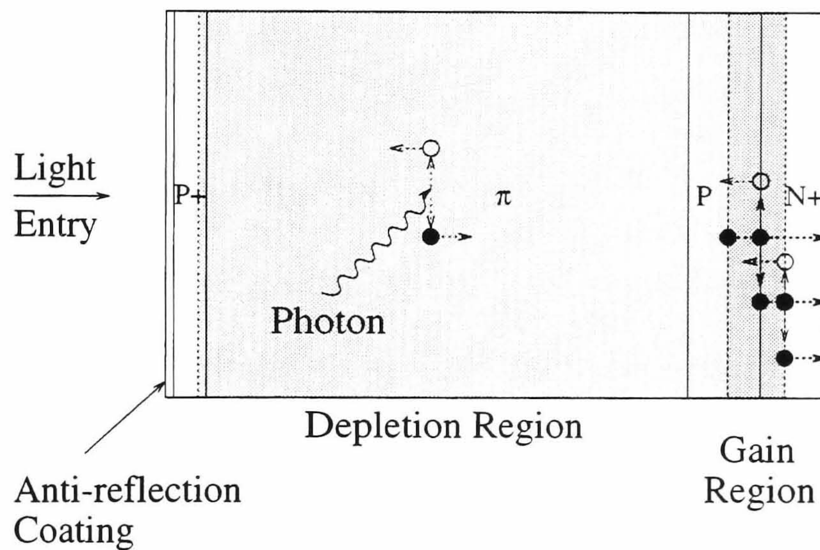

Figure 1.5: A simple schematic of a typical silicon reach through avalanche photodiode, showing the incident photon being collected in the depletion region and the process of impact ionisation in the gain region.

The APD uses the process of impact ionisation to generate gain. This will be discussed further in chapter 2. Impact ionisation occurs when a charge carrier gains enough energy from the electric field, between collisions, to ionise further charge carriers. In silicon this process becomes significant when the electric field reaches approximately 10^5Vcm^{-1}. Once a new charge carrier is liberated this can go on to impact ionise other charge carriers. The process continues and rapidly the signal is amplified.

Avalanche photodiodes thus have an advantage over PIN photodiodes, their internal gain mechanism increasing their input sensitivity and improving the signal to

noise ratio. APDs are also rugged and have good linearity. There are disadvantages that the gain mechanism introduces, high operating voltages of around 200 to 500V are typical. The devices can also be very sensitive to small changes in temperature or bias, this is usually due to the sensitivity of the gain. The statistical nature also introduces another source of noise, similar to the PMT, quantified in terms of the *excess noise factor*, F.

The uses of APDs are as diverse as those of PIN photodiodes. APDs are rapidly overtaking the use of PMTs in many areas including PET scanning [12]. A particularly interesting area where APDs are finding many uses is in the area of experimental High Energy Physics (HEP) [13],[14].

1.3.1 High Energy Physics

One particularly interesting example where the use of APDs has been adopted is for the electromagnetic calorimeter (ECAL) in the Compact Muon Solenoid (CMS) experiment. The CMS ECAL will operate in a uniform 4T magnetic field and will be subject to the most extreme radiation conditions. The photo-detectors will be exposed to a large neutron fluence in the ten year operation, estimated to be 2×10^{13} n/cm^2 in the barrel and 7×10^{14} n/cm^2 in the endcap [15]. The magnetic field instantly rules out the use of most vacuum devices, e.g. the PMT, thus the next choice was to use a semiconductor photo-detector. The low light yield of the scintillating crystals used in the CMS ECAL required that the photo-detectors possess an internal gain mechanism, thus APDs were selected.

1.4 The Compact Muon Solenoid Electromagnetic Calorimeter

1.4.1 Overview of CMS

The Compact Muon Solenoid [16],[17] is a general purpose detector proposed for use at the Large Hadron Collider (LHC) at CERN. The LHC is a 7+7 TeV proton-

proton collider that will replace the Large Electron Positron (LEP) collider presently running at CERN. The CMS detector has been optimised for the search for the standard model Higgs Boson, but will also be used to explore all the new physics that will occur at the LHC energies.

The CMS detector is shown in figure 1.6. The detector has a total length of 21.6m, a radius of 7.5m and a total weight of 12500 tonnes. The detector consists of a complement of intricate subsystems, from the core outward they are; the inner tracker, the electromagnetic calorimeter, the hadron calorimeter and a 4T superconducting solenoid coupled with a multi-layered muon system.

1.4.2 The ECAL

The main channels that will be used by the CMS experiment to detect the presence of the Higgs are the decays of the Higgs into two photons for $m_H \leq 150$ GeV and into four leptons for 140 GeV $\leq m_H \leq$ 700 GeV. The ECAL will provide much of the important information from these processes. A scintillating crystal calorimeter was chosen as this offered the best energy resolution [18], enhancing the likelihood of discovering the Higgs Boson.

	NaI(Tl)	**BGO**	**CsI**	**BaF_2**	**CeF_3**	**$PbWO_4$**
Density $/gcm^{-3}$	3.67	7.13	4.51	4.88	6.16	8.28
Radiation Length /cm	2.59	1.12	1.85	2.06	1.68	0.89
Interaction Length /cm	41.4	21.8	37.0	29.9	26.2	22.4
Molière radius /cm	4.80	2.33	3.50	3.39	2.63	2.19
Light Decay Time /ns	230	60 300	16	0.9 630	8 25	5 (39%) 15(60%) 100(1%)
Refractive Index (480nm)	1.85	2.15	1.80	1.49	1.62	2.30
Peak Emission /nm	410	480	315	210 310	300 340	440
Temperature Coeff. %/°C	0	-1.6	-0.6	-2/0	0.14	- 2
Relative Light Output	100	18	20	20/4	8	1.3

Table 1.2: Table showing the properties of various scintillating media [15].

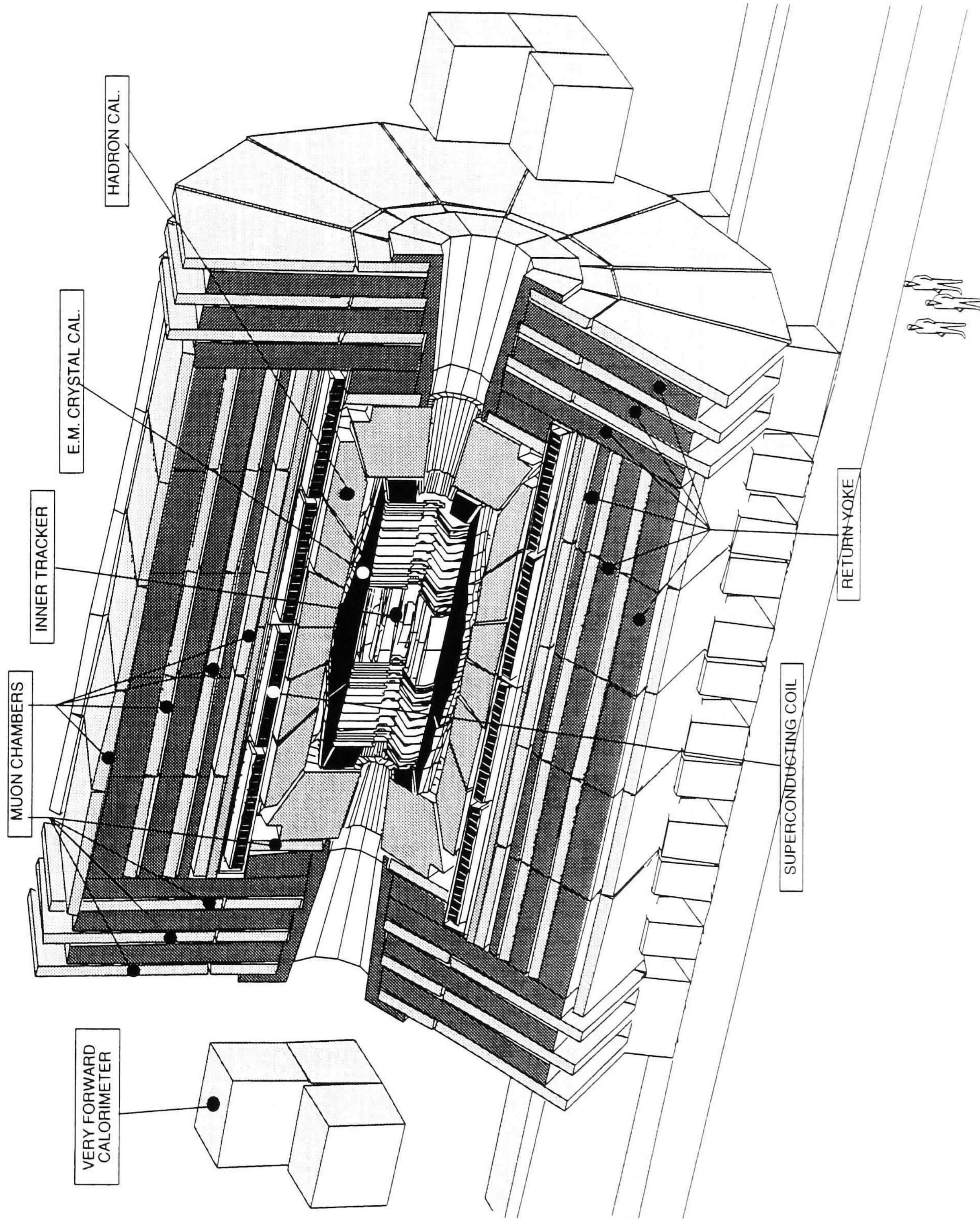

Figure 1.6: A figure showing the CMS detector due to start running at the Large Hadron Collider at CERN in 2005.

Lead tungstate, $PbWO_4$, crystals were chosen as the scintillating medium for the CMS calorimeter. A comparison of the properties of lead tungstate with other common scintillation media is show in table 1.2. Lead tungstate offers benefits such as; high density, a fast scintillator and a wide availability of raw materials. The high density of the crystals results in a short radiation length and small Molière radius, allowing the calorimeter to have a much reduced radius. The radiation tolerance of the crystals is adequate to withstand the radiation levels.

1.4.3 Application of APDs

The significant problem with the lead tungstate crystals is that of a very low light yield. Thus the use of a photo-detector with internal gain becomes essential to maintain the required resolution. APDs were selected because they fulfilled the criteria laid out for an ECAL photo-detector [17], [19] :

- ability to operate at any angle in a 4T magnetic field
- high quantum efficiency in the range of $PbWO_4$ emission
- stable gain
- radiation tolerant to an integrated fluence of 4×10^{14}ncm^{-2}
- small leakage current and low input capacitance
- low response to charged particles.

The last of the specifications ruled out the use of PIN photodiodes. The lack of an internal gain mechanism combined with the low $PbWO_4$ light yield resulted in the signal from the crystals being swamped by interactions of particles with the PIN photodiodes.

An extensive research and development program, focussing on the experimental evaluation of candidate devices was undertaken. Two devices, the EG&G C30626E reverse reach through APD and the Hamamatsu HS282 APD were developed over two years. The key parameters of both devices are detailed in table 1.3.

It was discovered that the devices would not be able to withstand the extremely harsh neutron radiation environment in the calorimeter endcap. Vacuum phototri-

Parameter	Goal	Hamamatsu	EG&G
Active Area /mm^2	> 50	25	25
Quantum Efficiency @ 450nm /%	80	80	75
Capacitance /pF	< 100	100	25
Series Resistance /Ω	< 10	5	5
Excess Noise Factor	< 2	2.0	2.3
Operating Bias Voltage /V	< 500	400-420	350-450
Initial Dark Current /nA	< 100	2-3	30-70
$dM/dV \times 1/M$ @ $M = 50$ /%	< 2	5	0.6
$\lvert dM/dT \rvert \times 1/M$ @ $M = 50$ /%	<-2	-2.3	-2.7
Passivation Layer	Si_3N_4	Si_3N_4	Si_3N_4
Packaging	non-magnetic	non-magnetic	non-magnetic

Table 1.3: Table showing the desired and measured parameters of the candidate APDs for the CMS ECAL [15]

odes, a small vacuum photodetector that can still operate when quasi-axial to a high magnetic field, have been selected as replacement photo-detectors in the endcap region.

1.4.4 Introducing the Simulation

To aid the experimental research and development program a simulation of the candidate EG&G device was developed. A severe limitation was imposed on the simulation by the lack of detailed knowledge about the device structure. The manufacturers were keen to limit the spread of information regarding their devices, which were commercial derivatives. The simulation work was concentrated on the EG&G C30626E reverse reach through device, due to the slightly increased availability of literature regarding the structure [20],[21],[22].

The aim of the simulation is to emulate, as accurately as possible within the limitations, the performance of the device in as wide a range of conditions i.e. bias, illumination and neutron irradiation, as possible. Also the simulation is to be dynamic enough to allow models of other structures to be easily constructed. maximising the benefit of the simulation.

A drift-diffusion formulation, that uses the classical semiconductor equations to describe the flow of charge through the device, was chosen. This allowed the majority of standard tests performed on the APDs to be directly modelled. This type of model was used, very successfully, to model the behaviour of silicon microstrip detectors under neutron irradiation [23], [24]. Thus a proven scheme of introducing radiation damage to the devices could be confidently implemented.

In conjunction with the EG&G reverse reach through APD, a commercial EG&G reach through type structure was modelled. Schematics of the electric field profile through both a reach through and reverse reach through APD device are shown in figure 1.7. The model of the commercial diode was included to demonstrate the wide variety of applications available to the model.

1.5 Overview of Thesis

The work presented in this thesis describes in detail the technical implementation of the simulation coupled with the limitations involved and possible avenues for further development. Models of a reverse reach through device, based on the EG&G C30626E proposed for use in the CMS ECAL, and a reach through device that assumes the general structure of some commercial silicon APDs are presented. Variation in the applied bias and the incident wavelength are investigated. The effects of neutron irradiation on the operation of the devices is studied. A short experimental study is also introduced that aims to qualitatively confirm the predictions made by the models.

Chapter 2 will introduce some of the topics that are implemented in the model. These include impact ionisation, Shockley-Read-Hall recombination and the mechanisms involved in neutron radiation damage. Chapter 3 will introduce the techniques employed in the short experimental evaluation of the devices. An exhaustive technical summary of the simulation packages is presented in Chapter 4. The limitations of the model are discussed and avenues for development uncovered. Chapter 5 will

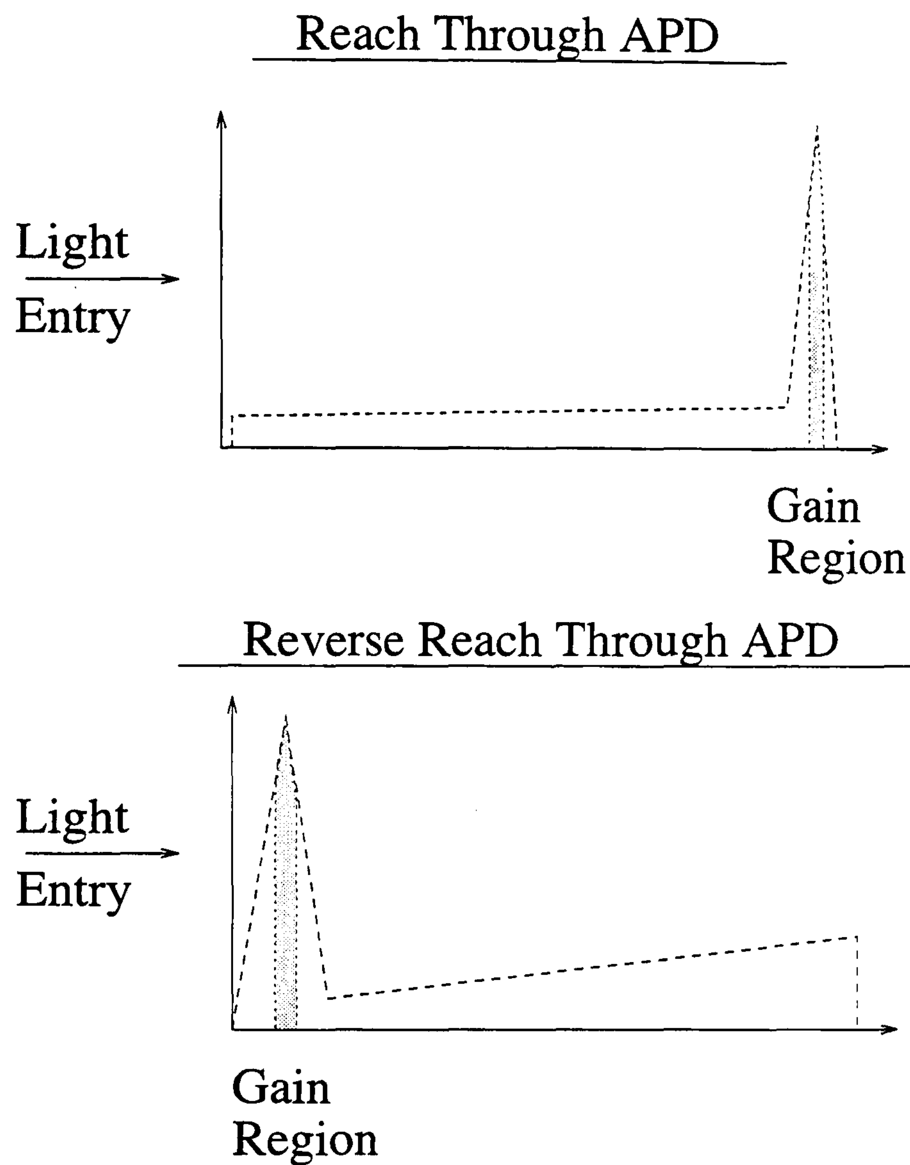

Figure 1.7: A simple schematic showing the electric field profiles and gain regions of the EG&G reach through and reverse reach through APDs.

compare data from the model with the results from the experimental study. Conclusions will be drawn in chapter 6.

Chapter 2

APD Device Theory and Operation

2.1 Introduction

Simulating the operation of semiconductor photo-detectors requires an understanding of the microscopic processes that occur. These fundamental processes are well described and form the basis of modern semiconductor theory. A typical semiconductor photo-detector incorporates a reversed biased pn-junction to form a depletion region, in which the incident photons are collected. Pairs of charge carriers, generated via photoexcitation, rapidly drift apart in the depleted region and are collected to form the electronic signal. In the case of the avalanche photodiode an additional process, impact ionisation, is utilised to multiply the number of charge carriers, hence amplify the measured signal. This chapter will introduce the theories relevant to semiconductor photo-detectors, and in particular the silicon avalanche photodiode. It will also introduce the terms in the semiconductor equations necessary to simulate the operation of a silicon avalanche photodiode.

2.2 The Semiconductor Equations

2.2.1 Introduction

The simulation presented in this thesis is based on a drift-diffusion formulation [25]. The flow of charge through and the potential variation across the device are described by a well-known set of partial differential equations, frequently referred to as the semiconductor equations, (2.1) to (2.5) [26].

$$\frac{\delta p}{\delta t} = -\frac{1}{q}\mathrm{div}\vec{J_p} + \mathrm{G} - \mathrm{U} \tag{2.1}$$

$$\frac{\delta n}{\delta t} = \frac{1}{q}\mathrm{div}\vec{J_n} + \mathrm{G} - \mathrm{U} \tag{2.2}$$

$$\vec{J_p} = -qD_p \,\mathrm{grad}\, p - q\mu_p p \,\mathrm{grad}\, \psi \tag{2.3}$$

$$\vec{J_n} = qD_n \,\mathrm{grad}\, n - q\mu_n n \,\mathrm{grad}\, \psi \tag{2.4}$$

$$\mathrm{div\ grad}\ \psi = -\frac{q}{\epsilon}\left(N_d - N_a + p - n\right) \tag{2.5}$$

Where n and p are the free electron and hole concentrations, $\vec{J_n}$ and $\vec{J_p}$ the electron and hole current densities, μ_n and μ_p the electron and hole mobilities, D_n and D_p the electron and hole diffusivity co-efficients, ψ the potential, N_d and N_a the ionised donor and acceptor concentrations, U the recombination rate, G the generation rate and q the electronic charge.

These fundamental equations form the theoretical basis of the simulation, and will be investigated further. The set of equations can be categorised into:

The current equations (2.3),(2.4) - describe the flow of electrons and holes through the semiconductor by both drift and diffusion.

The continuity equations (2.1),(2.2) - account for the change in the carrier concentration according to the current flow and generation-recombination processes.

The Poisson equation (2.5) - describes the potential variation across the semiconductor due to the influence of free carriers and ionised dopants.

2.2.2 The Current Equations

The flow of charge in a semiconductor can be written as the superposition of both the drift and diffusion currents. The drift current is due to the response of the charge carriers to an electric field, and the diffusion current the result of density gradients in the charge carrier population. The one-dimensional forms, applicable to the model, will be introduced.

The Drift Term

The drift current density can be written in terms of the conductivity, σ, of the material and the electric field, in one-dimensional form:

$$J(x) = \sigma E(x). \tag{2.6}$$

The current can also be written in terms of the density of charge carriers, N, the charge per carrier, q, and the drift velocity, v_d:

$$J(x) = qNv_d(x). \tag{2.7}$$

By equating equations (2.6) and (2.7) we can define the mobility, μ, which describes the response of a charge carrier to an applied electric field, equation (2.8).

$$\mu = \frac{\sigma}{qN} \quad \text{hence} \quad v_d(x) = \mu E(x) \tag{2.8}$$

Hence the drift current density can be written in terms of the mobility, equation (2.9).

$$J(x) = q\mu N E(x) \tag{2.9}$$

The Diffusion Term

When a concentration gradient exists in the distribution of randomly moving particles, they will tend to arrange themselves until their concentration is uniform. In the case of charge carriers in a semiconductor, for example the electrons, the redistributive current density is given by equation (2.10). This form applies equally to the holes.

$$J_e(x) = -qD_n \frac{\mathrm{d}n}{\mathrm{d}x} \tag{2.10}$$

The Einstein relation equates the diffusivity co-efficient, D_n with the mobility, introduced in section 2.2.2, for the low injection case:

$$D_n = \frac{kT}{q}\mu_n. \tag{2.11}$$

Where k is the Boltzmann constant and T the absolute temperature. Hence the diffusion current density can be re-written in terms of the mobility of the charge carrier, equation (2.12).

$$J_e(x) = kT\mu_n \frac{\mathrm{d}n}{\mathrm{d}x} \tag{2.12}$$

The total current density can now be expressed as the sum of the drift and diffusion terms. Equation (2.13) shows the form of the total electron current density.

$$J_e(x) = q\mu_n \left(nE(x) + \frac{kT}{q}\frac{\mathrm{d}n}{\mathrm{d}x} \right) \tag{2.13}$$

2.2.3 The Continuity Equations

The charge carrier density in a semiconductor is not only affected by the current flow, but is also subject to a range of generation and recombination processes. The continuity equations describe how the charge carrier density varies with time as a result of the complex interaction between these effects. The one-dimensional form of the continuity equations is given, for electrons, by equation (2.14).

$$\frac{\delta n}{\delta t} = G - U + \frac{1}{q}\frac{\mathrm{d}J_x}{\mathrm{d}x} \tag{2.14}$$

The terms for generation, G, and recombination, U, will be discussed in detail in section 2.3.2.

2.2.4 The Poisson Equation

Modern semiconductor photodiodes are often operated in reverse bias, ensuring a large detecting volume is exposed to the incident illumination. The performance of a semiconductor diode in reverse bias is strongly affected by the presence of ionised dopant atoms in the depletion region. The Poisson equation written in its simplest form is given in equation (2.15).

$$\frac{\mathrm{d}^2\psi}{\mathrm{d}x^2} = -\frac{\rho}{\epsilon_0} \tag{2.15}$$

In a semiconductor the charge density, ρ, is comprised of the mobile charge carriers and the ionised dopants. Thus equation (2.15) can be expressed explicitly, equation (2.16).

$$\frac{\mathrm{d}^2\psi}{\mathrm{d}x^2} = -\frac{q}{\epsilon_0}\left(N_d - N_a + p - n\right) \tag{2.16}$$

The set of equations can be used to form an accurate mathematical description of the operation of a semiconductor device. Unfortunately their complexity forms a significant hurdle in their application. Finding an analytical solution to the equations is extremely difficult, except in the most simple of cases. Fortunately a wide range of numerical methods exist that enable the equations to be used in a practical way. In particular the method of finite differences can be used to express the equations in a more manageable form. This process is discussed in detail in chapter 4.

2.3 The PN Junction

2.3.1 Introduction

A pn-junction is formed at the boundary of a p-type region and n-type region in a semiconductor crystal. Typically the distribution of dopants in the semiconductor will not be trivial. This is in part caused by the techniques used to introduce the dopants into the semiconductor crystal, and also due to the complexity of useful designs. In most cases however, the actual doping profile can be represented by a simplified version, to provide a theoretical basis.

The pn-junction formed the original practical application of semiconductor device technology. Shockley [27], was the first to provide a mathematical description of the current-voltage characteristics of the pn-junction diode. The diversity of modern semiconductor devices is only overshadowed by the complexity of the modern theories that describe them. But the pn-junction still forms a fundamental building block in many semiconductor devices, and the theories devised by Shockley still reside in most modern semiconductor texts.

The work presented in this thesis does not provide an analytical solution to the problems being investigated, as Shockley did when he formulated the diode

law. Instead a numerical method is employed to solve the semiconductor equations, for a given set of conditions. The algorithmic process is essentially replacing the formulaic solution, which would be almost impossible to derive. Before the numerical methods can be applied to the semiconductor equations, they must be expressed explicitly. Hence the terms representing generation and recombination processes must be investigated in more detail.

2.3.2 Thermal Generation and Recombination Processes

At any time in a semiconductor, there are generation and recombination processes occurring. A dynamic equilibrium is formed when the conflicting processes exactly cancel. In silicon the recombination occurs via an intermediate state, and is known as indirect recombination, figure 2.1. The position of the intermediate level affects the recombination efficiency.

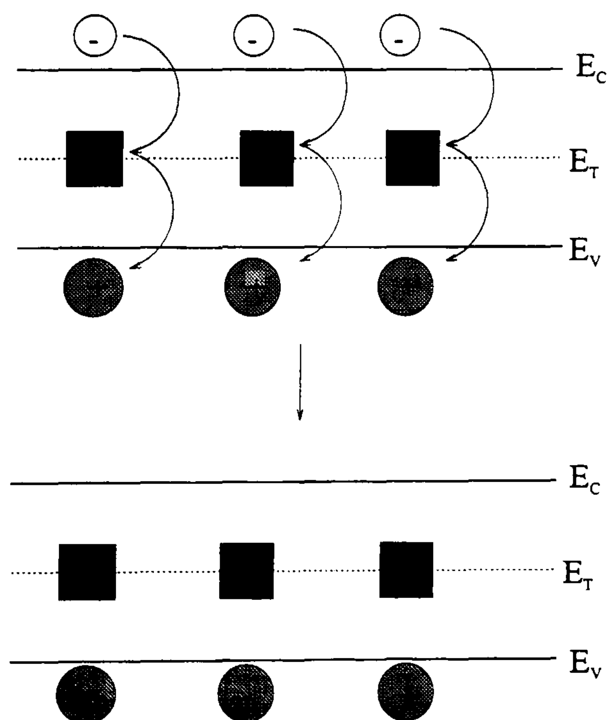

Figure 2.1: A simple diagram showing indirect recombination.

Materials, such as intrinsic gallium arsenide, do not exhibit this behaviour. Instead the recombination occurs spontaneously between the valence and conduction band, and is known as direct recombination, figure 2.2 . Near the band edges the

intermediate states are denoted as traps; these are typically formed from impurities in the semiconductor and by-products of the production process. Recombination centres, which promote the most efficient recombination, are found near the centre of the bandgap.

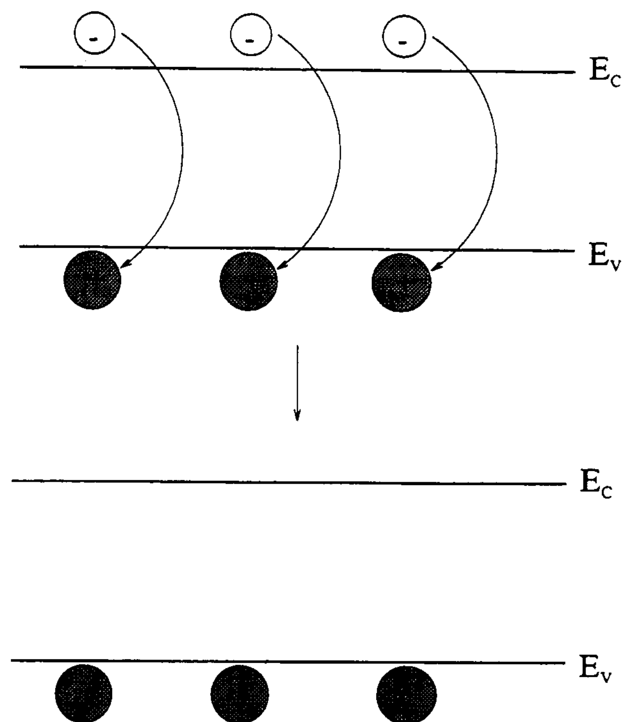

Figure 2.2: A simple diagram showing direct recombination.

The APDs evaluated in this thesis are produced from silicon, thus the process of indirect recombination will be investigated further.

2.3.3 Indirect Recombination

There are several processes that can occur during indirect recombination. Figure 2.3 follows from 2.1, to show the individual processes; electron capture, electron emission, hole capture and hole emission respectively. The processes have a corresponding recombination rate, shown by equations (2.17), (2.18), (2.19) and (2.20), where C_e and C_h are the electron and hole capture rates, e_n and e_p the electron and hole emission rates, N_T the trap density and $f(E_T)$ the Fermi function at the trap energy level.

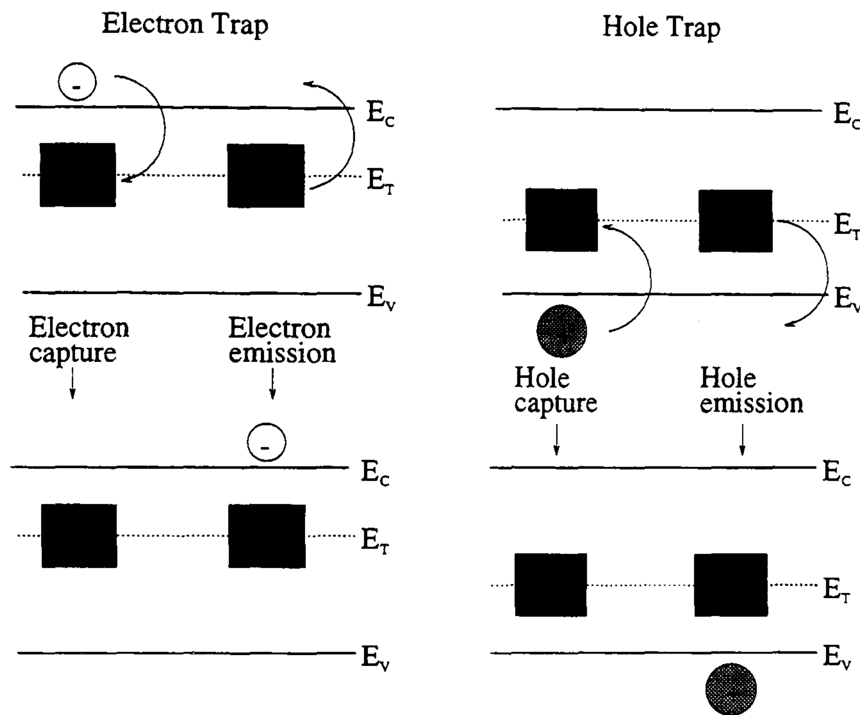

Figure 2.3: A diagram showing the processes involved in indirect recombination.

$$\text{electron capture} : r_a = C_n n N_T (1 - f(E_T)) \tag{2.17}$$

$$\text{electron emission} : r_b = e_n N_T f(E_T) \tag{2.18}$$

$$\text{hole capture} : r_c = C_p p N_T f(E_T) \tag{2.19}$$

$$\text{hole emission} : r_d = e_p N_T (1 - f(E_T)) \tag{2.20}$$

If we consider the non-equilibrium case where carriers are generated at a rate G, but at steady state, we can write the continuity equations for n-type silicon, equations (2.21) and (2.22).

$$\frac{\delta n}{\delta t} = G_e - (r_a - r_b) \tag{2.21}$$

$$\frac{\delta p}{\delta t} = G_h - (r_c - r_d) \tag{2.22}$$

At steady state the charge carrier concentrations remain constant with time, hence the derivatives are zero, and the recombination and generation terms for each carrier type are equal. Thus we can write equation (2.23).

$$r_a - r_b = r_c - r_d \tag{2.23}$$

The emission rates for electrons and holes are expressed by equations (2.24) and (2.25) respectively.

$$e_n = \sigma_n v_{th} N_c \exp^{-\frac{E_c - E_T}{kT}} \tag{2.24}$$

$$e_p = \sigma_p v_{th} N_v \exp^{-\frac{E_T - E_v}{kT}} \tag{2.25}$$

Where N_c and N_v are the effective density of states in the conduction band and valence band. The capture rates can also be expressed in terms of the capture cross section, $\sigma_{n/p}$, and the thermal velocity for the electrons and holes, equations (2.26) and (2.27) respectively.

$$C_n = \sigma_n v_{th} \tag{2.26}$$

$$C_p = \sigma_p v_{th} \tag{2.27}$$

Equations (2.17) to (2.20) and equations (2.24) to (2.27) can be substituted into equation (2.23) to give equation (2.28).

$$\sigma_n n N_T(1 - f(E_T)) - N_T \sigma_n N_c \exp^{-\frac{E_c - E_T}{KT}} f(E_T) =$$
$$\sigma_p p N_T f(E_T) - N_T \sigma_p N_v \exp^{-\frac{E_T - E_v}{KT}} (1 - f(E_T)) \quad (2.28)$$

Equation (2.28) can be re-arranged to give the trap occupancy function, equation (2.29).

$$f(E_T) = \frac{n + \frac{\sigma_p}{\sigma_n} N_v \exp^{-\frac{E_T - E_v}{KT}}}{n + N_c \exp^{-\frac{E_c - E_T}{KT}} + p\frac{\sigma_p}{\sigma_n} + \frac{\sigma_p}{\sigma_n} N_v \exp^{-\frac{E_T - E_v}{KT}}} \quad (2.29)$$

The form of the occupancy function can now be re-inserted into equation 2.28 to give the recombination rate, equation 2.30 [28],[29].

$$R = \frac{\sigma_p \sigma_n v_{th} N_T \left[pn - n_i^2\right]}{\sigma_n \left[n + N_c \exp^{-\frac{E_c - E_T}{KT}}\right] + \sigma_p \left[p + N_v \exp^{-\frac{E_T - E_v}{KT}}\right]} \quad (2.30)$$

The minority carrier lifetimes for electrons and holes can be expressed in terms of the capture cross section, the carrier thermal velocity and the trap density, equations (2.31) and (2.32) respectively.

$$\tau_n = \frac{1}{\sigma_n v_{th} N_T} \quad (2.31)$$

$$\tau_p = \frac{1}{\sigma_p v_{th} N_T} \quad (2.32)$$

Expressing the recombination rate, equation (2.30), in terms of the intrinsic Fermi level via equations (2.33) and (2.34) and re-arranging, results in a form suitable for solution using numerical methods, equation (2.35).

$$N_c \exp^{-\frac{E_c-E_T}{KT}} = n_i \exp^{\frac{E_i-E_T}{KT}} \tag{2.33}$$

$$N_v \exp^{-\frac{E_T-E_v}{KT}} = n_i \exp^{-\frac{E_T-E_i}{KT}} \tag{2.34}$$

$$R = \frac{pn - n_i^2}{\tau_p \left[n + n_i \exp^{\frac{E_i-E_T}{KT}}\right] + \tau_n \left[p + n_i \exp^{-\frac{E_T-E_i}{KT}}\right]} \tag{2.35}$$

2.3.4 Additional Generation and Recombination Processes

So far a term for the trap-assisted recombination has been derived. This describes the processes that occur in a non-equilibrium pn-junction at steady state. There is another important process that needs to be introduced into the semiconductor equations in order to describe fully the operation of a silicon avalanche photodiode.

2.3.5 Impact Ionisation

The avalanche photodiode was briefly introduced in chapter 1. The devices are able to amplify the incident signal via the process of impact ionisation, shown in the band diagram in figure 2.4. In a region of sufficiently high electric field, typically above 10^5V/cm for silicon, electrons travelling on average $\frac{1}{\alpha_e}$ and holes travelling on average $\frac{1}{\alpha_h}$ will gain enough energy to impact ionise further electron-hole pairs. Any charge carrier entering the high field region will undergo this process. Hence the bulk dark current will be amplified along with any useful photo-generated signal. Impact ionisation can be included in the mathematical description of the avalanche photodiode via a generation term in the continuity equations, equation (2.36).

$$G(x) = \frac{1}{q}\left(\alpha_e J_n(x) + \alpha_h J_p(x)\right) \tag{2.36}$$

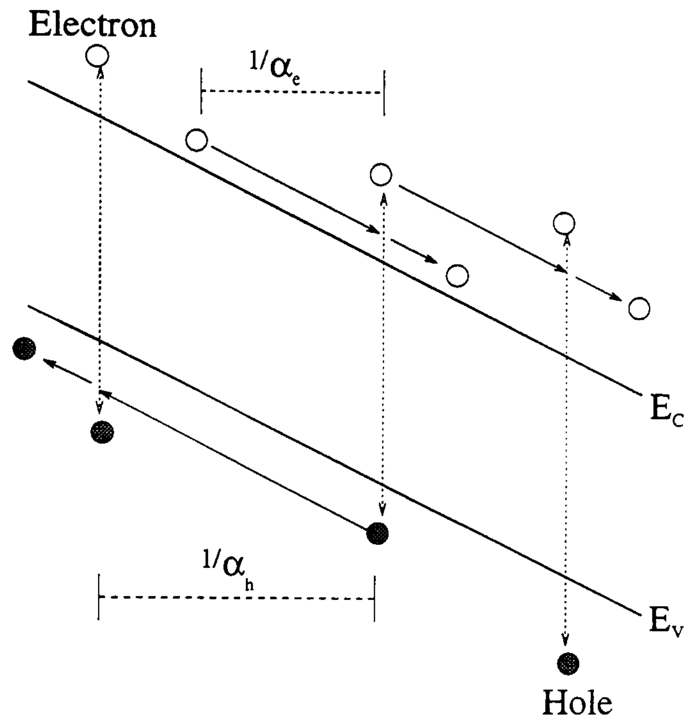

Figure 2.4: A band diagram showing the process of impact ionisation.

Figure 2.5 shows the values of α_e and α_h as a function of the electric field calculated from the Chenowyth parameterisation, [30], for silicon at room temperature. The parameterisation, equation (2.37), provides a good approximation of the ionisation coefficients at room temperature.

$$\alpha = A\text{exp}^{-B/E} \tag{2.37}$$

Parameters A and B are detailed in table 2.1.

	Electron	Hole
A (cm^{-1})	3.8×10^6	2.25×10^7
B (V/cm)	1.75×10^6	3.26×10^6

Table 2.1: Table showing the parameters used in the Chenowyth expression for the ionisation co-efficients in silicon [30].

The ratio of the ionisation coefficients, k($=\alpha_h/\alpha_e$), is an important parameter in the analysis of avalanche photodiodes, and typically lies in the range 0.1 to 100.

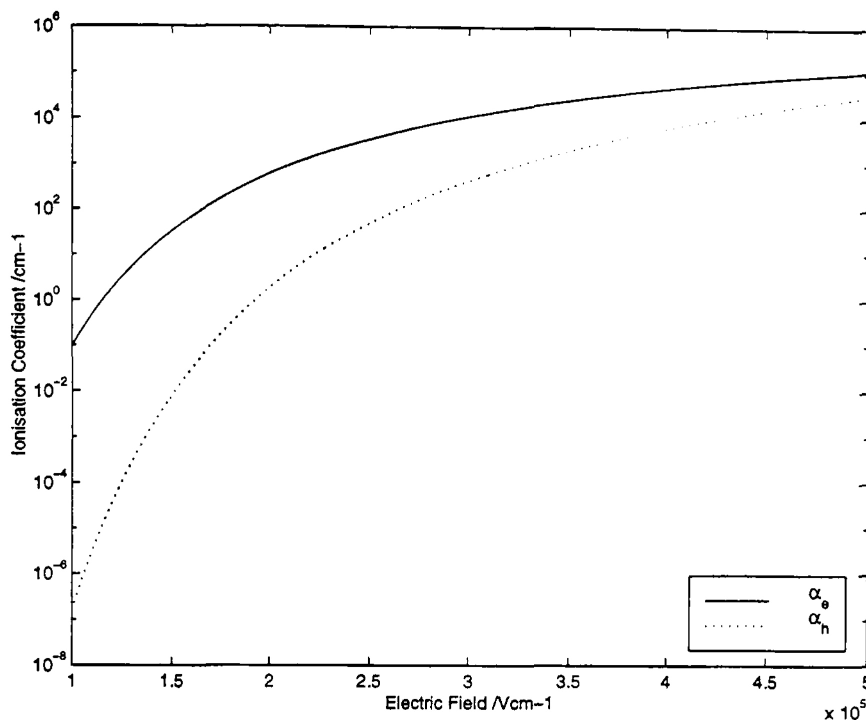

Figure 2.5: Figure showing the values of α_e and α_h, at room temperature, calculated using the Chenowyth parameterisation.

The value of k significantly affects the quality of APD performance, and constrains the way the device is used, if efficient operation is to be maintained.

Figures 2.6 and 2.7 show the formation of avalanches, with k=0 and k$\neq$ 1 respectively. In each example an electron, injected at the edge of the gain region, initiates the avalanche. In figure 2.6, where k=0, the avalanche evolves in a simple manner resulting in an exponential increase in the number of electrons. In figure 2.7, the avalanche includes a process of 'positive feedback', from the significant hole multiplication, resulting in a much more complex gain process [1].

If we consider the case where k=0 ($\alpha_h = 0$), and an electron current,J_{n0}, is injected at the edge of the gain region, the change in the electron current, $J_n(x)$, with position can be written as equation (2.38).

$$-\frac{\mathrm{d}J_n(x)}{\mathrm{d}x} = \alpha_e J_n(x) \tag{2.38}$$

The solution for $J_n(x)$ is shown in equation (2.39). If the electron current is evaluated

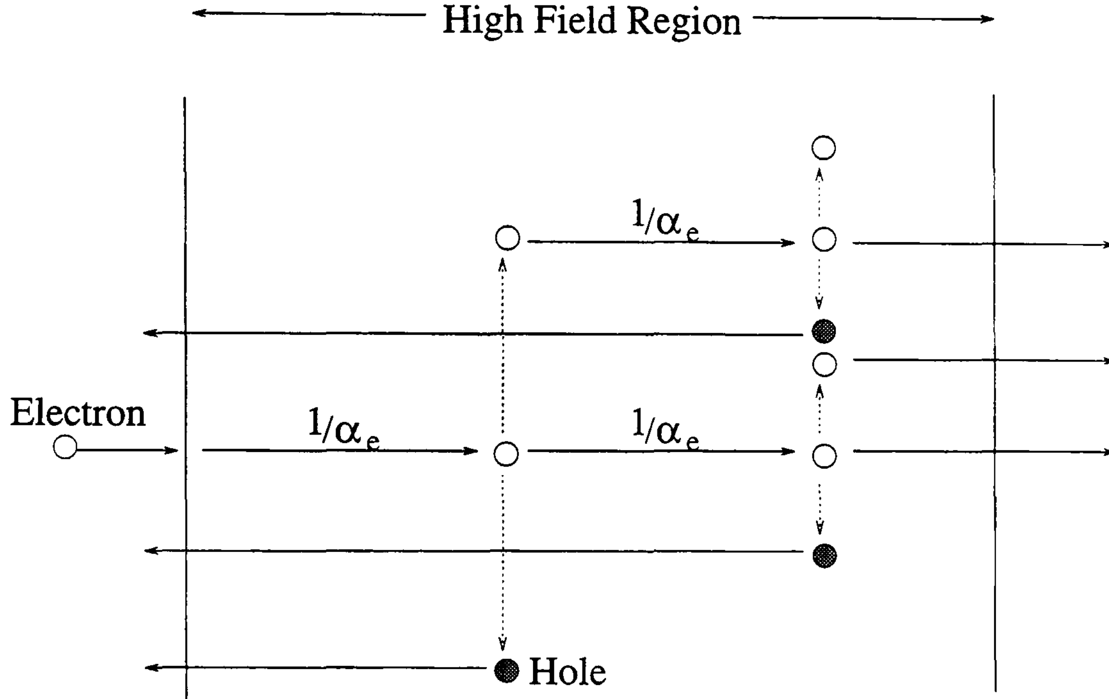

Figure 2.6: A diagram showing the formation of an avalanche where k=0.

after traversing the gain region, width w, the gain can be evaluated, equation (2.40).

$$J_n(x) = J_{n0}\exp^{\int_0^x \alpha_e \mathrm{d}x} \tag{2.39}$$

$$M_e = \frac{J_n(w)}{J_{n0}} = \exp^{\int_0^w \alpha_e \mathrm{d}x} \tag{2.40}$$

The exponential growth in the electron current is clearly shown. For the case where k≠0, the electron multiplication can be shown to be given by equation 2.41 [1].

$$M_e = \frac{1}{1 - \int_0^w \alpha_e \exp^{-\int_0^w \alpha_e - \alpha_h \mathrm{d}x'} \mathrm{d}x} \tag{2.41}$$

For the case where only one of the carrier types undergoes impact ionisation the gain can become large, but will never become infinite. Hence the device will never break down. In reality, for most practical materials, both carriers will readily

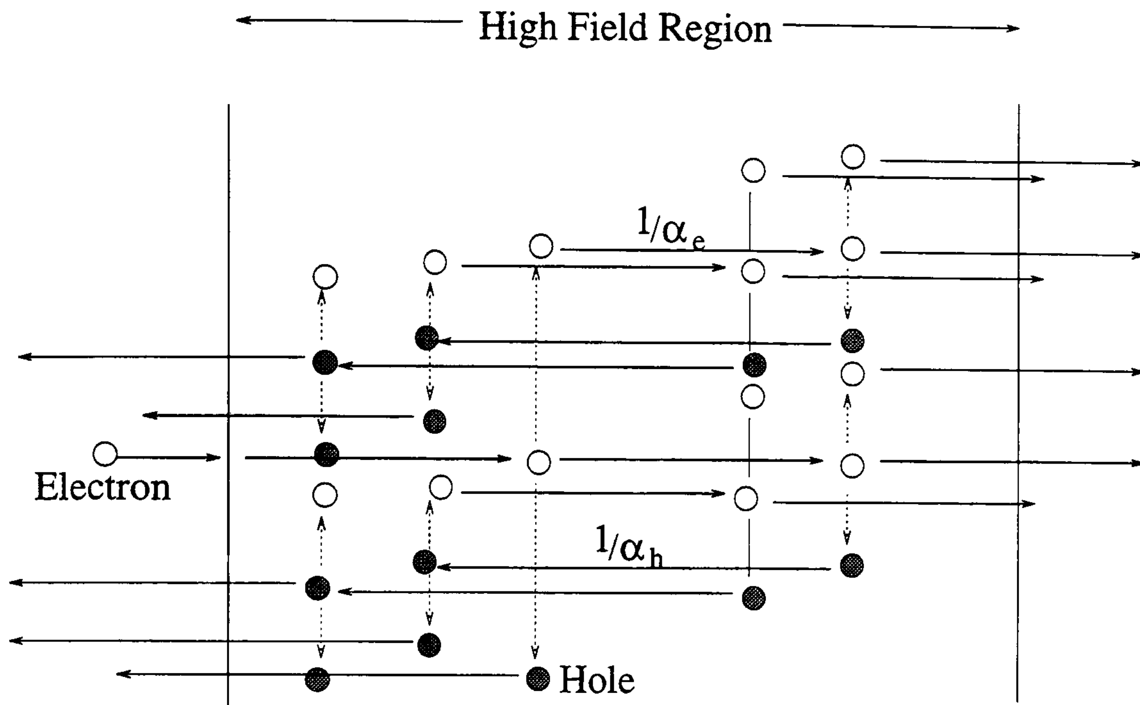

Figure 2.7: A diagram showing the formation of an avalanche where k≠0.

undergo impact ionisation. In this case avalanche breakdown will occur, the breakdown condition for electron injection, from equation 2.41, is given by equation 2.42 [31].

$$\int_0^w \alpha_e \exp^{-\int_0^w \alpha_e - \alpha_h \mathrm{d}x'} \mathrm{d}x = 1 \tag{2.42}$$

The breakdown effect is caused by the 'positive feedback' from the hole multiplication, which allows the number of charge carriers to grow infinitely in a finite distance. If k=1 then the effect of the 'positive feedback' is maximal. In this case the gain becomes extremely sensitive to the electric field strength [32], and unless the doping is extremely uniform the gain will vary across the area of the device. It is clearly beneficial to ensure that the value of k is as close to 0 as possible for electron injection (k>>1 for hole injection) to maximise the stability of the gain.

2.3.6 Excess Noise

Another important effect in avalanche photodiodes, which results from impact ionisation, is the introduction of an extra noise term due to the stochastic nature of the gain process. The total number of charge carriers produced in an avalanche will vary simply due to the statistical nature of their motion and the collision process. Thus the preceding discussions on the gain actually refer to the mean gain, the gain experienced by individual charge carriers will vary significantly. This leads to an additional source of noise in the measured signal, which is generally quantified in terms of the *excess noise factor*, F. A useful definition of F is given in [33], which defines the excess noise factor as the ratio of the total noise to the noise that would occur if the multiplication process were noiseless, i.e. with no statistical fluctuations. Mcintyre derived an equation describing the excess noise factor in terms of the ratio of the ionisation coefficients, k, and the multiplication factor, $M_{e/h}$ for electron and hole injection, equations 2.43 and 2.44 respectively [34]. For the derivation the value of k was taken to be constant, which would require a constant electric field throughout the gain region, a condition which rarely occurs in real devices.

$$F_e = M_e \left[1 - (1 - k)\frac{(M_e - 1)^2}{M_e^2}\right] \tag{2.43}$$

$$F_h = M_h \left[1 + \frac{(1 - k)}{k}\frac{(M_h - 1)^2}{M_h^2}\right] \tag{2.44}$$

It is clear from equation 2.43 that if electrons initiate the avalanche then it is desirable to have a small k value, i.e. $\alpha_e >> \alpha_h$. Conversely, if holes initiate the avalanche then a large k value is beneficial. Thus the equations re-enforce the requirement that the charge carrier initiating the avalanche should have the higher ionisation coefficient.

The repercussion of these arguments is that in silicon devices, where $\alpha_e > \alpha_h$, it is advantageous to ensure that the electrons initiate the avalanche. In addition, the

generation of charge carriers in the gain region should also be avoided. The designs of modern silicon avalanche photodiodes almost always follow these rules.

2.3.7 Ionisation Co-efficients

A large area of research is still dedicated to the study of impaction ionisation in semiconductors [35],[36],[37]. A large number of theoretical models are used to describe the process of impact ionisation. There are also many parameterisations that can be used to describe the ionisation coefficients [38]. A modified form of the Baraff three parameter theory is used to describe α_e and α_h in the simulation. The choice of parameterisation used to describe the ionisation rates is a compromise between the accuracy in the desired range, and the complexity, which limits the convergence time. The application of the modified Baraff theory is described in detail in chapter 4.

2.4 Photo-detection

There are three main types of semiconductor photo-detector; the photoconductor, the PIN photodiode and the avalanche photodiode. The PIN photodiode and the APD are both junction devices and utilise a pn junction for the conversion of the incident photons into an electrical signal. Typically junction devices are operated in reverse bias and the incident photons are collected in the depletion region. All the devices use the same fundamental process to 'collect' the incident photons, namely the photoelectric effect. The significant difference between the devices is the method used to collect the resultant photo-generated charge carriers.

2.4.1 Photoexcitation

The idea of ideal intrinsic photo-excitation was introduced in chapter 1, where a photon interacts with the semiconductor material, figure 1.3. If the energy of the photon is greater than the bandgap energy then a valence band electron will be

excited into the conduction band, creating an electron-hole pair. Extrinsic photodetectors can be used to detect photons which don't have enough energy to excite an electron from the valence band into the conduction band. In this case energy levels deep in the bandgap, introduced via doping, allow photons with an energy much less than the bandgap to excite electrons into the conduction band, and hence be detected.

An important parameter used to characterise photodetectors is the external quantum efficiency, η. This is defined as the number of charge carriers collected per incident photon and can be written in terms of the measured photocurrent and incident optical power, equation (2.45) [39].

$$\eta = \frac{I_{ph}}{q} \frac{h\nu}{P_{inc}} \tag{2.45}$$

The external quantum efficiency depends on the dimensions of the absorption or 'light collecting' region and the absorption coefficient of the material, β. The absorption co-efficient is a function of the wavelength of the incident light, hence the quantum efficiency can vary with the incident wavelength also.

2.5 Junction Photodiodes

The semiconductor junction photodiode is the most common form of semiconductor photo-detector. The devices employ a reverse biased pn junction, providing a depletion region in which the incident light is collected. Electron-hole pairs generated within the depletion region are rapidly swept apart to give rise to a measurable photocurrent. Electron hole pairs generated within a diffusion length of the depletion region can diffuse to the depletion region to be collected. The charge carriers collected via diffusion can have an adverse effect on the transient response of a device. Spurious measurements of the transient gain, made during calibration of devices for a CMS test beam, were found to be a result of a significant fraction of the signal charge being collected via diffusion [40].

2.5.1 PIN Photodiodes

The PIN photodiode was introduced in chapter 1. A schematic of a typical Si PIN photodiode structure was shown in figure 1.4. Even at relatively low electric fields, the carriers drift at their saturation velocity through the depletion region. Hence the PIN photodiode is a relatively fast device. The devices can be optimised for a particular wavelength by varying the width of the i-region. Quantum efficiencies of 80% are readily attainable throughout the optical spectrum.

2.5.2 Avalanche Photodiodes

The avalanche photodiode was briefly introduced in chapter 1. Avalanche photodiodes provide many of the advantages of the PIN photodiode with the addition of an internal gain mechanism. Gains of 10^4 are available in some devices [41],[42]. For applications where high sensitivity is required, the avalanche photodiode is a suitable replacement for the PIN photodiode.

The fundamental operation of the avalanche photodiode is very similar to the PIN photodiode. The APD is designed to provide a region of sufficiently high electric field, at operating bias, to allow impact ionisation to occur. The collected charge carriers drift to this region and initiate an 'avalanche', which amplifies the original signal. This process and its consequences are discussed in section 2.3.5.

There are a vast number of different avalanche photodiode designs that incorporate numerous materials, each optimised for different applications, generally by the wavelength of light detectable.

2.5.3 Germanium Avalanche Photodiodes

The small bandgap in Germanium allows Ge avalanche photodiodes to be use in the detection of long wavelength light, typically used in fibre optical communication. Unfortunately the small bandgap results in a very high level of thermal generation, hence leakage current. This, combined with the lack of pure substrate material, which can result in un-even breakdown in a device leading to *micro-plasmas*, means

that the gains are typically limited to < 20. Difficulties encountered in the diffusion of p-type impurites into Ge resulted in early diodes having an n^+p structure, figure 2.8. This structure does not follow the rules outlined in section 2.3.6, and carriers of the *wrong* type are amplified, resulting in poor noise performance. The use of ion-implantation has allowed this to be rectified although achievable gains are still limited.

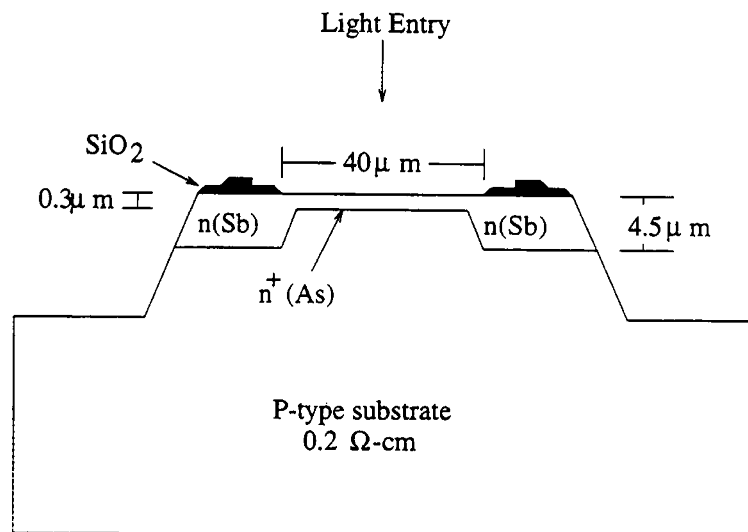

Figure 2.8: A diagram showing the structure of a Germanium diffused avalanche photodiode [1].

2.5.4 Hetero-Junction Avalanche Photodiodes

Hetero-junction avalanche photodiodes, typically using InGaAs-InP, prove to be ideal photo-detectors for optical communication. The bandgap varies with doping between 0.74 and 1.35eV, and as such a wide range of wavelengths can be detected. The devices also suffer from substrate contamination and hence values of gain are limited by the formation of *micro-plasmas*. The junction is formed in the high bandgap material, hence resulting in a small leakage current. Long wavelength detection is possible via the small bandgap InGaAs material, where light can be absorbed. To improve the response time a thin layer of quaternary InGaAsP can be inserted between the InP and InGaAs layers. The resulting devices are known as separate-absorption-graded-mutiplication (or SAGM) APDs, for example figure 2.9.

SAGM-APDs are the most efficient avalanche photodiodes currently used in optical communication systems.

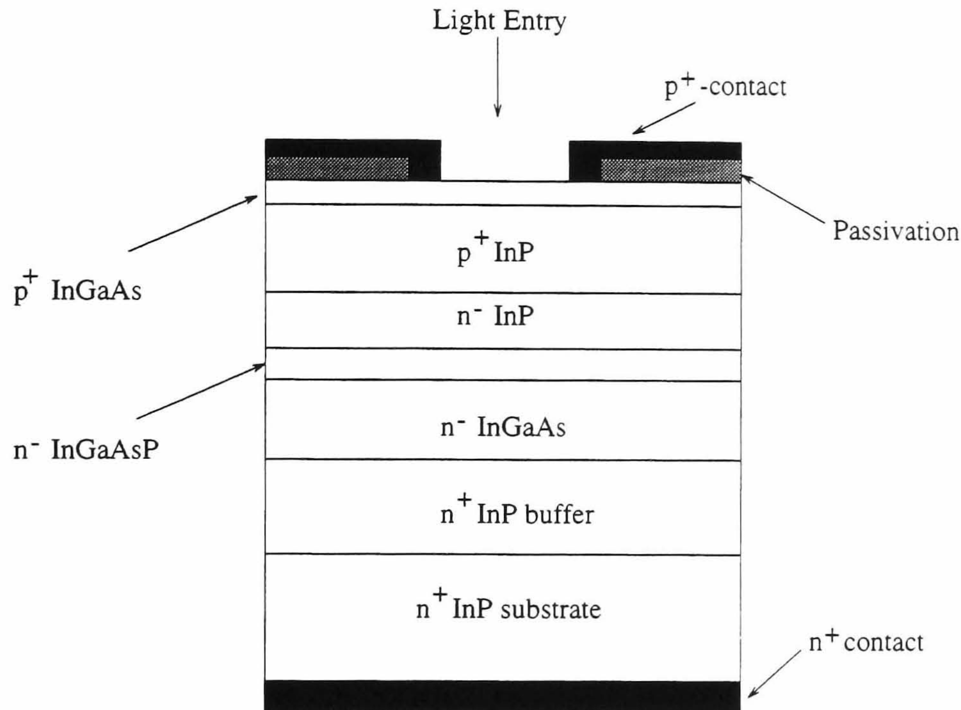

Figure 2.9: A Schematic showing the structure of an InP-based SAGM avalanche photodiode [39].

The work in this thesis is based on two silicon avalanche photodiodes; the EG&G C30916E reach through APD and the EG&G C30917F reverse reach through APD. The avalanche photodiodes utilise complementary designs, introduced in chapter 1, that will be discussed in more detail.

2.5.5 Reach Through Avalanche Photodiodes

The estimated structure of the C30916E reach through APD (as used in the reach through APD model) is shown in figure 2.10. This type of structure is common as it provides a wide depletion region for light collection, resulting in a high quantum efficiency and low capacitance. The high field region is situated at the far side of the device (shown in figure 1.7). The device is designed so that electrons, generated by photo-excitation from the incident photons, will traverse the depletion region and arrive at the gain region. This follows from previous arguments, which showed that

the charge carrier with the highest ionisation coefficient should be used to initiate the avalanche. The typical characteristics of the C30916E are shown in table 2.2 [43]. This type of structure is optimised for the detection of longer wavelengths, which are absorbed deep in the device [33].

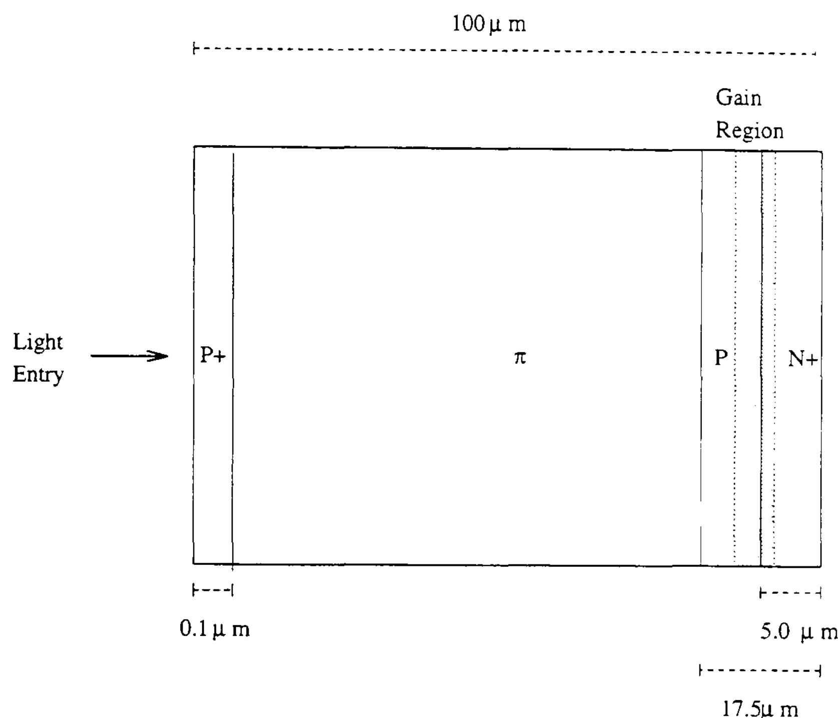

Figure 2.10: A diagram showing the estimated structure of the C30916E APD used in the reach through APD model.

The reach through structure suffers from two main disadvantages. The first is that the bulk dark current, generated in the wide depletion region, is subject to the same multiplication as the photo-generated signal. This is a problem if the devices are subject to non-ionising radiation damage, where the introduction of recombination centres leads to a substantial rise in the bulk dark current, which would then be amplified. The second arises if the device is used in scintillation applications, where the *nuclear counter effect* can become significant [44]. In this case charged particles can generate a large number of electron-hole pairs as they traverse the wide depletion region. The signal from the particles, generated over the whole depletion region, can swamp the signal from the scintillation crystals. These problems are addressed in the design of the reverse reach through avalanche

photodiode.

Device	Sensitive area /mm	Photosensitivity A/W	Dark Current /nA	Capacitance (100kHz) pF	Response Time /ns
C30916E	1.5 Dia.	70 @900nm	100	3	2
C30719F	5 × 5	16 @480nm	10	30	< 20

Table 2.2: Table showing the stated typical characteristics of the C30916E and C30719F APD at 22°C.

2.5.6 Reverse Reach Through Avalanche Photodiodes

The estimated structure of the EG&G C30719F reverse reach through APD (as used in the reverse reach through APD model) is shown in figure 2.10. The electric field profile, at operating bias, is shown in figure 1.7. It is immediately clear that the principle of the structure is similar to the C30916E, except that the gain region is shifted towards the front of the device. The structure is similar to the short wavelength selective reverse avalanche photodiode (SWS RAPD) proposed in [20].

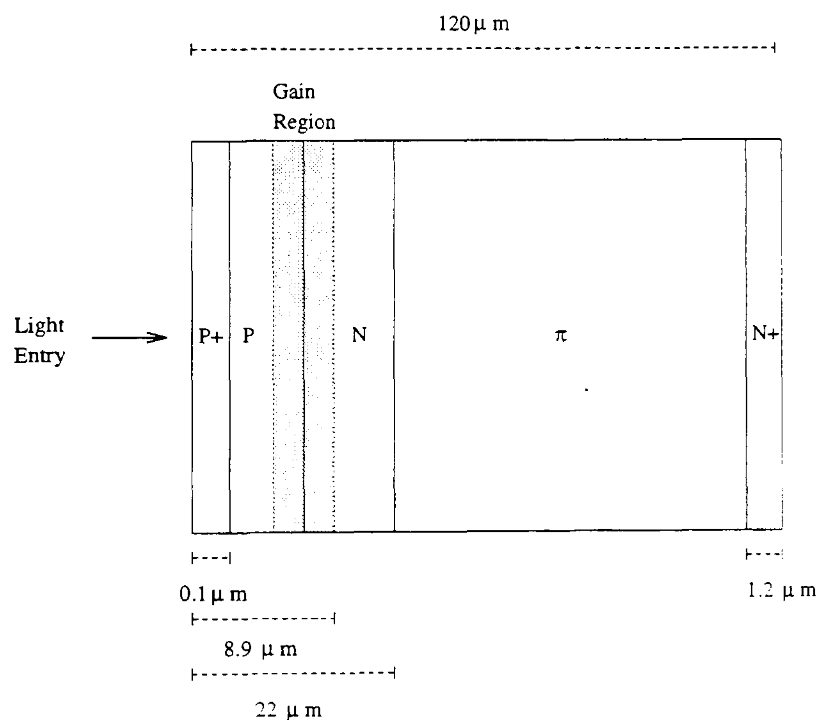

Figure 2.11: A diagram showing the estimated structure of the C30719F APD used in the reverse reach through APD model.

The design of the SWS RAPD is optimised specifically for scintillation applications, where the wavelength of the detected light is typically below 550nm. The small depletion region in front of the gain region is very narrow, of the order of a few microns. Only the dark current generated in this narrow region undergoes efficient amplification, i.e. the electron signal is amplified from this region. Multiplication of the dark current generated in the wide depletion region is negligible in comparison because the hole signal is amplified. The result is that the devices tend to be more radiation tolerant; the rise in dark current from radiation damage is compensated by the selective multiplication of the dark current. The dark current of the C30719F is shown in table 2.2; although the device has a significantly greater area than the C30916E the dark current is much smaller.

2.6 Fast Neutron Radiation Damage

Semiconductor detectors are frequently used in areas where they are subject to radiation induced damage from a range of sources. Their widespread use in HEP, commonly in the form of silicon vertex detectors where high levels of radiation are commonplace, has led to intense study into the mechanisms involved in radiation damage. Semiconductor diode detectors, in particular avalanche photodiodes, are being more frequently used in many systems in HEP detectors. These range from scintillation readout in calorimeters [45] and [46], to use in optical fibre data-bus systems [47]. Understanding the fundamental processes that lead to the observed radiation damage in semiconductor devices is vital for the prolonged use of all these systems.

The two main types of damage that commonly occur in semiconductor diode detectors can be divided into: i) surface damage and ii) bulk damage. The surface damage refers to the interaction of γ's or low energy charged particles with the surface passivation layer. This manifests itself as a reduction in the quantum efficiency and an increase in the surface current. The quantum efficiency of avalanche photo-

diodes being evaluated for the CMS ECAL was seen to fall by 50% (for blue light) as a result of damage to the SiO_2 passivation layer by a 5.5 Mrad dose of $^{60}Co\gamma$ irradiation. Replacement with Si_3O_4 passivation reduced this fall to 10% [48]. Re-calibration of the semiconductor detector can often be used to counter the effects of surface damage.

The physical processes that constitute bulk damage, in particular damage to silicon by neutrons, have only recently been understood [49]. Even now the picture is not complete. The large neutron and hadron background present in modern HEP experiments and the severity of the resulting effects has identified bulk damage as being the most significant hurdle in producing radiation hard devices [50]. Understanding the mechanisms involved, especially for silicon which is widely used, is necessary so that steps can be taken to enhance the longevity of these devices, e.g. by defect engineering.

2.7 Macroscopic Effects in Silicon

The consequences of neutron radiation damage on silicon devices are threefold:

1. a significant increase in the bulk dark current due to increased thermal generation
2. a reduction in the charge collection efficiency due to enhanced trapping
3. a change in the effective impurity concentration the cause of which is still being debated.

For avalanche photodiodes, which are operated at high reverse bias, 1 and 3 prove to be the most significant effects. The bulk dark current is found to increase linearly with neutron fluence, up to about $10^{15}ncm^{-2}$, for PIN diodes according to equation 2.46 [15]. Here V is the volume, Φ_n the neutron fluence and the value of α is approximately 4 to $9x10^{-17}Acm^{-1}$ [51], before annealing.

$$\Delta I_{Bulk} = \alpha V \Phi_n \tag{2.46}$$

This relationship was found to hold for silicon avalanche photodiodes by using the *effective depth* [45]. The *effective depth* was originally used to quantify the response to charged particles i.e. the nuclear counter effect. This was achieved by exposing the avalanche photodiodes to 2MeV electrons from a ^{90}Sr source, measuring the charge collected and normalising in terms of the charge collected by a known PIN photodiode via equation (2.47).

$$\mathrm{d}_{\mathrm{eff}} = \frac{\mathrm{d}_{\mathrm{PIN}}}{Q_{\mathrm{PIN}}} \frac{Q_{\mathrm{APD}}}{M} \tag{2.47}$$

The change in the effective impurity concentration has not been measured directly for silicon avalanche photodiodes, although the effect on the operating characteristics of the devices has been observed [15].

Much of the research in this area has been based on high resistivity silicon PIN diodes and charge-coupled-devices (CCDs) [52],[53]. It was observed that for n-type diodes the value of N_{eff}, measured from the depletion voltage, initially fell with 1MeV neutron fluence until the device became p-type. The fluence at which this occurs is known as the *inversion fluence.* N_{eff} then increased linearly with neutron fluence at a rate of 0.016cm^{-1}.

2.8 Damage Mechanism

Recent advances have been made in the understanding of the processes involved in neutron radiation damage to silicon devices [54], [55], [56], although few are directly related to APDs. Vacancy (V) and interstitial (I) type defects are created in the semiconductor lattice for many types of irradiation, figure 2.12. The significant difference between fast neutron radiation and, for example, ^{60}Co γ irradiation arises due to the large amount of energy imparted to the primary knock-on atom (PKA).

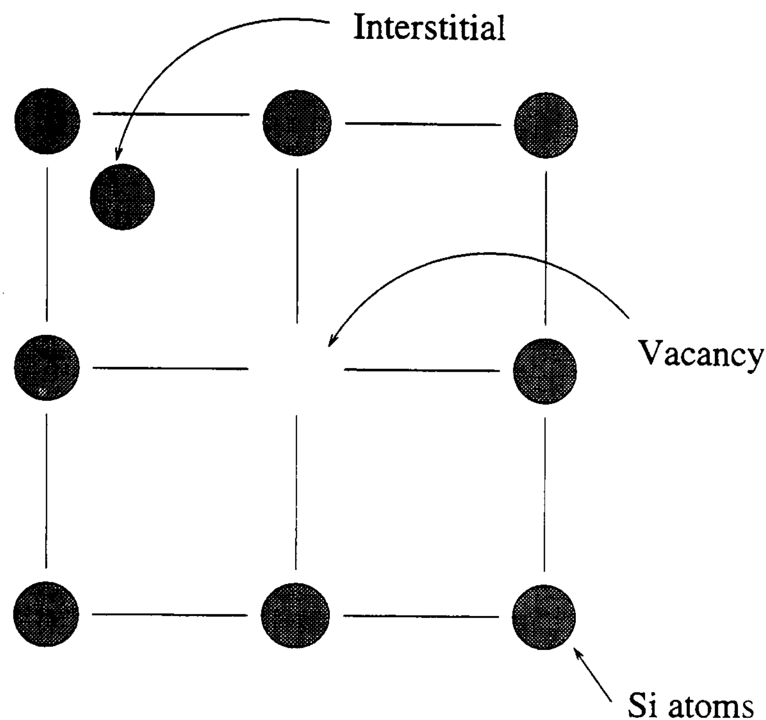

Figure 2.12: A simple schematic of the principal types of radiation induced damage to a semiconductor lattice.

The recoiling PKA goes on to create a large cluster of V and I defects (a ^{60}Co γ will only cause at most two silicon atoms to be displaced). The majority of these defects recombine immediately, the rest either form divacancies (V_2) or higher order V complexes; or the defects diffuse into the lattice and combine with impurity atoms, figure 2.13. The introduction rate is defined as the rate at which defects are introduced per unit neutron flux. For 1MeV neutron irradiation, the introduction rate for the divacancy (V_2) is approximately 100 times greater than for ^{60}Co γ irradiation [55]

Initially, for fluences below the *inversion fluence*, the change in the effective impurity concentration seen in n-type diodes was attributed to the combination of vacancy (V) defects with the phosphorus dopant atoms, producing the E-centre in silicon. It was discovered by Watts et al, that the removal rate of phosphorus in microstrip diodes was approximately 30 times lower than the level required to produce the measured change in N_{eff} [24]. A new theory was thus developed that attributed the change in N_{eff} to the creation of acceptor-like states deep in the bandgap [23].

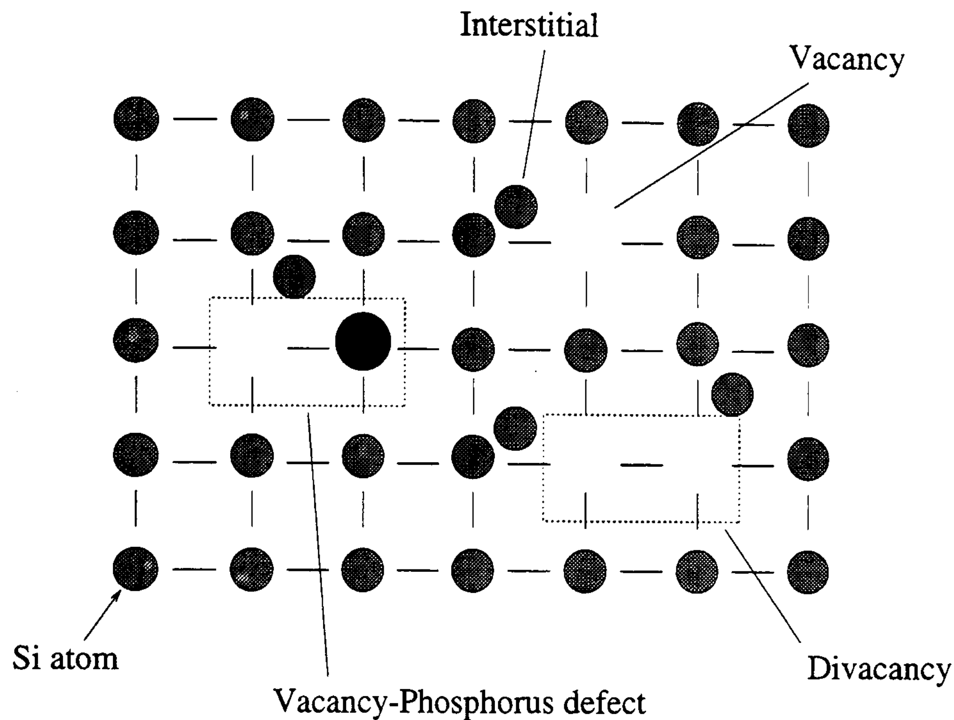

Figure 2.13: A simple schematic showing the formation of a cluster of defects caused by an incident high energy neutron.

It was known that, at thermal equilibrium, the devices became intrinsic after heavy neutron irradiation. The change in N_{eff} occurred in the intrinsic region only when the diode was reverse biased. The change in the effective doping concentration is thus a consequence of the space-charge distribution produced by the ionised deep levels.

The effects of neutron irradiation are included into the simulation via the introduction of an ionised deep acceptor concentration in the Poisson equation. The occupancy of the deep levels is described by Shockley-Read-Hall statistics, as described in section 2.3.3. The increase in thermal generation is included by modifying the minority carrier lifetime, τ, according to the lifetime-damage-constant,K_τ. The thermal generation-recombination in the simulation is controlled by the value of the minority carrier lifetime via the SRH recombination term, equation 2.30. Hence the simulation includes the effects of radiation induced generation without requiring exact information about the defects that give rise to this process. The mechanism that gives rise to the increased thermal generation is still being investigated, although

new theories have been able to describe the process well [57].

2.9 Annealing

Annealing is an important phenomenon associated with radiation damage. Many of the centres introduced during irradiation have been identified, the corresponding recovery at various temperatures has also been measured. A large area of research is dedicated to fully characterising these defects and understanding the complex processes that occur. This is a vital area of research for the comprehensive understanding of the long-term behaviour in radiation-damaged devices. The simulation presented in this thesis does not include the effects of annealing because the annealing data on the V_2O complex, the 'deep acceptor' candidate, are not yet available. Including the effects of annealing in the simulation is a worthwhile avenue for future development.

Chapter 3

Experimental Techniques

3.1 Introduction

A short experimental study was undertaken to generate results for comparison with the simulation output. Commercial devices were acquired for the study, hence little information was available regarding their exact structure, although the structure type was known and reflected the models developed. Thus the results produced in the study were intended to replicate the models' results qualitatively and not to allow quantitative comparison.

The requirements of the study were threefold:

1. to replicate the trends displayed in the simulation results for the full range of results output from the models
2. to use well know methods for the measurements
3. to employ a temperature stable environment to reduce the effects of temperature fluctuations on the results.

3.2 The Test System

3.2.1 Introduction

To satisfy the requirements outlined in the introduction a test system was built using tested hardware. The system used to apply bias to the APDs, figure 3.4, was built

according to a design used for preliminary APD measurements for the CMS ECAL [58]. A pulsed LED system was used in the measurement of the excess noise factor. The simple pulse system, figure 3.6, was also based on a design used in preliminary APD evaluation for the CMS ECAL [58].

3.2.2 Temperature Control

A temperature control system was used to allow accurate control of the level and stability of the temperature to ±0.1 °C in the test environment. This was based on a system used in the temperature control of a stabilised blue illumination system [59]. The APD temperature control system utilised a CAL 9900 PID temperature controller, [60], and a Peltier heat pump.

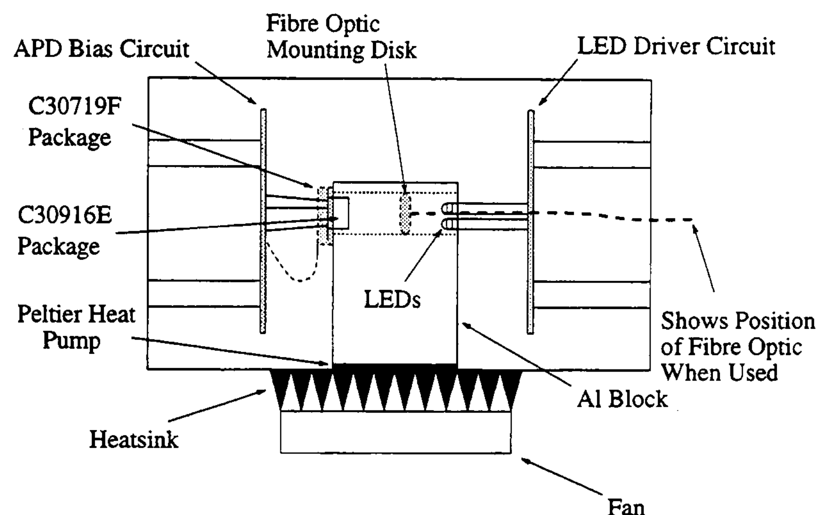

Figure 3.1: Diagram showing the layout of the APD test box.

The test circuitry was mounted in an insulated di-cast aluminium box, figure 3.1. The Peltier heat pump was attached to a small aluminium block using a thermally conductive silicon compound. The aluminium block surrounded the APD and illuminating LED, as shown in figure 3.2. This arrangement also allowed good control of the LED temperature during excess noise factor measurements. A PT100 sensor, used by the temperature controller, was mounted on the aluminium block as close as possible to the APD. This increased the response of the temperature controller to

small changes in APD temperature. The stability of the temperature was recorded over a short period after the temperature had stabilised, figure 3.3.

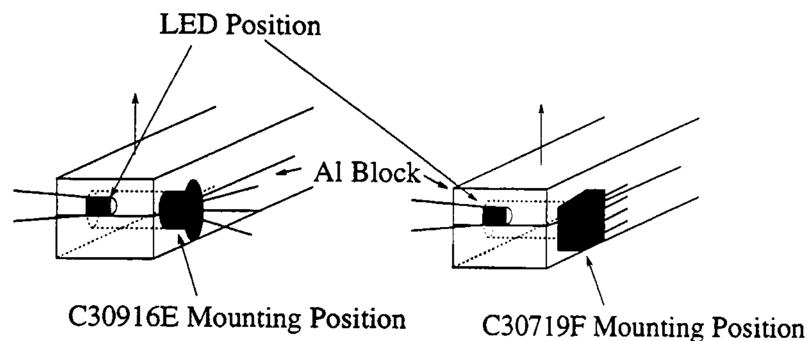

Figure 3.2: Diagram showing the position of the LED and APD in relation to the Aluminium cooling block

Cooling the APD is necessary to reduce the dark current, this is essential for the post-irradiation results. The dark current increases substantially due to the defects introduced during the irradiation; reducing the dark current increases the resolution of the photocurrent measurements. Cooling is also beneficial in the measurement of the excess noise factor as the shot noise, introduced by the dark current, can be significantly reduced.

The APDs were cooled to 10°C. The constraints that affected the choice of temperature are listed below.

- The ambient temperature of the laboratory varied substantially during the day due to heating from the equipment and from day to day depending on the external temperature. Thus a temperature that could be consistently reached and maintained over a wide range of ambient temperatures was required.

- Due to the high humidity at the time of the experiments , condensation forming inside the test box was a potential problem. A lower temperature constraint was set by the formation of condensation. This was reduced by the use of Silica gel packs in the test box and a de-humidifier in the laboratory.

- The temperature controller could not maintain the required stability at temperatures close to ambient. Thus, the temperature controller set an upper

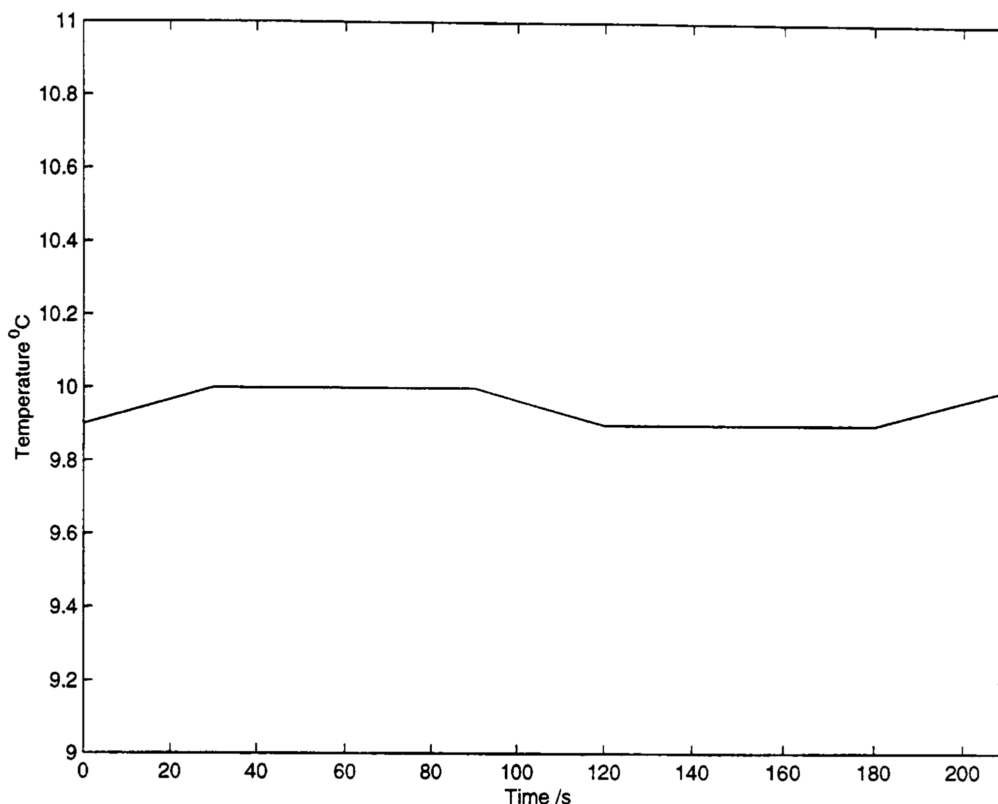

Figure 3.3: Plot showing the short term stability of the temperature control system

temperature constraint, this varied with the day-to-day ambient temperature.

The lower temperature constraints were the most significant in the selection of a suitable temperature. The temperature controller could comfortably maintain a temperature approximately 20°C below ambient. Thus on a 'cold' day a temperature just above 0°C was possible. Condensation proved to be a problem at this temperature. A temperature of 10°C was chosen as this was easily maintained by the temperature control system, with minimal formation of condensation. It also ensured that the temperature could be repeated if the ambient temperature rose significantly.

3.2.3 Bias Control

Bias was applied to the APD using a simple circuit, figure 3.4. The high precision 100k resistor in series with the APD allowed the current passing through the APD to be measured. The 10M resistor in series with the APD acts in a passive

quenching role. It is common to employ some form of quenching, whether active or passive, when using devices with gain to prevent an excessive current build up causing damage to the device. The passive quenching circuit works simply as a potential divider, if the current through the APD becomes very large, e.g. at breakdown, then the potential across the quenching resistor increases, reducing the APD bias and preventing the onset of breakdown.

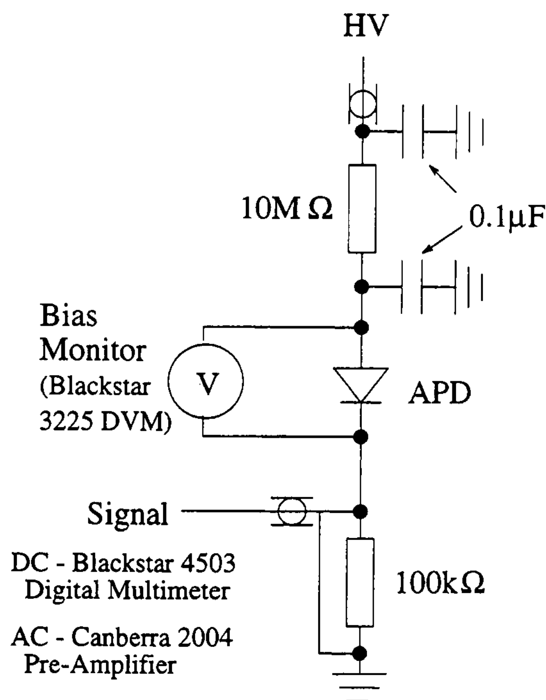

Figure 3.4: Schematic of the APD bias circuit.

3.2.4 Illumination

The measurements performed on the devices required the use of both continuous and pulsed illumination. The continuous illumination system was required to provide a set of known wavelengths in the optical range. A monochromator feeding a plastic fibre optic cable was fed into the test system, figure 3.5. This provided the required range of wavelengths, selected via a vernier scale, allowing simple and accurate changes to the illumination wavelength. The pulsed illumination system, used solely for the excess noise factor measurements, utilised LEDs. These are easily driven and have been used by a large number of groups for such measurements [61].

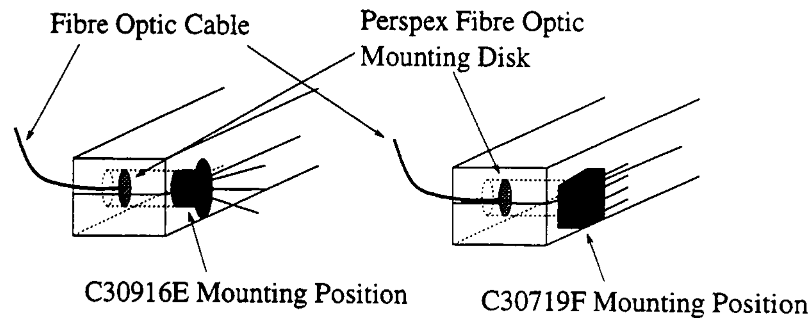

Figure 3.5: Diagram showing the method used to mount the fibre optic cable

Continuous Illumination

The continuous illumination system was used for the majority of the APD tests; including the gain and photosensitivity measurements. The requirements of the system are listed below.

- To provide easily selectable monochromatic illumination at a variety of wavelengths in the optical range.
- To cause minimal intrusion to the test environment such that the temperature stability was not degraded.

The second requirement was satisfied by the use of an optical fibre, which was fed into a small hole in the test system. This separated the test environment from any heat emitted from the light source and had a minimal effect on the test environment structure.

The use of a fibre optic feed allowed the second requirement to be satisfied in two ways:

1. use a single light source capable of generating monochromatic illumination over a wide range of wavelengths e.g. a monochromator.
2. use several light sources with filters to produce monochromatic illumination.

A Hilger and Watts, 1 meter focal length, f/10 grating monochromator was chosen as it provided the simplest method for wavelength selection. The monochromator

employed a Xe arc lamp, producing a large amount of ultraviolet. A 420nm long-wave pass filter was employed to ensure that a minimal amount of UV was allowed to pass into the fibre optic and thus reach the APD.

Care had to be taken during the measurements using the continuous illumination system to minimise contamination in the fibre optic from external light sources. The optical laboratory benefited from window covers and during the measurements the lights were switched off. Even a small amount of background light had a significant effect on the measurements, in particular for the evaluation of the dark current.

Pulsed Illumination

Measurements of the excess noise factor utilised pulsed LED illumination, the driver circuit for the LED is shown in 3.6. This provides a very fast pulse, approximately 20ns rise time and 25ns decay time constant, to the LED.

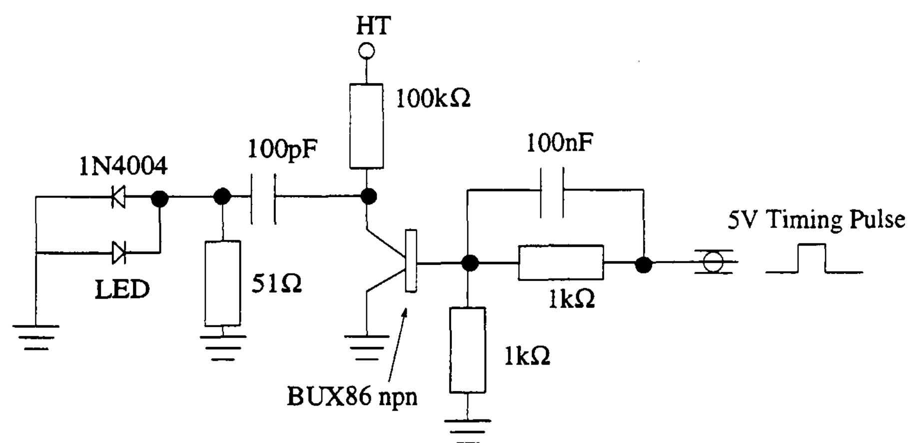

Figure 3.6: Schematic of the LED pulser circuit

The output pulse from the APD was fed into a Canberra Model 2004 semiconductor detector pre-amplifier [62]. The high gain setting of 1.0V/pC was used. This allowed the LED output to be reduced, minimising the effects of jitter from the LED [63]. The voltage dropped across the LED, hence the intensity of the LED pulse, was controlled using the HT power supply. An EG&G Ortec 485 shaping amplifier was used with a $0.5\mu s$ shaping time constant and coarse gain of 100. An ACE ADC card, housed in a PC running Maestro II pulse height analysis software, was used

to analyse the output pulse. This allowed accurate measurement of the width and amplitude of the APD output pulse height distribution.

The choice of wavelength for illumination was important; the generation of signal charge in or beyond the gain region increases the excess noise factor [63]. Thus absorption of the incident light in front of the gain region was required. Monochromatic illumination was not essential as long as the incident spectrum only included wavelengths absorbed in front of the gain region.

LEDs provide an ideal source of pulsed illumination, allowing simple control of the pulse width and amplitude and available with a wide range of output spectra. They have been widely used in excess noise measurements using well documented techniques [64],[65]. A Kingbright L934SED diffused blue LED, with a peak wavelength at 430nm, was used as a light source for the excess noise factor measurements.

The system used to pulse the LEDs was successfully employed in preliminary APD tests [66]. The design allows the charge stored in a capacitor to be discharged through the LED, providing a fast and stable pulse over a wide range of frequencies. A Thandar TG105 pulse generator was used to control the pulse frequency.

The LEDs were mounted inside the test environment, figure 3.2, thus were subject to the same temperature control as the APDs. This ensured that the experimental conditions were as consistent as possible between measurements. The close proximity of the LEDs to the APDs allowed them to be driven with a low intensity. This was necessary as the illumination level had to be chosen as a compromise between the effects of LED jitter and photon statistics. A small signal, equating to approximately 10^4 photons, was used.

Spectrophotometer

The photosensitivity measurements required calibration of the incident illumination intensity from the monochromator. This was achieved by the use of a spectrophotometer which utilised a calibrated Hamamatsu S1337-66BR PIN photodiode and high gain current-to-voltage amplifier. The gain of the amplifier was known and

hence the photocurrent of the PIN photodiode was easily determined. The known quantum efficiency of the PIN photodiode allowed the incident illumination intensity to be determined at the required wavelengths.

The calibration could not be carried out *in situ* in the test box. Thus to ensure that the measured intensity correctly matched that incident on the APD, a mock-up of the cooling block was made. The fibre optic cable was located using a small Perspex disk. The intensity of the incident light, at all the necessary wavelengths, could thus be determined and the fibre optic cable re-mounted in the test box for measurements.

3.3 Experimental Procedures

3.3.1 Introduction

A vast amount of experimental work on APDs has occurred since the decision to use APD technology in the CMS ECAL. The purpose of the experimental study was to provide a wide range of results from the use of 'well known' techniques. To this end, the methods presented here are based on prior experiments where the results and techniques have been published.

The evaluation of the devices consisted of three key areas:

- the constant illumination gain
- the photosensitivity
- the excess noise factor.

The equipment used in the measurements has been described in detail. This section will introduce the methods used to characterise the devices.

3.3.2 The Constant Illumination Gain

The APD gain is evaluated using a commonly employed technique [67], [68]. The dark current of the APD is recorded, over the full range of bias. The device is

then illuminated and the total current recorded. Subtracting the dark current thus provides the photocurrent. A bias is selected such that the gain of the device is unity and optimal detection of the incident light occurs. The photocurrent at this bias is taken to be the un-multiplied photocurrent, injected into the gain region. The gain of the device is now easily determined from the ratio of the un-multiplied photocurrent and the remaining photocurrent values.

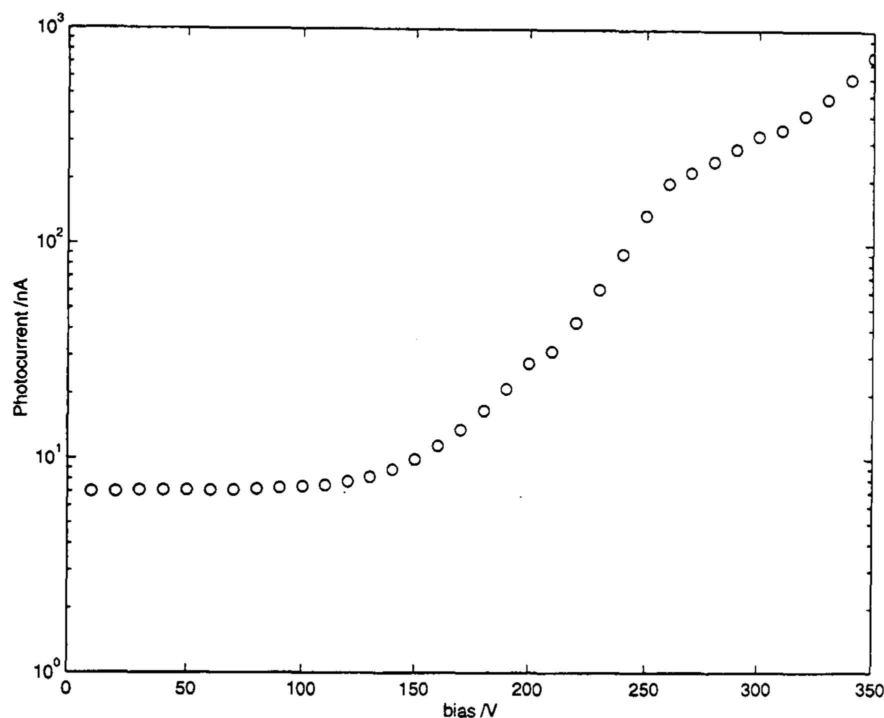

Figure 3.7: Figure showing the variation of reach through APD photocurrent with bias.

A typical reach through APD photocurrent plot is shown in 3.7. The structure of the curve is quite pronounced. The initial rise in the photocurrent is slow, leading to a 'plateau', which occurs prior to the onset of gain. The slow initial increase is due to depletion spreading through the device, and a subsequent increase in the photo-generated charge that is collected. Just before the sharp rise, attributed to the gain, the plateau indicates that an increase in bias does not increase the charge collection efficiency, hence the charge collection efficiency is at its maximum. Thus the un-multiplied photocurrent in this region is taken to be valid for the whole bias range.

3.3.3 Photosensitivity

The Photosensitivity of the devices was evaluated using a spectrophotometer, section 3.2.4. The spectrophotometer was used to measure the light intensity output from the monochromator. The photosensitivity was determined by measuring the unmultiplied photocurrent, as described in section 3.3.2, and using equation (3.1). Here I_{APD} is the measured APD photocurrent, V_{PIN} the voltage measured from the current-to-voltage amplifier with gain G_{AMP}, ϵ_{PIN} the known PIN quantum efficiency, $E_\gamma(\lambda)$ the photon energy and q the electronic charge.

$$\text{Photosensitivity} = \frac{I_{APD}\epsilon_{PIN}G_{AMP}q}{V_{PIN}E_\gamma(\lambda)} \tag{3.1}$$

3.3.4 Excess Noise Factor

The excess noise factor is a fundamental characteristic of APD performance and hence has been measured by many groups. The Webb method, [69], used in the evaluation of APDs for the CMS ECAL , [64], was employed in this study. The variance of the APD output can be written as:

$$\sigma^2 = M^2FN + \sigma_{\text{sh}}^2 + \sigma_{\text{amp}}^2 \tag{3.2}$$

where σ_{sh} represents the shot noise, $\sigma_{\text{amp}}$the electronic noise, M the APD gain, F the excess noise factor and N the number of injected charge carriers. M^2FN represents the noise due to the statistical fluctuations in the gain.

The electronic and shot noise can be simultaneously measured as the white noise, σ_{w}, of the system, via a known test charge injected into the amplifier chain. This is achieved using a range of calibrated capacitors. Thus equation (3.2) can be rewritten as:

$$\sigma^2 = M^2FN + \sigma_{\text{w}}^2 \tag{3.3}$$

By substituting $M = X/N$, where X is the APD output signal, and substituting the Mcintyre approximation, for $M > 10$, we can write:

$$\sigma^2 = \left(\frac{X}{N}\right)^2 (2 + kM)\, N + \sigma_{\mathrm{w}}^2 \tag{3.4}$$

Equation (3.4) can be re-arranged to give:

$$\frac{\sigma^2 - \sigma_w^2}{X^2} = \frac{2}{N} + \frac{Xk}{N^2} \tag{3.5}$$

A plot of $\frac{\sigma^2 - \sigma_w^2}{X^2}$ against the pulse height, X, will result in a straight line plot. Substituting k, evaluated from the gradient, back into the Mcintyre equation leads to the excess noise factor, F.

3.3.5 Errors

The main sources of error throughout the DC measurements were the 1% error on the resistor used to measure the APD current and the precision of the voltmeter used to measure the potential drop across the resistor. At the lowest current values (~1nA) the error on the voltage measurement dominated, resulting in an uncertainty of about 5% in the measured current. As the current increased ($>$ 100nA) the error on the resistance dominated, leading to an uncertainty of 1-2%. The error in the evaluation of the DC gain is not only affected by the error in the photocurrent measurement but also from the selection of the un-multiplied photocurrent. From the systematic errors in the photocurrent measurement, the error on the gain lies in the range 3-5%. The inherent problems in identifying the true un-multiplied photocurrent, discussed later in chapter 5, are also the source of a large error in the gain measurement.

Evaluation of the photosensitivity required the incident flux on the APD to be determined. The flux could only be measured to the level of the known quantum

efficiency of the PIN diode (~5%), and when combined with the error on the photocurrent measurement this results in an overall uncertainty of approximately 5-6% on the photosensitivity measurement.

3.3.6 Post Irradiation

To provide experimental comparison with the predictions made by the models, the C30916E and C30719F APD's were irradiated at the Rutherford Appleton Laboratory's ISIS facility [70],[71]. ISIS is a neutron spallation source and generates neutrons by bombarding a heavy metal target, e.g. tantalum, with protons from an 800MeV synchrotron. For general irradiation a sample is transported via an 'endless' chain system to approximately 30cm above the target. The energy spectrum received by the samples peaks at approximately 1MeV, falling by a factor of 5 by 0.1MeV and 10MeV.

The measurement of the neutron fluence received by the samples is achieved by the activation method. The technique uses cobalt foils, which are irradiated along with the samples. Thus an accurate measurement of the fluence received by the samples is available from the ISIS facility. The gamma dose received by the samples is estimated to be 10% of the total dose received [72].

The fluence received by the devices was selected as a compromise between maximising the effects due to the irradiation and not damaging the device. EG&G C30626E devices were also irradiated at the ISIS facility and suffered terminal damage to the internal bonding [73]. [74] also compared the results from biased and un-biased devices. They did not find any significant difference in the results, indicating the application of bias had little effect on the damage introduced during irradiation. The devices irradiated in this study were also unbiased during the irradiation.

The same methods and equipment were used to evaluate the devices after the neutron irradiation. The design of the test facility was influenced to ensure that no changes would be required to the test equipment, thus ensuring consistency in

the results. The devices were stored in a freezer between measurements during the post-irradiation testing at Brunel. Typically the measurements lasted 30 minutes, and during the measurements the APDS were cooled to 10°C.

Post irradiation measurements of the excess noise factor were found to be impossible due to the massive increase in the shot noise from the dark current. Evaluation of the width of the APD output pulse could not be accurately determined from the PHA software.

Chapter 4

Simulation of Avalanche Photodiodes.

4.1 Introduction

The rapid development of ever more powerful computers has been closely followed by an explosion in the use of computer simulation. With computers such a key part of all kinds of modern research, it is hard to believe that their development has spanned only the last fifty years. Modern software ranges from *finite element analysis* of the largest structures to *Monte Carlo* methods employed in the understanding of *High Energy Physics.* The computer has probably become the most versatile tool available to the scientist.

Simulation has often been used to gain physical insight into a problem, either by visualisation of the results or by uncovering the underlying mechanics behind a process. The key attribute that has led to its success is the "what if ?" scenario. Once a model has been constructed, a change in the conditions can often be used to infer further information about a system. This is quite often prompted by the thought "what if ..? ". It is this dynamic nature that makes simulation such a powerful tool.

One area where simulation has taken a strong foothold is in semiconductor device and circuit modelling. Many types of model are available; from the classical drift-diffusion model, where flow of charge is considered, to Monte Carlo methods that follow individual charge carriers through a device. Table 4.1 outlines a few of the available types of model.

The simulation described in this thesis is based on a a drift-diffusion fomulation, which has been applied to many semiconductor problems [75],[76],[77],[78]. The non-linear mathematics that are required are difficult to solve analytically without making broad assumptions. This is where numerical methods can be effectively used. Before describing the simulation in detail it is first necessary to understand the function of the component parts. Figure 4.1 shows how the different parts interact.

The software described here has been developed over the past two years by the

Type of Model	Main Features
Drift/Diffusion	Deterministic, semiconductor equations used to describe flow of charge.
Monte Carlo	Stochastic, random motion/interaction of charge carriers incorporated into the classical motion of the charge carriers.
Quantum Mechanical	Quantum mechanical effects included in the description of the charge carrier interactions, e.g. tunnelling.

Table 4.1: table showing some of the available types of semiconductor device model and their main features

author. It consists of several packages used to create and analyse pn junction devices, including avalanche photodiodes. Once a device has been created the structure plus analysis software can be considered a model. This chapter will aim to describe in detail how the component parts of the software work. The models will be discussed in chapter five with the results of the simulation.

4.2 APDSIM

4.2.1 Introduction

APDSIM is the most important piece of software. It provides fundamental information about the device under investigation. The software can simulate a range of external influences, including bias, illumination and neutron irradiation. These can be easily controlled by the user and allow a wide range of possible investigations to be performed on a particular device structure.

APDSIM applies the methodology proposed by Kurata [79]. This provides a reasonably detailed account of a one-dimensional model of a pn-junction. A one-dimensional form is able to simulate the majority of standard tests performed on APDs whilst retaining a level of simplicity that allows new structures to be evaluated

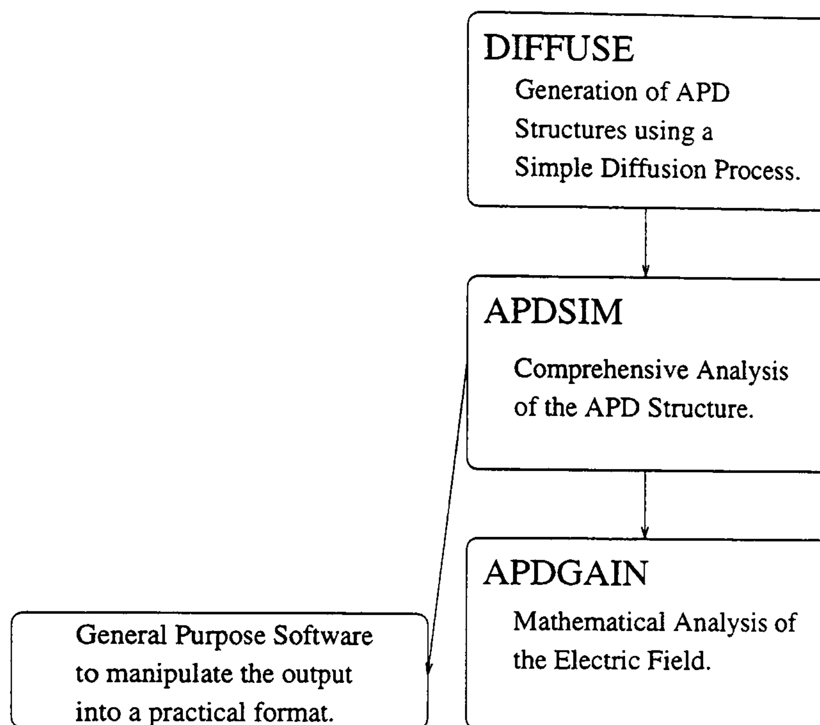

Figure 4.1: Schematic of the interaction between the individual programs that are used in the simulation.

relatively quickly. Implicit integration, a numerical technique, is used to solve the semiconductor equations across the user-defined structure. The implicit technique involves solving the semiconductor equations by generating a set of linear simultaneous equations. These may be expressed in a simple matrix form; $[A][X] = [B]$. Applying finite differences to the non-linear semiconductor equations allows a set of linear simultaneous equations to be generated. The set of approximated simultaneous equations are then solved using Newton's Iteration Principle.

Solution of the equations provides the free electron and hole concentration and electrostatic potential through the device. The current density and electric field can be subsequently inferred. The current density provides the only route for direct comparison with measurements. When combined with the external conditions e.g. applied bias and illumination, quantities such as gain, dark current and photocurrent can be predicted. The electric field profile can also be analysed to calculate the multiplication and excess noise factor for the particular device.

This process is extremely mathematically intensive, involving a matrix of order

2000 for a typical grid size. The use of a powerful workstation is essential to make the simulation practical. A Digital ALPHASTATION 233 workstation was employed to run the software. The length of a typical job was kept down to several days to produce a full range of bias, illumination and irradiation data.

The following sections will explain each step of the calculation in detail. The forms of the physical parameterisations will be described and the limitations of the simulation discussed.

4.2.2 Semiconductor Equations

The semiconductor equations employed in the simulation were in the standard form (see section 2.2.1):

$$\frac{1}{q}\frac{\mathrm{d}\vec{J}_p}{\mathrm{d}x} - (G - U) = 0 \tag{4.1}$$

$$\frac{1}{q}\frac{\mathrm{d}\vec{J}_n}{\mathrm{d}x} + (G - U) = 0 \tag{4.2}$$

$$\frac{\mathrm{d}^2\psi}{\mathrm{d}x^2} = -\frac{q}{\varepsilon}(\Gamma + p - n - \sum N_A + \sum N_D). \tag{4.3}$$

Here $\Gamma = N_d - N_a$, and $\sum N_A$and$\sum N_D$ are the ionised deep acceptor and hole concentrations respectively.

The high grid density in the gain region allowed the assumption that the electric field was constant over the range of one grid space. This allowed the integral form of the current equation [80] to be used to increase the stability of the solution in regions of high electric field [79] inherently present in an APD:

$$\vec{J}_p = -\frac{q\mu_p E}{1 - e^{\theta E x}}\left[p(0)e^{\theta E x} - p(x)\right] \tag{4.4}$$

$$\vec{J_n} = -\frac{q\mu_n E}{1 - e^{-\theta Ex}} \left[n(0)e^{-\theta Ex} - n(x) \right]. \qquad (4.5)$$

4.2.3 The One-Dimensional Grid

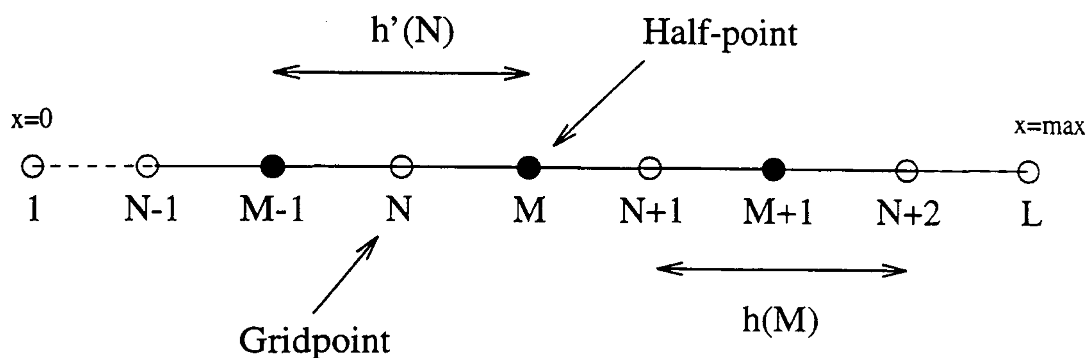

Figure 4.2: A schematic of the grid composition used in the discretisation of the semiconductor equations.

Finite differences are used to express the semiconductor equations in a linear form. Application of finite differences involves representing the device structure as a one-dimensional grid, figure 4.2, each grid-point containing information about the potential and free carrier concentration. Using half-points for the evaluation of derivatives is recommended to increase the accuracy of the difference approximation [79].

A non-uniform grid spacing allows the efficient distribution of grid-points along the device structure. The high potential gradient in the gain region benefits from an increased grid density, while the bulk of the device can be adequately discretised at a lower level. A typical array consists of 2000 gridpoints, 1000 in the first 20% of the device surrounding the active region and the remaining 1000 spread uniformly across the final 80% of the device.

4.2.4 Grid Parameter Selection

The design of the grid forms an essential part of the simulation that can often be overlooked. It usually involves accounting for device specific properties to help fine

tune the simulation into a working model.

The number of grid points in the simulation determines the overall accuracy that is attainable. The truncated Taylor expansion is used to derive the spatial derivatives in the simulation, equation (4.7), and is the dominant source of error. For a first order approximation the error is of the order of the grid size itself, equation (4.6) [81].

$$\text{Error} = \frac{1}{h}\left[\frac{h^2}{2!}f''(x) + \cdots\right] \tag{4.6}$$

Thus reducing the grid-spacing will increase the accuracy of the simulation but at the expense of increased computation time. At a certain point truncation errors in the computer will begin to dominate and decreasing the grid-spacing further will not benefit the accuracy.

The detailed structure of the grid can also be manipulated to improve the accuracy and convergence properties of a model. A non-uniform grid was investigated due to convergence problems with the EG&G reverse reach through APD. The selected grid structure was chosen due to stability of the convergence over a wide range of incident wavelengths. Several structures were investigated and the 80%/20% split was found to allow wavelengths in the range 400-800nm to be investigated fully. Other constructs suffered from non-convergence at either long or short wavelengths.

To select a suitable number of grid points, simulations were run utilising grids ranging from 500 to 3000 gridpoints. The simulations were performed using a reverse reach through structure, which is discussed in detail in chapter 5. Figure 4.3 shows how the calculated potential at one point in the structure varies according to the number of grid points used in the difference approximation. Table 4.2 outlines the number of steps and the convergence time for each size of grid. It is clear from Fig 4.3 that above 2000 gridpoints the value of the potential begins to stabilise. The same effect is seen to occur for the carrier concentrations. A large increase in convergence time, mainly due to extra processing, is seen from 1000 to 2000

gridpoints. A smaller but not insignificant increase in the convergence time is also observed when increasing from 2000 to 3000 gridpoints. Thus a grid containing 2000 gridpoints was chosen as this appeared to give the best compromise between convergence speed and accuracy.

Gridpoints	Number of Steps	Convergence Time (s)
500	20	12
1000	12	17
2000	21	52
3000	22	77

Table 4.2: Table showing the convergence steps and time for various grid sizes

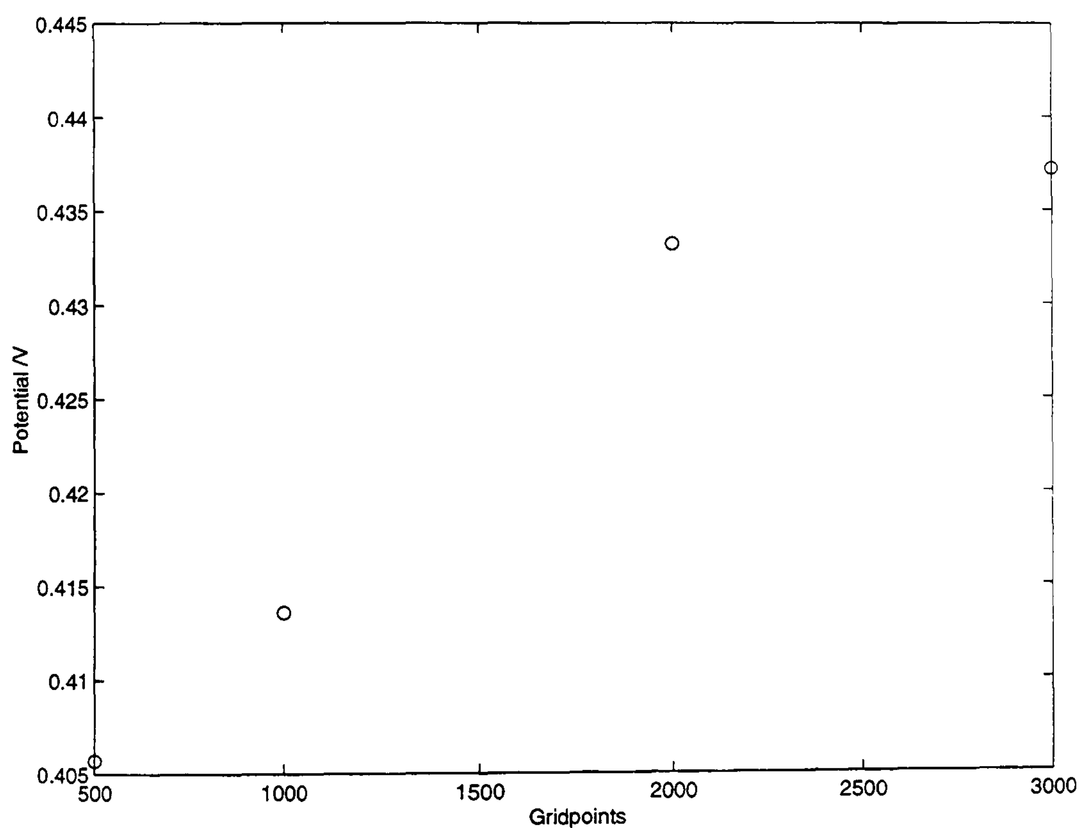

Figure 4.3: Figure showing the potential variation at one grid point with increasing grid size.

4.2.5 Discretisation Error

As mentioned in the previous section the dominant source of error in the simulation arises from the granularity of the grid spacing. The finer the grid, the closer the finite-difference approximation is to the *real* set of equations being solved. The accuracy of the solution, for a particular grid spacing, can be set at a very high level (as is the case here, see section 4.2.9) so that the error in the solution to the finite-difference approximation can be considered negligible. Of course this is just the level of accuracy to which the approximation has been solved. The level at which the approximation equates to the real *equations* determines the overall accuracy, and this is known as the discretisation error.

Figure 4.4 shows the mean relative shift in the solution across the reverse reach through structure, for each of the fundamental parameters, as the number of grid-points is increased from 500 to 3000. The plot shows that a finite difference approximation using 500 or 1000 gridpoints is clearly too coarse to provide an accurate solution in this case. The shift from 2000 to 3000 grid points is of the order of a few percent for the free carrier concentrations, and about 6% for the potential. The plot indicates that the discretisation error should become negligible between 3000 and 4000 gridpoints, thus we can prudently estimate for 2000 gridpoints, the level of discretisation error to be of the order of 5% for the carrier concentrations and 10% for the potential.

4.2.6 Application of Finite Differences

To apply the time-independent semiconductor equations to the grid requires that they are expressed in a discrete form, i.e. discretised. This is achieved by expressing the spatial derivatives, at gridpoint M, via a truncated Taylor series, equation (4.7).

$$\frac{\mathrm{d}p}{\mathrm{d}x}(M) = \frac{p(N+1) - p(N)}{x(N+1) - x(N)} \tag{4.7}$$

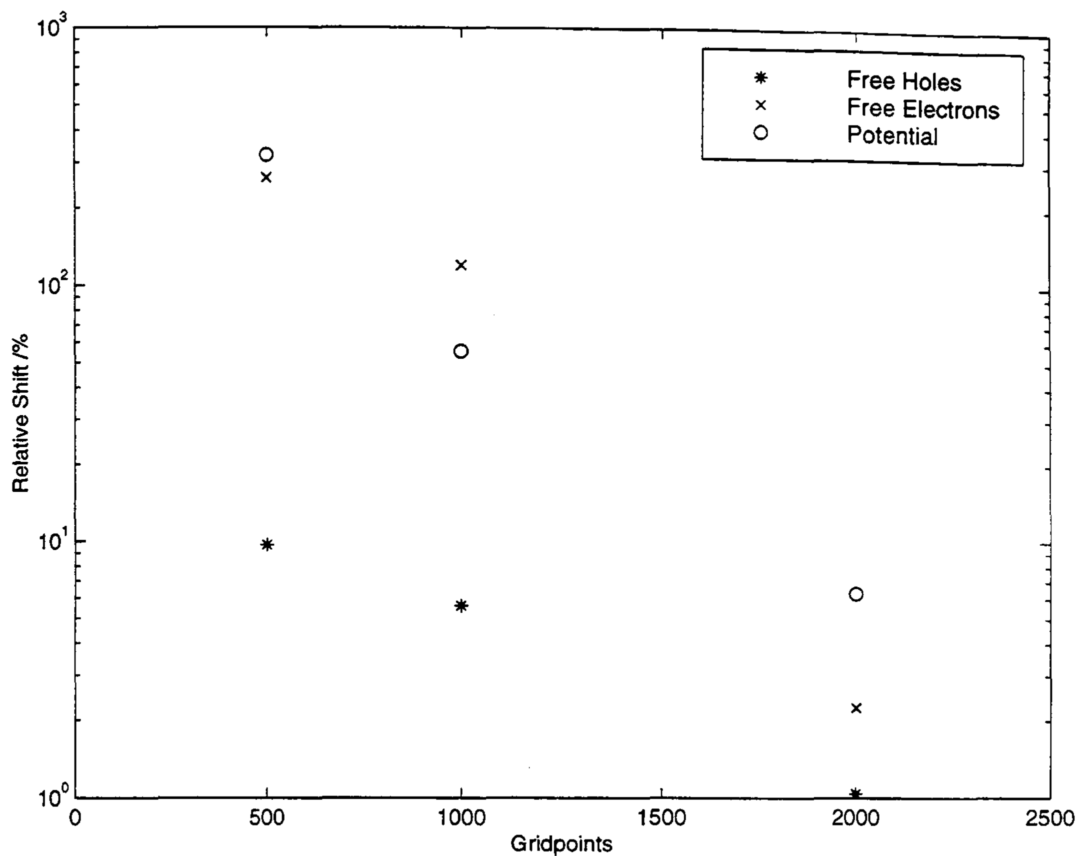

Figure 4.4: Figure showing the mean relative shift in solution for each of the fundamental parameters as the grid size is increased from 500 to 3000 grid points.

Thus a first order difference approximation is used. The discretised equations can be written explicitly:

$$J_p(M) = \frac{q}{h(M)}\Big[\mu_p(M)\frac{\psi(N)-\psi(N+1)}{1-exp^{-\beta(M)}}p(N) + \mu_p(M)\frac{\psi(N)-\psi(N+1)}{1-exp^{\beta(M)}}p(N+1)\Big] \quad (4.8)$$

$$J_n(M) = \frac{q}{h(M)}\Big[\mu_n(M)\frac{\psi(N)-\psi(N+1)}{1-exp^{\beta(M)}}n(N) + \mu_n(M)\frac{\psi(N)-\psi(N+1)}{1-exp^{-\beta(M)}}n(N+1)\Big] \quad (4.9)$$

$$\frac{1}{q}\frac{\vec{J_p}(M)-\vec{J_p}(M-1)}{h'(N)} - G(N) + U(N) = 0 \quad (4.10)$$

$$\frac{1}{q}\frac{\vec{J}_n(M) - \vec{J}_n(M-1)}{h'(N)} + G(N) - U(N) = 0 \tag{4.11}$$

$$\frac{1}{h(M-1)h'(N)}\psi(N-1) - \frac{1}{h'(N)}\left[\frac{1}{h(M-1)} + \frac{1}{h(M)}\right]\psi(N) + \frac{1}{h(M)h'(N)}\psi(N+1) = -\frac{q}{\varepsilon}\Big[\Gamma(N) + p(N) - n(N)\Big]. \tag{4.12}$$

Here $beta(M)$ is defined as $E(M)h(M)\theta$. It should be noted that although derivatives are evaluated at half-points, second derivatives, which occur in the Poisson and continuity equations, are evaluated at the main grid-points.

4.2.7 Linearising the Discretised Equations

Newton's iteration principle is now used to express the equations in a linear simultaneous form. This involves expressing the true value of each of the fundamental variables in terms of the present value plus an associated error or increment; e.g. for the hole concentration:

$$p_{true} = p^0_{initial} + \delta p. \tag{4.13}$$

the individual terms in the equations are expanded via a truncated Taylor expansion in terms of the known value and associated increment; e.g. for the hole current density:

$$J_p(M)\Big\{p(N), p(N+1), \psi(N), \psi(N+1)\Big\} = J^0_p(M) + \Bigg[\delta p(N)\frac{\delta J^0_p(M)}{\delta p(N)} + \delta p(N+1)\frac{\delta J^0_p(M)}{\delta p(N+1)} + \delta\psi(N)\frac{\delta J^0_p(M)}{\delta\psi(N)} + \delta\psi(N+1)\frac{\delta J^0_p(M)}{\delta\psi(N+1)}\Bigg]. \tag{4.14}$$

The resulting set of linear simultaneous equations can be expressed as a tri-diagonal matrix equation:

$$\begin{aligned} A(N)\delta y(N-1) + B(N)\delta y(N) + C(N)\delta y(N+1) &= F(N) \\ \text{for} \quad 2 \leq N \leq MAX-1 & \end{aligned} \tag{4.15}$$

where;

$$\delta y(N) = \begin{pmatrix} \delta p \\ \delta n \\ \delta \psi \end{pmatrix} \quad \text{and} \quad \delta y(1) = \delta y(MAX) = 0.$$

$A(N)$, $B(N)$ and $C(N)$ are 3×3 matrices, $F(N)$ is a 1×3 vector. N represents the current position along the grid and MAX the final gridpoint. The matrix equation is shown in full in appendix A.

4.2.8 Solving the Matrix Equation

Solution of the matrix equation is complicated by its large size. An efficient algorithm is required to ensure that processing time is minimised. A method suggested in [79] is used. This technique involves expressing the matrix equation in terms of only two grid-points:

$$B'(N)\delta y(N) + C'(N)\delta y(N+1) = F'(N). \tag{4.16}$$

Thus a reduced set of unknown primed matrices are introduced. A set of recursive relations can be formed by equating (4.16) to (4.15), re-arranging to give:

$$\delta y(N) = B'(N)^{-1}F'(N) - B'(N-1)^{-1}C'(N)\delta y(N+1). \tag{4.17}$$

and comparing the resulting equation with (4.16):

$$B'(N) = B(N) - A(N)B'(N-1)^{-1}C'(N-1) \quad (4.18)$$
$$C'(N) = C(N) \quad (4.19)$$
$$F'(N) = F(N) - A(N)B'(N-1)^{-1}F'(N-1) \quad (4.20)$$
$$\text{for} \quad 3 \leq N \leq MAX - 1.$$

Using the fact that the endpoints are known via the boundary conditions i.e.

$$\delta y(1) = \delta y(MAX) = 0$$

and comparing equations (4.15) and (4.16), uncovers the value of the primed matrices for $N = 2$:

$$B'(2) = B(2) \quad , \quad C'(2) = C(2) \quad , \quad F'(2) = F(2)$$

The recursive relations can now be used to calculate the values of the primed matrices at each consecutive grid-point. Once the primed matrices are known for each grid-point the value of the incremental matrix ,δy, can be calculated using equation (4.17) by working back along the grid and again noting that $\delta y(MAX) = 0$.

Once the values of the vector δy are known for all gridpoints, the fundamental variables at each gridpoint can be amended according to (4.13). Thus the solution of the equations is improved. The non-linear nature of the semiconductor equations requires that the process be iterated until the solution reaches an acceptable level. The ultimate accuracy of the final solution is controlled by the order of the difference approximation and the grid spacing. As shown in section 4.2.4, for a first order approximation the accuracy that is attainable is typically of the order of the grid spacing itself. To decide when the required level of accuracy has been reached a convergence test is applied. This will be discussed in the next section.

4.2.9 Initialising and Terminating the process

The iterative technique described up to this point includes no facility for starting or ending the process. In order to evaluate each cell in the matrix for the first time, to initiate the solution process, it is first necessary to have a set of trial values for n, p and ψ. In addition, to terminate the process it is necessary to know when the solution has reached the required level of accuracy. This is achieved by applying a convergence test.

Initialisation

To speed the solution process a trial solution that is close to the final solution is required. Of course, if a trial solution was known for all of the simulated external influences i.e. bias, illumination and irradiation, then the simulation would have little value. Thus a simple analytical trial solution is provided for the case with no external influence. Space charge neutrality is assumed and hence the carrier densities are given by:

$$p = \begin{cases} -\Gamma & \text{P region} \\ \frac{n_i^2}{\Gamma} & \text{N region} \end{cases} \tag{4.21}$$

$$n = \begin{cases} \Gamma & \text{N region} \\ -\frac{n_i^2}{\Gamma} & \text{P region.} \end{cases} \tag{4.22}$$

The potential is set to be:

$$\psi = \begin{cases} \frac{1}{\theta}\ln\left(-\frac{n_i}{\Gamma}\right) & \text{P region} \\ \frac{1}{\theta}\ln\left(\frac{\Gamma}{n_i}\right) & \text{N region.} \end{cases} \tag{4.23}$$

It is assumed that the device has ideal ohmic contacts i.e. they are in thermal equilibrium hence any excess charge immediately vanishes and no space charge exists. Once a final solution is found, external influences can be gradually introduced. The trial solution for the new case is then constructed from the previous final solution.

Modifying the Conditions

For a change in applied bias the new trial solution includes the carrier concentrations, n and p, from the final solution at the previous bias. No alteration is made to the carrier concentration. Thus it is necessary to *step up* in small increments of bias. This ensures that the carrier concentration is not significantly altered by the change in bias. Typically steps of 1V are used.

The electrostatic potential, $\psi(N)$, from the solution at the previous bias is slightly altered to provide a new trial electrostatic potential, $\psi_T(N)$ at each gridpoint. This ensures that the boundary conditions are satisfied. A simple proportional relation is used to modify the value of $\psi(N)$.

$$\psi_T = \left[1 - \frac{V_c - V_p}{\psi(1) - \psi(L)}\right]\psi(N) + \frac{V_c - V_p}{\psi(1) - \psi(L)}\psi(L) \tag{4.24}$$

where V_p and V_c are the previous and current bias, ψ is the electrostatic potential from the previous solution at the boundaries;$(1), (L)$ and at gridpoint (N).

When simulating neutron irradiation, the complete un-altered solution from the previous fluence is used as a trial solution. Thus for the first *irradiation* the unirradiated solution is used as a starting point. This method works very efficiently and steps of $1 \times 10^{13}\mathrm{ncm}^{-2}$ are possible.

The software is designed to produce data over a pre-set range of bias and neutron irradiation fluence, for a particular device, with the minimum of user interaction. This is necessary as the simulation can run for several days. The efficient storage and retrieval of 'old' solutions is clearly essential as these form part of later solutions.

To facilitate efficient storage a well defined scheme is required. Figure 4.5 shows how the solution procedure is organised. The initial analytical trial solution is provided at point A, i.e. with no bias or irradiation. The final solution, at point A.is then used to generate a trial solution for the next increment in bias. This continues for the complete bias range, as shown by point B. At this point the *irradiation* of the device begins. The solution procedure jumps back to the first bias selected by the user for irradiation, In this case point C. Once a solution is found the neutron fluence is then incremented. The solution at the previous increment is then supplied as a complete trial solution for the new neutron fluence level. This process continues until the level of irradiation specified by the user is reached, point D. The procedure then repeats for the complete range of bias values selected by the user, points E ... If at any point an acceptable solution is not found a warning message is generated specifying the bias and fluence level for which this occurred.

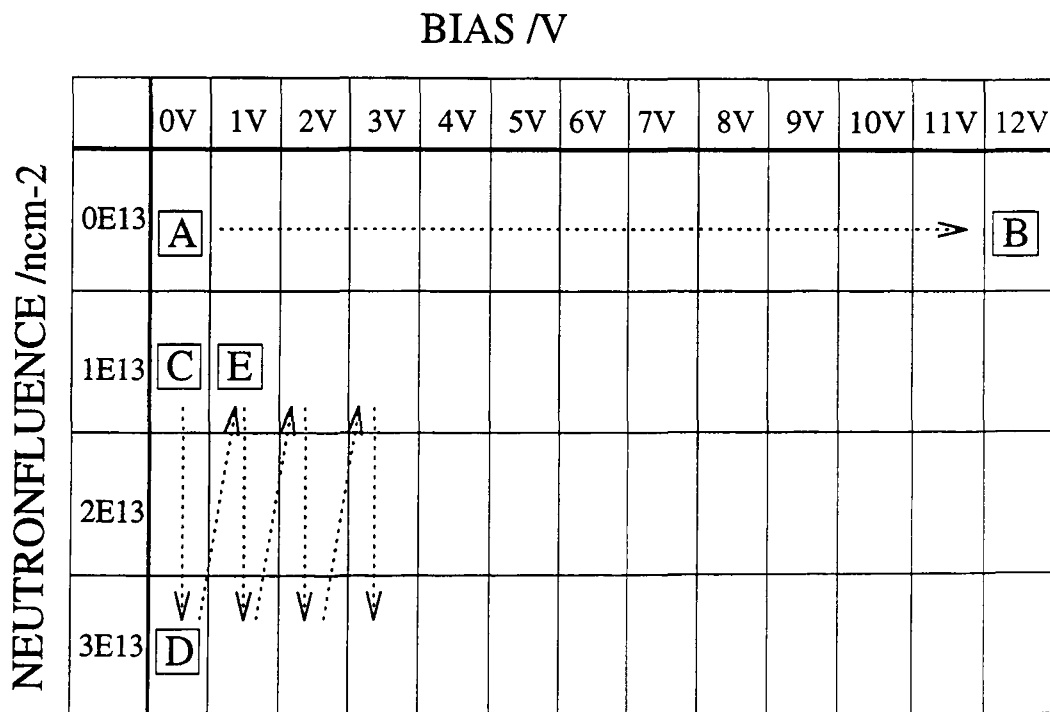

Figure 4.5: A diagram showing how the solution procedure is organised to allow efficient retrieval of previous solutions for use in new trial solutions.

The illumination of devices is performed throughout the whole process just outlined. Thus when a device is illuminated, the illumination is actually present for

the first scenario with no bias or neutron irradiation. The analytical trial solution given by equations (4.21), (4.22) and (4.23), is also used with illumination. Thus to characterise a device for several wavelengths over a range of bias and irradiation conditions, a set of processes is required. One un-illuminated process provides the dark current at each bias and neutron fluence and the illuminated processses are used to provide the photocurrents at selectable wavelengths. In this way the spectral response of the device can be evaluated for any combination of bias and/or neutron fluence.

Termination

A convergence test is used to determine when the solution has reached the required level of accuracy. The absolute error in the solution cannot be determined explicitly because the true solution is unknown. Thus a new parameter, the residual, is used as a measure of the relative error at each gridpoint. The residual is defined as the ratio between the calculated increment, i.e. δp, used to modify the value of the fundamental variable and the value of the fundamental variable itself i.e. p. Defining the residual such that the relative error is used allows a single threshold to be applied equally to each variable at each gridpoint. Once the required threshold is reached at each gridpoint the iteration is terminated. Typically a value of $5\text{x}10^{-9}$ is used as this is typically the minimum that can be achieved for the first few solutions.

4.2.10 Impact Ionisation

Impact ionisation is the fundamental process that underlies the operation of avalanche photodiodes, thus inclusion of the process is essential. A generation term that describes impact ionisation is incorporated into the continuity equations (4.1),(4.2):

$$G(N) = \frac{1}{q}(\alpha_e(N)J_n(N) + \alpha_h(N)J_p(N)) \tag{4.25}$$

The electron and hole ionisation rates in silicon, α_e and α_h, are calculated using a modified [82] form of the Baraff three parameter theory [83], equation (4.26).

$$\alpha_{e/h} = \frac{1}{\lambda_{p/n}} \exp\left(\frac{A\varepsilon_i^2}{q^2 E^2 \lambda_{p/n}^2} + \frac{B\varepsilon_i}{qE\lambda_{p/n}} + C \right) \quad (4.26)$$

$$\begin{aligned} A &= 11.5r^2 - 1.17r + 3.9 \times 10^{-4} \\ B &= 46r^2 - 11.9r + 1.75 \times 10^{-2} \\ C &= -757r^2 + 75.5r - 1.92 \end{aligned} \quad (4.27)$$

$$r = \frac{\langle \varepsilon_r \rangle}{\varepsilon_i} \quad (4.28)$$

Following Ref.[84] , ε_i, the activation energy, is taken to be $\frac{3E_G}{2}$ where E_G is the bandgap energy, $\langle \varepsilon_r \rangle$ is the mean energy loss per optical phonon collision. $\lambda_{p/n}$ is the optical phonon mean free path for either holes or electrons. Following Ref. [9] , the variation of ionisation rate with temperature was accounted for via the expressions

$$\langle \varepsilon_r \rangle = \varepsilon_r \tanh\left(\frac{\varepsilon_r}{2kT} \right) \quad (4.29)$$

$$\lambda = \lambda_0 \tanh\left(\frac{\lambda_0}{2kT} \right) \quad (4.30)$$

where λ_0 is taken to be 55Å for holes and 76Å for electrons and $\varepsilon_r = 0.063eV$.

The modified Baraff three parameter theory was sucessfully used to model temperature effects in EG&G silicon APD's [93]. Sutherland developed a more accurate empirical fit to the Baraff curves [92]. This provides a good fit to the Baraff curves over a wider range of parameter values than the Crowell-Sze approximation [82]. The disadvantage of the Sutherland method is that the resulting parameterisation has a cubic form. Incorporating this technique into the model would increase the complexity dramatically, hence reducing the computational efficiency. At 300K and up to electric fields of around 350kVcm^{-1}, approximately the maximum reached

by the models, the less complex Crowell-Sze approximation performs well. The improvement offered by the Sutherland model, over the Crowell-Sze method, occurs predominantly at higher electric fields than found in the models developed, and would incur a large computational penalty. Hence the use of the Crowell-Sze approximation is preferable due to its relative simplicity.

The generation term is evaluated at the main grid point and hence the current density and electric field, which are evaluated at the half-points, have to be transformed to main grid points also. To increase the accuracy of the generation term, this is achieved by assuming a linear change in their values between the half-points and therefore the value at the main grid-point is taken to be the mean of the two half-point values weighted to the distance between the half-points and the main-points, figure 4.6. The weighting is necessary for regions of non-uniform grid-spacing. The electric field and hole current density at the main-points are written explicitly in equations (4.31) and (4.32).

$$E(N) = \frac{1}{h'(N)}\Big[\frac{h(M)}{2}\frac{1}{h(M-1)}[\psi(N) - \psi(N-1)] + \frac{h(M-1)}{2}\frac{1}{h(M)}[\psi(N+1) - \psi(N)]\Big] \quad (4.31)$$

$$\begin{aligned} J_p(N) = {} & \frac{h(M)}{2h'(N)}\frac{q}{h(M-1)}\Big[\mu_p(M-1)\frac{\psi(N-1)-\psi(N)}{1-e^{-\theta[\psi(N-1)-\psi(N)]}}p(N-1) + \\ & \mu_p(M-1)\frac{\psi(N-1)-\psi(N)}{1-e^{\theta[\psi(N-1)-\psi(N)]}}p(N)\Big] + \\ & \frac{h(M-1)}{2h'(N)}\frac{q}{h(M)}\Big[\mu_p(M)\frac{\psi(N)-\psi(N+1)}{1-e^{-\theta[\psi(N)-\psi(N)]}}p(N) + \\ & \mu_p(M)\frac{\psi(N)-\psi(N+1)}{1-e^{\theta[\psi(N)-\psi(N+1)]}}p(N+1)\Big] \end{aligned} \quad (4.32)$$

Equation (4.33) shows the generation term in its explicit form.

$$
\begin{aligned}
G(N) = \frac{1}{q}\Bigg[\frac{1}{\lambda_n}\exp\Bigg\{ \\
&\left(\frac{A\varepsilon_i^2}{e^2\left(\frac{1}{h'(N)}\left[\frac{h(M)}{2}\frac{1}{h(M-1)}[\psi(N)-\psi(N-1)]+\frac{h(M-1)}{2}\frac{1}{h(M)}[\psi(N+1)-\psi(N)]\right]\right)^2\lambda_n^2}\right) \\
&+\left(\frac{B\varepsilon_i}{e\left(\frac{1}{h'(N)}\left[\frac{h(M)}{2}\frac{1}{h(M-1)}[\psi(N)-\psi(N-1)]+\frac{h(M-1)}{2}\frac{1}{h(M)}[\psi(N+1)-\psi(N)]\right]\right)\lambda_n}\right) \\
&-C\Bigg\}\times\Bigg\{\frac{h(M)}{2h'(N)}\frac{q}{h(M-1)}\left[\mu_n(M-1)\frac{\psi(N-1)-\psi(N)}{1-e^{\theta[\psi(N-1)-\psi(N)]}}n(N-1)+\right. \\
&\left.\mu_n(M-1)\frac{\psi(N-1)-\psi(N)}{1-e^{-\theta[\psi(N-1)-\psi(N)]}}n(N)\right]+ \\
&\frac{h(M-1)}{2h'(N)}\frac{q}{h(M)}\left[\mu_n(M)\frac{\psi(N)-\psi(N+1)}{1-e^{\theta[\psi(N)-\psi(N)]}}n(N)+\right. \\
&\left.\mu_n(M)\frac{\psi(N)-\psi(N+1)}{1-e^{-\theta[\psi(N)-\psi(N+1)]}}n(N+1)\right]\Bigg\}+\frac{1}{\lambda_p}\exp\Bigg\{ \\
&\left(\frac{A\varepsilon_i^2}{e^2\left(\frac{1}{h'(N)}\left[\frac{h(M)}{2}\frac{1}{h(M-1)}[\psi(N)-\psi(N-1)]+\frac{h(M-1)}{2}\frac{1}{h(M)}[\psi(N+1)-\psi(N)]\right]\right)^2\lambda_p^2}\right) \\
&+\left(\frac{B\varepsilon_i}{e\left(\frac{1}{h'(N)}\left[\frac{h(M)}{2}\frac{1}{h(M-1)}[\psi(N)-\psi(N-1)]+\frac{h(M-1)}{2}\frac{1}{h(M)}[\psi(N+1)-\psi(N)]\right]\right)\lambda_p}\right) \\
&-C\Bigg\}\times\Bigg\{\frac{h(M)}{2h'(N)}\frac{q}{h(M-1)}\left[\mu_p(M-1)\frac{\psi(N-1)-\psi(N)}{1-e^{-\theta[\psi(N-1)-\psi(N)]}}p(N-1)+\right. \\
&\left.\mu_p(M-1)\frac{\psi(N-1)-\psi(N)}{1-e^{\theta[\psi(N-1)-\psi(N)]}}p(N)\right]+ \\
&\frac{h(M-1)}{2h'(N)}\frac{q}{h(M)}\left[\mu_p(M)\frac{\psi(N)-\psi(N+1)}{1-e^{-\theta[\psi(N)-\psi(N)]}}p(N)+\right. \\
&\left.\mu_p(M)\frac{\psi(N)-\psi(N+1)}{1-e^{\theta[\psi(N)-\psi(N+1)]}}p(N+1)\right]\Bigg\}\Bigg] \qquad (4.33)
\end{aligned}
$$

4.2.11 Illumination

A change in incident wavelength can have several independent simultaneous effects on a device's operation. The net effect can appear extremely complex over a range

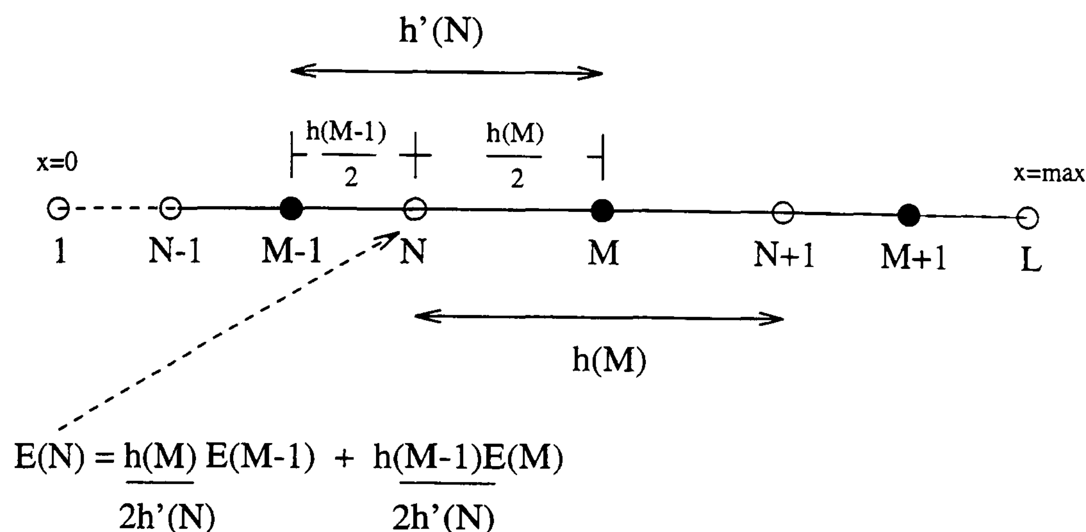

Figure 4.6: A figure showing the method used to transform the electric field from the half-points to the main grid points.

of wavelength and bias. To simulate accurately the spectral response of a device, in particular an APD, it is necessary to include illumination directly into the model. Thus the simulation automatically superimposes the different effects that can occur. In this way the simulated diode can be *illuminated* and tested using a process that relates directly to experimental method.

Monochromatic illumination is included via a generation term in the continuity equations. Normal incidence is considered at all times.

$$G(N) = e^{-\beta x(N)} - e^{-\beta x(N+1)} \tag{4.34}$$

Equation (4.34) shows the form of the generation term used. Here β represents the optical absorption co-efficient in silicon. The signal charge generated at each grid point represents the integrated charge generated over the whole inter-grid point spacing. The variation in optical absorption co-efficient with wavelength in silicon,(4.35), is described using data from [85].

$$\beta(\lambda) = 6 \times 10^5 \times \exp^{-8.5\times10^{-3}\times\lambda} \tag{4.35}$$

During the simulation one job is left to run without illumination, producing dark current data and several *illuminated* jobs are run to produce data at each wavelength. The data produced in this way are identical in form to the data collected experimentally. This simplifies the evaluation of the data as the same manipulation is applied to both data sets.

4.2.12 Neutron Radiation Damage

The main motivation behind the development of the simulation was to investigate the effects of neutron radiation damage in avalanche photodiodes. Neutron radiation damage was incorporated into the model via the introduction of deep acceptor levels and a suitable change in the minority carrier lifetime. This method was sucessfully used to model the change in N_{eff} with neutron fluence in silicon microstrip detectors [86].

The deep acceptor levels are included via a term in the Poisson equation (4.3). The total number of filled acceptors at grid point N , $\sum N_A(N)$, is given by the product of the total number of available levels, $N_A(N)$ and the occupancy function, $f(E_T, N)$, equation (4.36).

$$\sum N_A(N) = f(E_T, N) \times N_A(N) \tag{4.36}$$

A Shockley-Read-Hall occupancy function is used to fill the deep levels. The fraction of filled acceptors, at energy E_T and gridpoint N, is given by equation (4.37).

$$f(E_T, N) = \frac{n(N) + \frac{\sigma_p}{\sigma_n} n_i \exp\left(\frac{E_i - E_T}{kT}\right)}{n(N) + \frac{\sigma_p}{\sigma_n} p(N) + n_i \exp\left(\frac{E_T - E_i}{kT}\right) + \frac{\sigma_p}{\sigma_n} n_i \exp\left(\frac{E_i - E_T}{kT}\right)} \tag{4.37}$$

Initially quasi-Fermi statistics were used to describe the occupancy of the deep levels; this equates to substituting $\sigma_p = 0$ in equation (4.37). The use of quasi-Fermi statistics resulted in severe convergence problems. This was thought to be due to the

lack of consideration of electron emission, via σ_p, causing the occupancy function to saturate when the deep donor implant in the reverse structure was partly depleted.

The most likely candidate for the deep acceptor level is the V_2O complex [87], [88] which is situated 0.5eV below the conduction band (see chapter 3). The deep acceptor level used in the simulation is based on the V_2O, although any species of acceptor or donor level can be modelled. A maximum of one acceptor and one donor level is possible. The V_2O introduction rate , for 1 MeV neutrons, has been calculated from a defect kinetics model to be 0.96cm^{-1} at 20°C [88]. A summary of the properties of the deep level used in the simulation are provided in table 4.3

Property	Value
Name	V_2O
Type	Acceptor
Charge Un-occupied	neutral
Charge Ionised	negative (-1)
Position	$E_C - 0.5$eV
Introduction Rate	$0.96cm^{-1}$at$20°C$
$\frac{\sigma_p}{\sigma_n}$	1

Table 4.3: Table showing the properties of the deep acceptor level used in the simulation.

The variation in minority carrier lifetime, τ, with neutron fluence, Φ_n in silicon under equilibrium conditions, is described in terms of the lifetime damage-constant,K_τ [89]:

$$\frac{1}{\tau} = \frac{1}{\tau_0} + \frac{\Phi_n}{K_\tau}. \tag{4.38}$$

For high fluences this can be written as:

$$\frac{1}{\tau} \approx \frac{\Phi_n}{K_\tau}. \tag{4.39}$$

The minority carrier lifetime in the simulation is varied according to (4.39) and it is assumed that the effective carrier lifetime in the depletion region is subject to

the same relation. The value of K_τ is calculated for high resistivity-silicon [89] to be approximately $K_\tau = 10^7 \mathrm{scm}^{-2}$. With K_τ set to this value the rate of change of N_{eff} with fluence is kept consistent with predictions [87], [89] by setting the ratio of the hole and electron capture cross-sections to unity [87]. The introduction of the deep acceptor levels is assumed to be linear with neutron fluence.

The effects of annealing, although extremely important in the overall understanding of device performance under irradiation, have not been included in the model. This would be a very worthwhile extension to the model but there exist only limited data on the annealing of the concentration of individual defect species, in particular the V_2O. This information would be needed to modify the defect concentration with time. It would also be necessary to calculate how the minority carrier lifetime should be modified with annealing.

4.3 APDGAIN

4.3.1 Introduction

The multiplication factor is defined as the multiplying power of the gain region. For example if an electron is injected into a gain region with a multiplication factor of $M_e = 10$, then 10 electrons will emerge. Similarly we can define a hole multiplication factor M_h. If an electron is generated inside the gain region it will experience less multiplication, i.e. $M_e < 10$.

The current gain calculated from APDSIM includes effects such as absorption of signal charge in the gain region. Thus inferring the multiplication factor from the data can be difficult. To evaluate the multiplication factor directly an analysis is performed on the electric field profile provided by APDSIM. This allows the multiplication factor of the gain region to be computed and compared with the current gain evaluated directly from APDSIM. A simple extension of this process also allows the excess noise factor of the device to be evaluated.

4.3.2 Multiplication Factor

To calculate the multiplication factor equation (4.41) is evaluated across the gain region, this follows from the equation 2.41. Only the electron multiplication factor is calculated as most silicon devices are primarily designed to multiply the electron signal (see section 2.3.6). The multiplication factor is defined as

$$M_e = \frac{1}{1 - I} \tag{4.40}$$

Where

$$I = \int_0^w \alpha_e \exp^{-\int_0^x (\alpha_e - \alpha_h) dx'} dx \tag{4.41}$$

To determine the bounds of the gain region, the ionisation co-efficients are evaluated across the whole device using a simple Chenowyth approximation (see section 2.3.5). The boundaries of the gain region are then defined as the points at which the electron ionisation rate, α_e, becomes greater than unity.

Once the gain region has been specified, the number of grid points describing the electric field in the gain region is dramatically increased. Typically 50 grid points are introduced between the existing grid points. This is achieved by assuming a linear change in the electric field between the grid points and simply assigning the value of the new points accordingly.

Equation (4.41) is now computed across the *magnified* region. The integrals are evaluated using the trapezoid rule. To remain consistent with APDSIM during the calculation the ionisation co-efficients are expressed via the modified Baraff three parameter theory [83] . When the calculation is complete the *magnification* process is repeated, with another 5 grid points being inserted. Equation (4.41) is evaluated again and this process repeated until the change in the result falls below a pre-determined level, typically 1×10^{-3}. This corresponds approximately to an error of 1% on a gain of 10 and 10% on a gain of 100.

4.3.3 Excess Noise Factor

Discussion of APD properties is incomplete unless some mention of the excess noise factor is included. The discussion in chapter 2 explains that the excess noise factor is inherent in a device such as an APD, with a statistical gain mechanism. To this end a simple analysis of the excess noise factor was incorporated into the model [33].

$$F_e = K_{eff}M_e + (2 - \frac{1}{M_e})(1 - K_{eff}) \tag{4.42}$$

The excess noise factor is calculated using equation (4.42). The equation is similar to the form introduced in chapter 2 but the variation of the ratio of the ionisation co-efficients, k, with the electric field is accounted for in the term $\mathrm{K_{eff}}$. The definition of $\mathrm{K_{eff}}$ is given in equation (4.43), where the terms $\mathrm{k_1}$ and $\mathrm{k_2}$ are defined in equations (4.44) and (4.45) respectively. The electron excess noise factor is calculated for the same reasons outlined in section 4.3.2.

$$\mathrm{K_{eff}} = \frac{\mathrm{k_2} - \mathrm{k_1^2}}{1 - \mathrm{k_2}} \tag{4.43}$$

$$\mathrm{k_1} = \frac{\int_0^w \alpha_h M(x)\mathrm{d}x}{\int_0^w \alpha_e M(x)\mathrm{d}x} \tag{4.44}$$

$$\mathrm{k_2} = \frac{\int_0^w \alpha_h M(x)^2\mathrm{d}x}{\int_0^w \alpha_e M(x)^2\mathrm{d}x} \tag{4.45}$$

The calculation of the excess noise factor is incorporated into the calculation of the multiplication factor. This is possible because they are both calculated from the same common components. The magnification discussed in section 4.3.2 is also applied to the calculation of the excess noise factor. The process is terminated using the same conditions outlined in section 4.3.2.

4.4 DIFFUSE

4.4.1 Introduction

The final piece of software, DIFFUSE, is used to create the one-dimensional doping profiles of the devices under investigation. The aim of the software is to allow a user to specify the peak concentration and depth of the specific implants and to generate a structure accordingly.

The implants were created using a simple *drive in* diffusion process. This process consists of diffusing a fixed amount of dopant into the substrate and is a reasonable approximation of the method used to create the EG&G devices under investigation. The dopants used are phosphorus for the n-type implants and boron for the p-type implants. Phosphorus and boron are typical dopants used in silicon due to their high solubility, typically above $5 \times 10^{20} cm^{-3}$ [90]. It is assumed for simplicity that the diffusion co-efficient of phosphorus and boron are unchanged even when diffusing through already heavily doped regions.

The diffusion process is described by Fick's diffusion equation (4.46).

$$\frac{\delta C}{\delta t} = D\frac{\delta^2 C}{\delta x^2} \tag{4.46}$$

The solution of the equation satisfying the boundary conditions for drive in diffusion equations (4.47) and (4.48), is given by equation (4.49).

$$\int_0^\infty C(x,t)dx = 1 \tag{4.47}$$

$$C(\infty,t)dx = 0 \tag{4.48}$$

$$C(x,t) = \frac{S}{\sqrt{\pi Dt}}\exp\left[-\frac{x^2}{4Dt}\right] \tag{4.49}$$

Once the user's parameters are set, the program steps up in time calculating the concentration profile of each of the implants, until each implant reaches the required specifications. Once an individual implant is deemed satisfactory, its diffusion is stopped and the remaining implants allowed to continue. When the last implant is successfully diffused the process is terminated and the doping profile is saved to a file. The diffusion co-efficients used in DIFFUSE are $3.0 \times 10^{-12} cm^2 s^{-1}$ for phosphorus and $4.5 \times 10^{-12} cm^2 s^{-1}$ for boron after Ref [91].

4.5 Simulation Limitations

4.5.1 Introduction

A detailed summary of each of the three pieces of software used in the simulation has been presented. Once supplied with an effective doping profile the suite of software can be considered a model. To complete the summary a list of the key assumptions/limitations are listed.

4.5.2 APDSIM

- A one dimensional form is useful for investigating the bulk properties of a device i.e. dark current or effects due to variation of light absorption in the device. The significant limitation of a one-dimensional model is that surface effects and non-linearities along the lateral direction, which may result in impact ionisation occurring outside the defined gain region, have to be ignored. In a real device these play a significant part of the operation.

- The Crowell-Sze parameterisation of the universal Baraff curves that is used to calculate the ionisation rates in silicon has been shown to be inaccurate in some circumstances. Sutherland [92] discussed this problem and generated a cubic parameterisation that gave better coverage of the Baraff curves over a wider range of temperature and electric field strength. The data presented in this model are at 300K and the field strengths do not rise far above $350 kV cm^{-1}$. In this domain the

relatively simple Crowell-Sze approximation performs well. The implementation of the Sutherland parameterisation would be extemely complex, and the computational time would increase accordingly. Thus the use of the Crowell-Sze approximation is justified here but inclusion of the Sutherland parameterisation would be useful to expand the range of conditions accurately available to the model.

• The effects of self heating in the diode are not included in the model. In avalanche photodiodes this can become a very important effect as the gain can vary significantly with temperature. The inclusion of self heating would be a significant step in the path to creating an extremely versatile model.

• The parameterisation of the mobility, which accounts for the variation of the carrier mobility with carrier concentration, is not dependent on the temperature. This provides a major limitation to investigation of temperature dependent effects. To extract the full potential of the model a more general parameterisation needs to be developed.

• No account is taken of annealing of the radiation damage. The effects of annealing are of equal importance to the initial effects of radiation damage, as most devices are operated in conditions where annealing is present. A worthwhile extension to the model would be to include these effects. In order to do so, more specific information will be required about the change in concentration of individual defect species, e.g. V_2O, during annealing. Also the effect of annealing on the minority carrier lifetime will have to be investigated.

• The introduction of the neutron induced recombination centres is assumed to be linear with neutron fluence. This is a valid assumption as the measured increase in dark current, due to the introduction of recombination centres, is seen to increase linearly with neutron fluence indicating a linear increase in the trap density.

4.5.3 APDGAIN

• The limitations of the Crowell-Sze Baraff parameterisation apply here also. The use of a more sophisticated parameterisation would allow accurate simulation

over a wide range of temperature and with very large electric fields in the gain region.

• The multiplication factor and the excess noise factor are calculated in terms of an injected electron current only. This is valid as most, if not all, silicon devices are designed to multiply only the electron signal in an attempt to reduce the excess noise factor.

4.5.4 DIFFUSE

• The main assumption is that the diffusion of the implants is taken to be independent of the concentration of dopants already present in the substrate. This is an acceptable assumption in silicon as the diffusion is generally not sensitive to the dopant concentration [9].

4.6 Conclusions

A sophisticated simulation package has been introduced and the key components of its operation explained in detail. A full summary of the limitations and assumptions relating to each package has been given. A short description of the process of running the simulation is given in appendix B.

To conclude, the simulation is a very complex attempt at providing a realistic simulation of avalanche photodiode properties both before and after neutron irradiation. There exist several avenues for improvement which will allow the simulation to provide a significantly improved performance.

Chapter 5

Results

5.1 Introduction

The complementary APD designs used for the simulation were introduced in chapter 2. The reach through APD is designed to operate in the range 400-1100nm. The reverse reach through APD is a modified form of the standard reach through APD, optimised for scintillation applications, and operates in the range 400-700nm. The reach through APD has a wide depletion region in front of the gain region. This gives rise to a high quantum efficiency over a wide range of incident wavelengths. Conversely, the reverse reach through structure has a narrow depletion, in which light is collected in front of the gain region. This trades the high quantum efficiency at the longer wavelengths for a reduction in the *nuclear counter effect.*

Implant	S $/cm^{-2}$	t /s	Peak Level $/cm^{-3}$	Depth $/\mu m$
p+	1×10^{13}	5	3×10^{17}	0.12
p	2.4×10^{13}	22386	6×10^{15}	17.5
n+	3.4×10^{14}	511	7×10^{17}	5.0
π	-	-	2.5×10^{12}	-

Table 5.1: Table showing the specifications of each of the diffused implants used to create the reach through model.

The doping profiles used in the simulation are shown in figures 5.1 and 5.2 for the reach through and reverse reach through structures respectively. Light entry is to

Implant	S $/cm^{-2}$	t /s	Peak Level $/cm^{-3}$	Depth $/\mu m$
p+	1×10^{13}	5	3×10^{17}	0.12
p	9.4×10^{13}	4481	5×10^{16}	8.9
n	4.3×10^{13}	50206	8×10^{15}	22.0
n+	1×10^{14}	30	6×10^{17}	1.0
π	–	–	2.5×10^{12}	–

Table 5.2: Table showing the specifications of each of the diffused implants used to create the reverse reach through APD model.

the left for both figures. The generation of the doping profiles is discussed in chapter 4. The parameters used to generate the doping profiles for the reach through and reverse reach through models are given in tables 5.1 and 5.2 respectively.

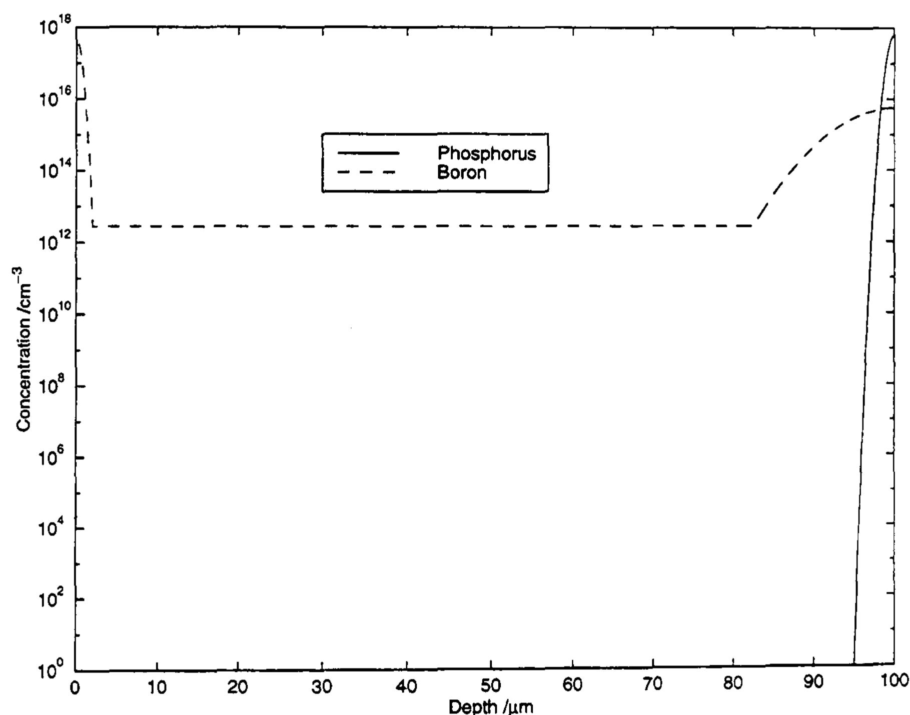

Figure 5.1: Doping profile used to simulate a silicon reach through APD.

The development of both models followed the same path. Initially literature regarding the structure was investigated. Once a working model was created i.e. a model which provided good convergence characteristics over the whole range of bias, illumination and neutron irradiation being investigated, the implants were adjusted until the general performance of the model matched the reported operation. The

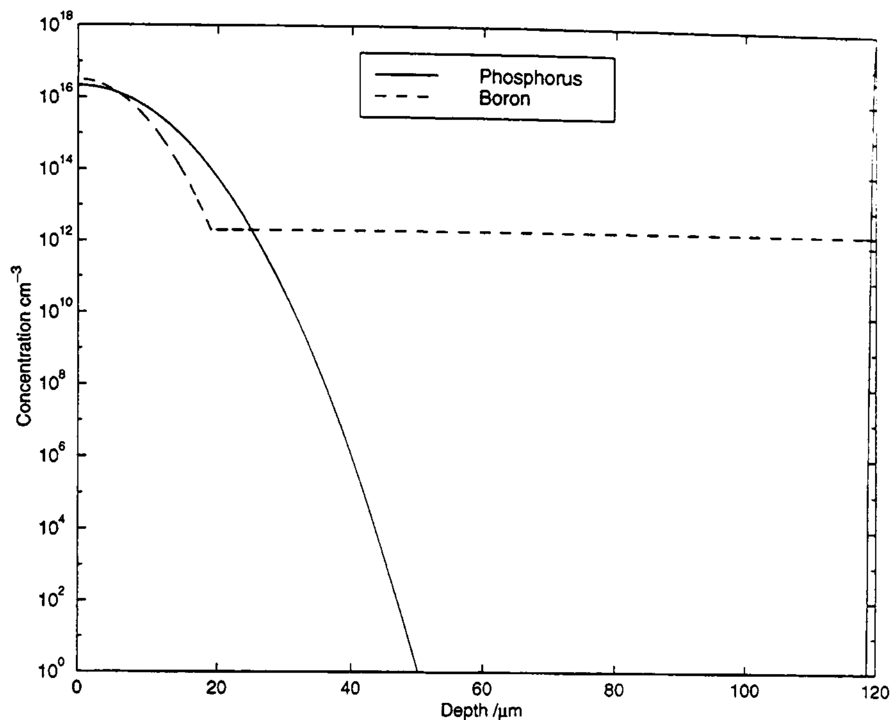

Figure 5.2: Doping profile used to simulate a silicon reverse reach through APD.

latter part of the process proved particularly time consuming. This was not only due to the extreme sensitivity of the device performance to the internal structure but also because modifying a working model often generated one where the solution diverged. Finding a structure that reasonably matched the experimental properties and had good convergence properties proved extremely difficult.

The limited supply of information regarding the structures of the devices significantly reduced the ability of the models to provide quantitative predictions. Thus the aim of the experimental study was limited to providing qualitative comparison with the predictions made by the model.

5.2 Pre-Irradiation

5.2.1 Introduction

The experimental study was performed on two EG&G devices, the C30916E reach through APD and the C30719E reverse reach through APD. The results presented here are divided into two key regions; pre-irradiation and post-irradiation. The aim

of the results is to demonstrate the wide range of information that can be extracted from the models, ranging from detailed microscopic information to the investigation of macroscopic phenomena.

5.2.2 Microscopic Features

The advantage of implementing a full drift-diffusion formulation without making broad assumptions, such as the depletion approximation, is that the device can be investigated throughout the full bias range. The microscopic properties of the devices, i.e. free carrier concentration, potential and electric field, are investigated over a wide range of bias. Figures 5.3 and 5.4 show how the hole and electron concentration vary with applied bias for the reach through structure.

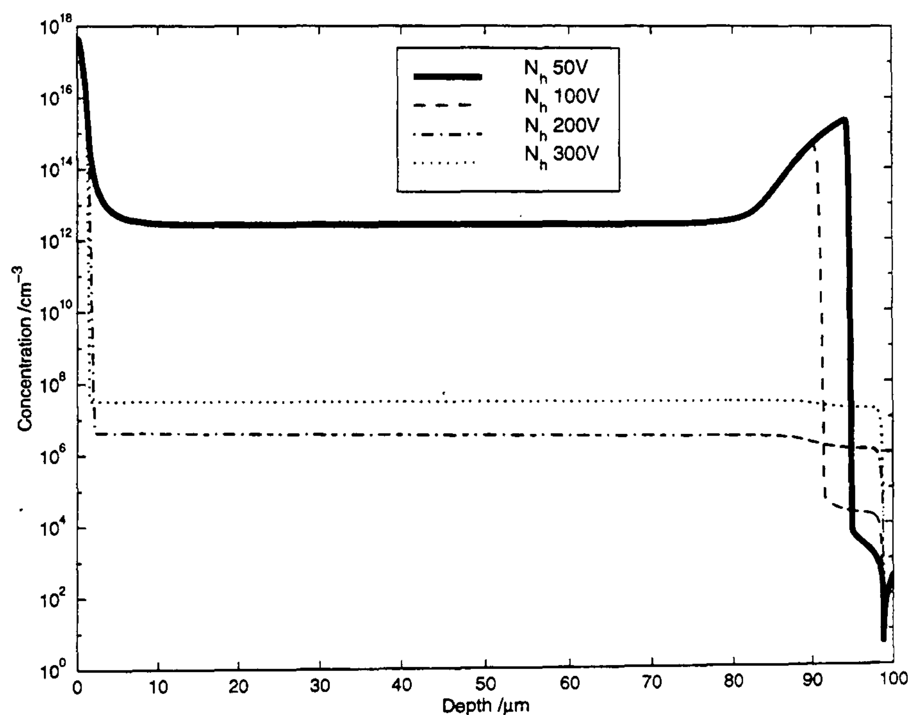

Figure 5.3: Variation in free hole concentration with bias for the reach through model.

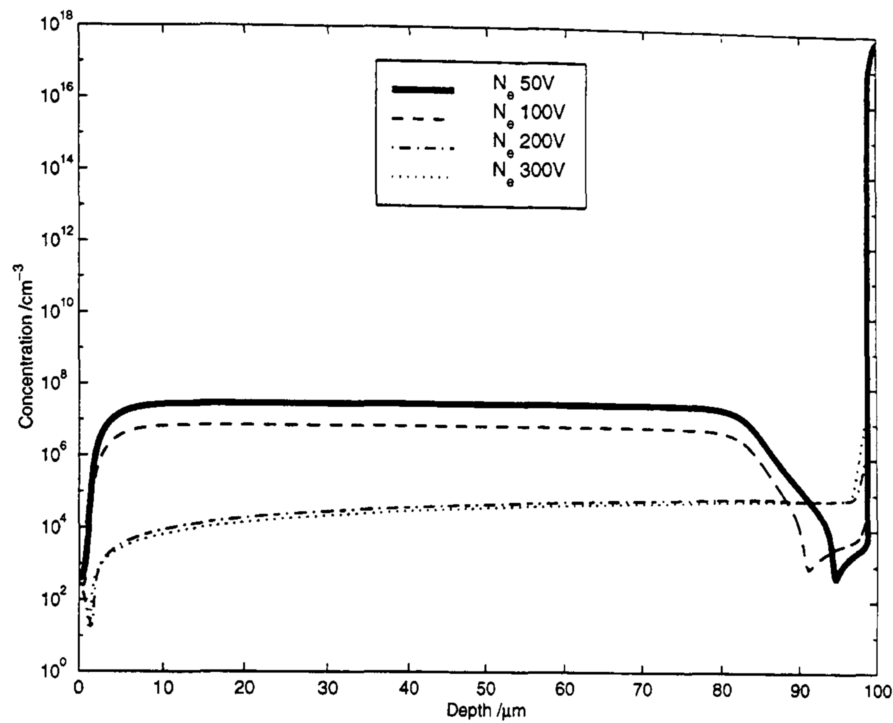

Figure 5.4: Variation in free electron concentration with bias for the reach through model.

Up to 100V the depletion is limited to the highly doped gain region. Once the lightly doped π region is reached, depletion occurs much more rapidly, until the device is fully depleted. Full depletion has occured by 200V. At 300V the gain of the device is large and a large injection of holes from the gain region into the device is visible.

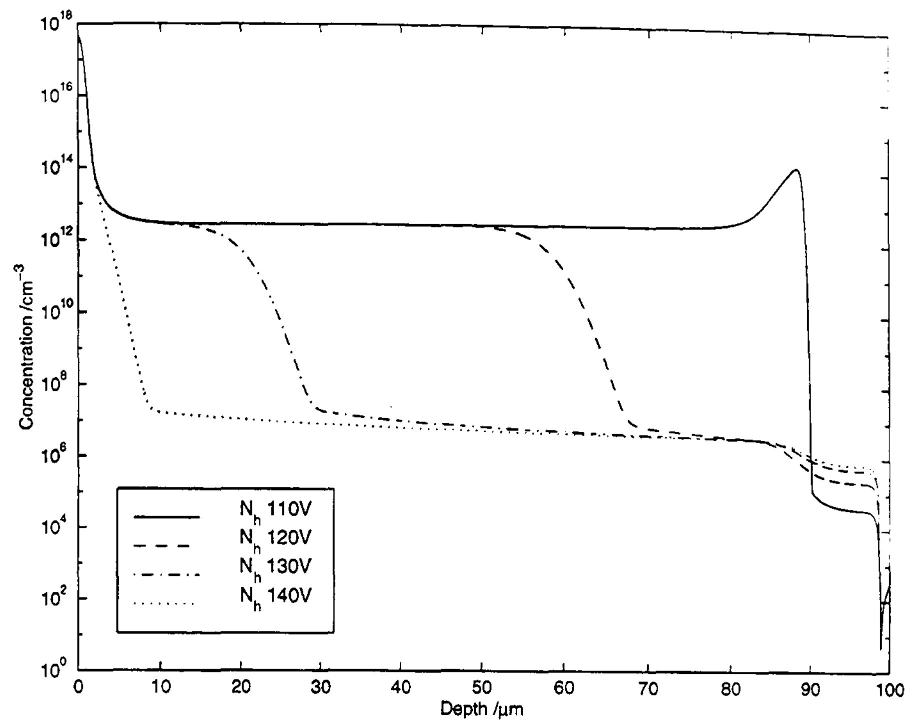

Figure 5.5: Variation in free hole concentration with bias for the reach through model as the device undergoes reach-through.

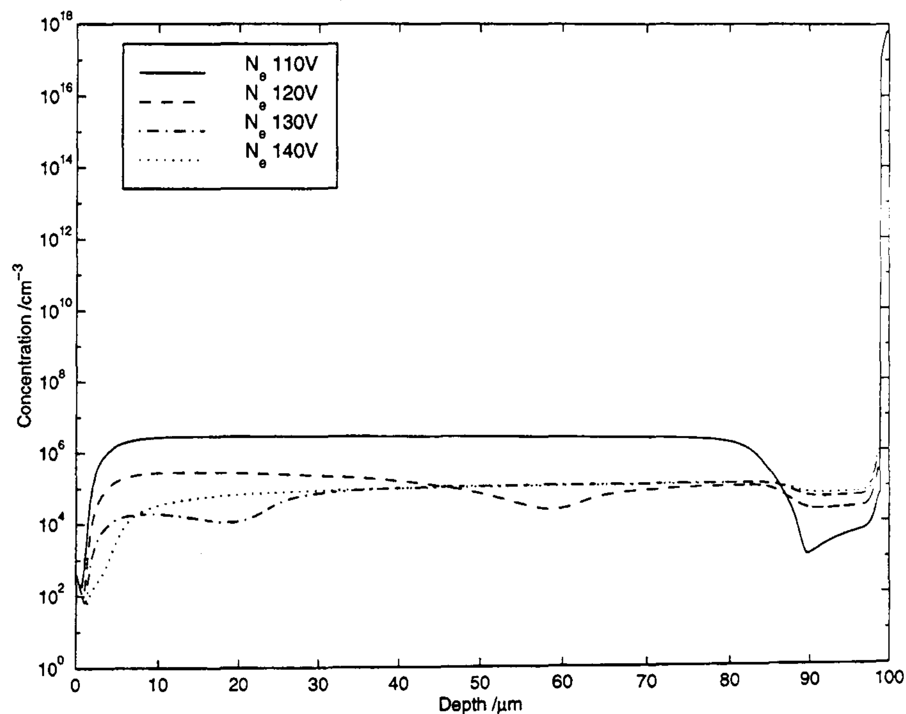

Figure 5.6: Variation in free electron concentration with bias for the reach through model as the device undergoes reach-through.

The transition of the depletion from the highly doped p-region to the lightly

doped π region is known as 'reach-through' and has a significant effect on the macroscopic device properties [94]. Figures 5.5 and 5.6 show the change in the hole and electron concentration as the reach through APD undergoes 'reach-through'. The spread of the depletion region across the device is clearly visible.

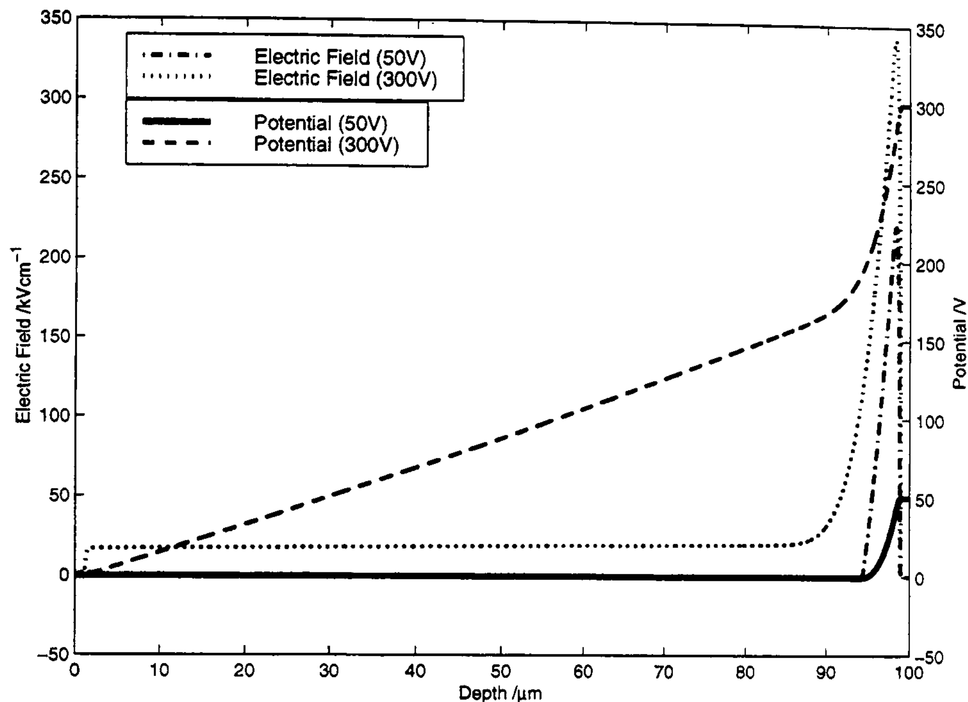

Figure 5.7: Variation in potential and electric field across the reach through model at 50V and 300V.

Figure 5.7 shows the relationship between the potential and the electric field across the device both before and after the device is fully depleted. The peak electric field region, that constitutes the gain region, is clearly visible. Once the device has 'reached through' and is fully depleted a large fraction of the potential drop is across the π region. This reduces the sensitivity of the peak electric field, and hence the gain, to fluctuations in the applied bias.

The free hole and electron concentrations through the reverse reach through APD are shown in figures 5.8 and 5.9. 'Reach-through' occurs at a much higher bias than for the reach through structure. The device is fully depleted at 300V, like the reach through APD the depletion region extends through the majority of the device.

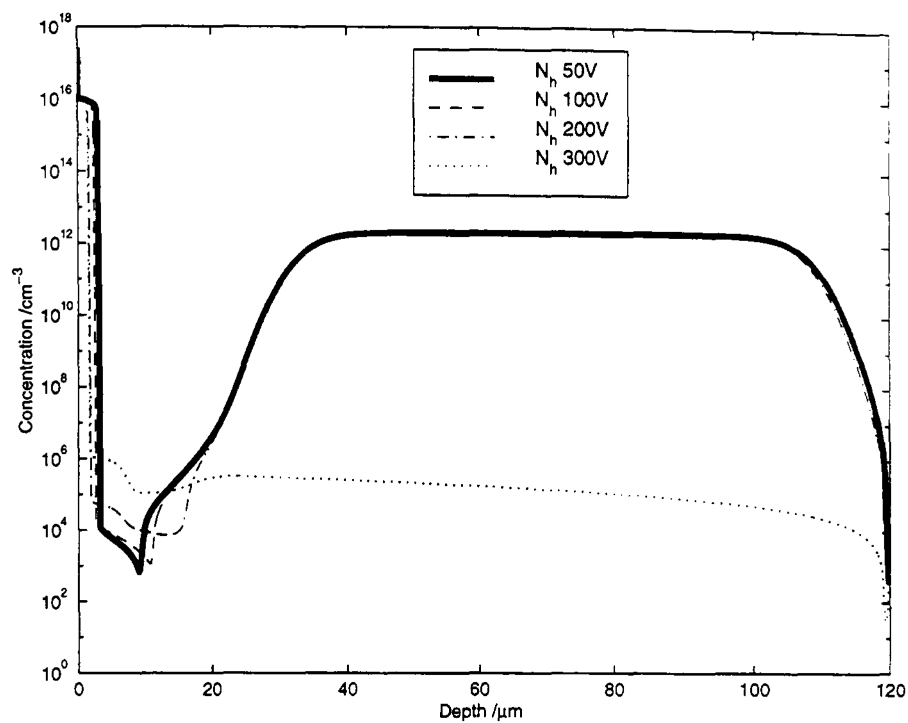

Figure 5.8: Variation in free hole concentration with bias for the reverse reach through model.

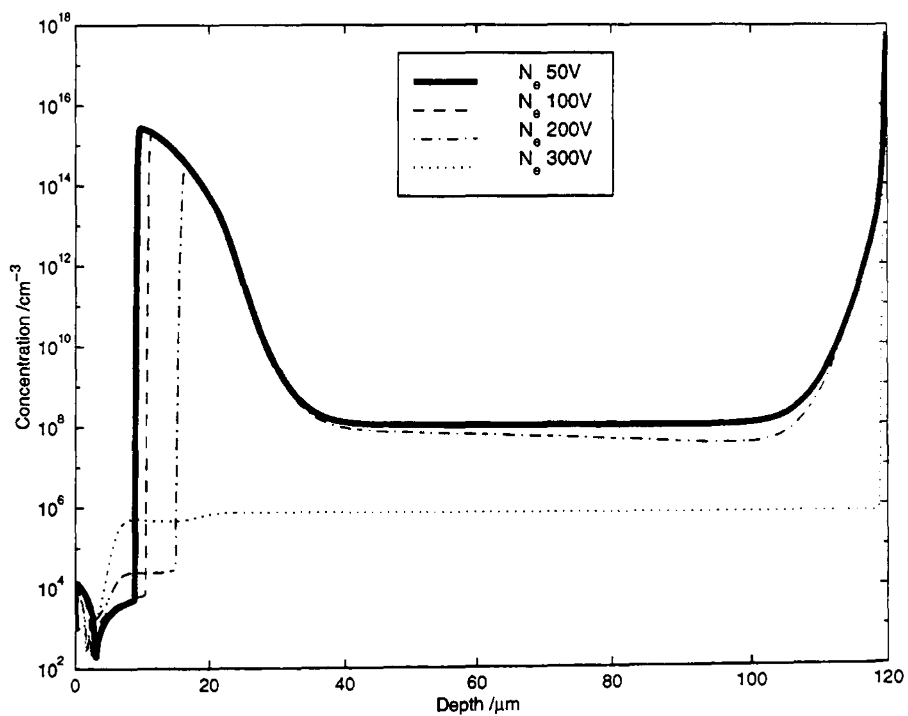

Figure 5.9: Variation in free electron concentration with bias for the reverse reach through model.

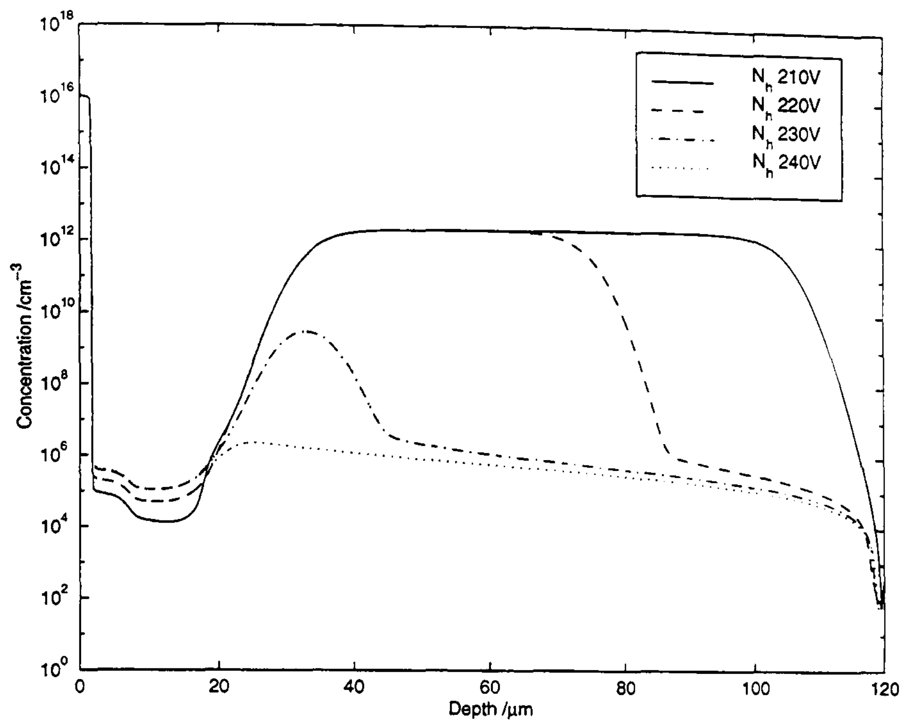

Figure 5.10: Variation in free hole concentration with bias for the reverse reach through structure as the device undergoes reach-through.

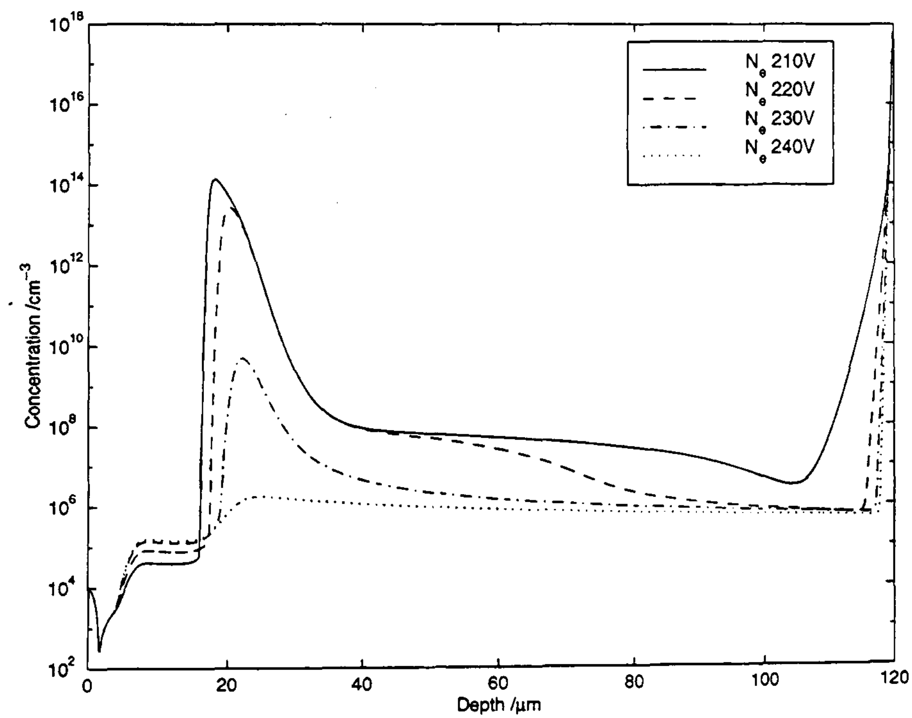

Figure 5.11: Variation in free electron concentration with bias for the reverse reach through model as the device undergoes reach-through.

Figs. 5.10 and 5.11 show how the reverse reach through APD 'reaches though'.

The depletion spreads into the π region from each of the ends. This is unlike the reach through APD, where the depletion extends only from the pn junction at the rear of the device. 'Reach through ' occurs in this device when the depletion region at the rear of the device spreads into the π region.

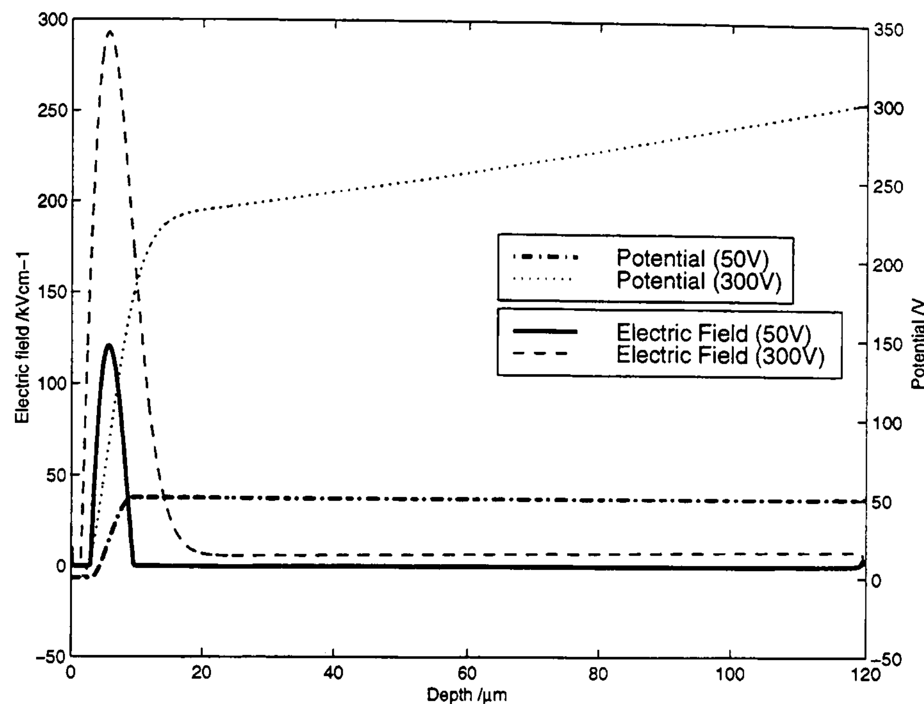

Figure 5.12: Variation in potential and electric field across the reverse reach through model at 50V and 300V.

The potential and electric field through the reverse reach through APD are shown in figure 5.12. The gain region in this device is broader and contains a lower peak electric field than for the reach through APD. Thus this device utilises a longer multiplication path, where the charge carriers undergo less multiplication per unit length than in the reach through structure but the increased width of the gain region means that appreciable gain values are still possible. The structure of the gain region affects the noise characteristics of the device. Typically, for a particular type of structure, a narrow high field region will result in a higher k factor. hence worse noise performance, than in a device employing a broader low field region [95].

5.2.3 Dark Current

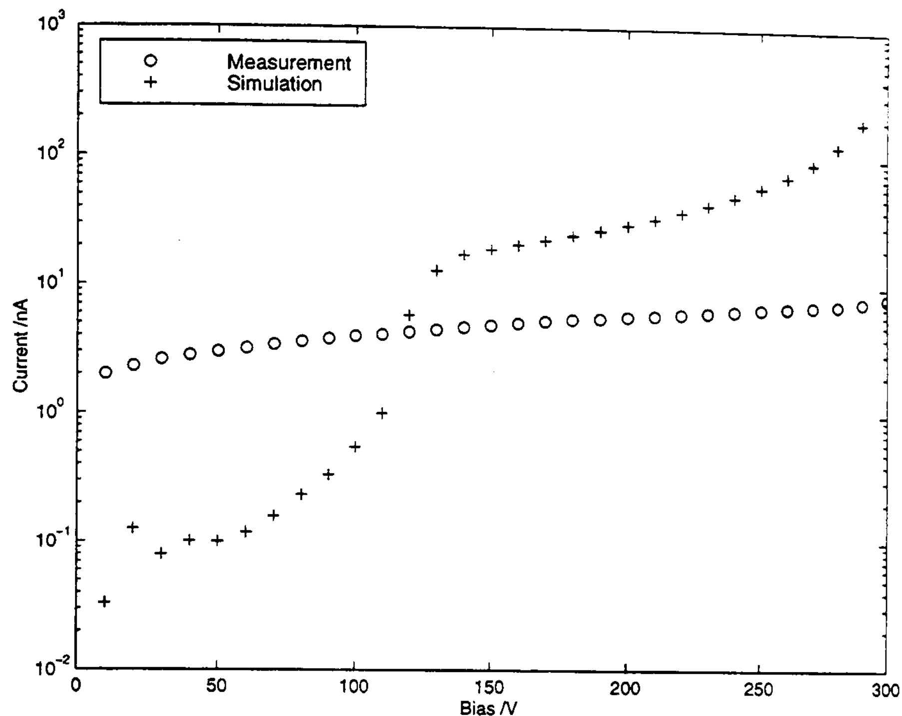

Figure 5.13: Comparison of the simulated bulk dark current from the reach through model with the measured total dark current from an EG&G C30916E reach through APD.

Figure 5.13 shows a comparison of the bulk dark current from the reach through APD model with the measured total dark current from a C30916E reach through APD. The modelled bulk dark current is multiplied by the APD in the same way as the measured signal. The distinctive knee in the curve shows where the device 'reaches through'. At this point the rapid increase in the gain with applied bias is curbed as the depletion spreads into the π region. A significant fraction of the potential drop then occurs outside the gain region, suppressing the increase in the electric field. Generally the surface leakage current is greater than the bulk leakage current [33]. This is confirmed by the measured data. The distinctive knee is not present, indicating that the measured current has not undergone multiplication, hence is surface leakage current.

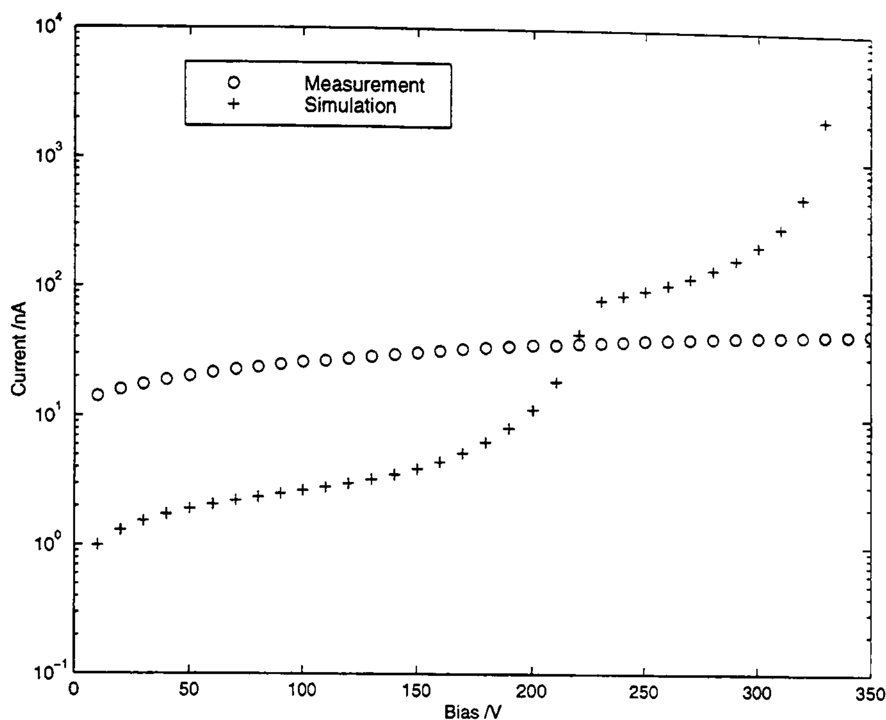

Figure 5.14: Comparison of the simulated bulk dark current from the reverse reach through model with the measured total dark current from an EG&G C30719F reverse reach through APD

Figure 5.14 shows a similar comparison between the modelled reverse reach through APD and measurements from a C30719F reverse reach through APD. The modelled bulk dark current clearly shows the point at which the device reaches through. The measured current is again dominated by the surface leakage current.

5.2.4 Photocurrent

Figure 5.15 shows a comparison of the predicted photocurrent from the reach through APD model with the measured photocurrent from a C30916E APD. To allow for the different illumination levels the curves are normalised at 50V. The modelled data show excellent qualitative agreement with the measured data. In both data sets the point at which the device 'reaches through' is clearly visible. The characteristic curve attributed to reach through devices is described well [94]. Section 3.3.2 describes the method used to evaluate the gain from the measurements of the photocurrent. The photocurrent at 50V is used for both the reach through model

and the C30916E.

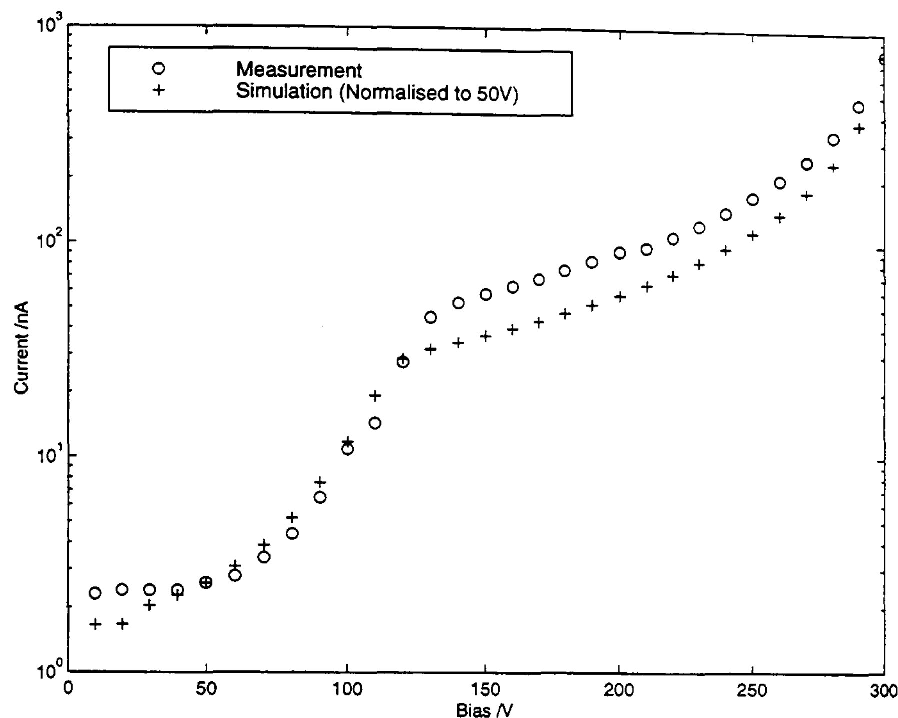

Figure 5.15: Comparison of the simulated photocurrent due to 650nm illumination calculated for the reach through model with the measured photocurrent from a C30916E APD.

A similar comparison is shown in figure 5.16. The photocurrent measured from the C30719F is compared with the reverse reach through model. The curves are normalised at 100V. Good qualitative agreement is again demonstrated, with the characteristic 'knee' due to 'reach through' visible in both plots. The gain for both the reverse reach through model and the C30719F are calculated using the photocurrent at 100V.

5.2.5 Gain

Perhaps the most important parameter relating to APDs is their gain. The experimental evaluation of the gain relies on the assumption that there is a bias at which unity gain occurs and efficient collection of the signal charge is possible. Figure 5.17 shows the gain measured from a C30916E reach through APD compared with gain. evaluated both directly and indirectly, from the modelled reach through APD.

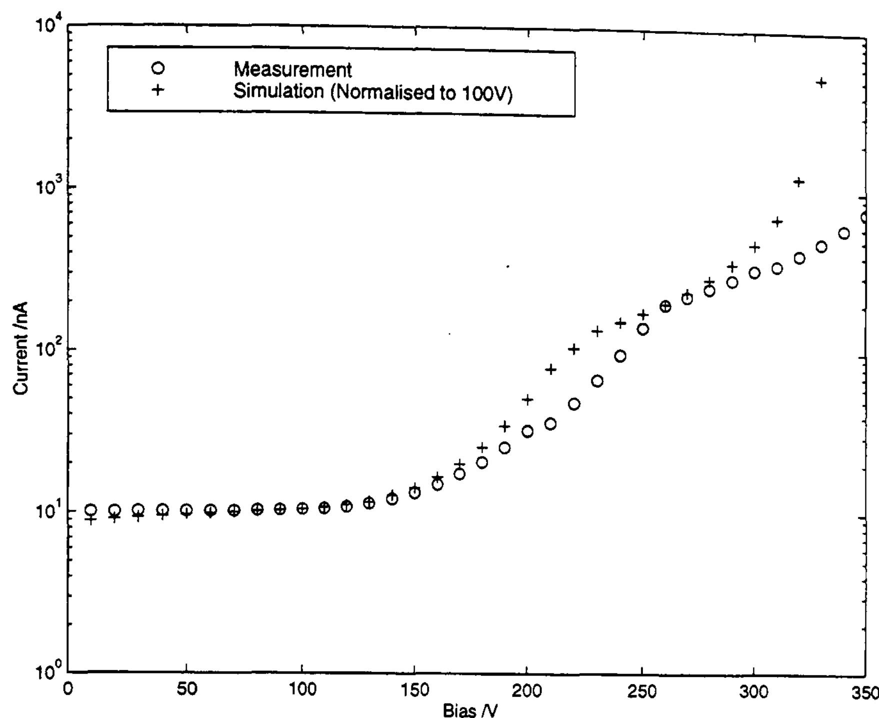

Figure 5.16: Comparison of the simulated photocurrent due to 650nm illumination for the reverse reach through model with the measured photocurrent from a C30719F APD.

The direct evaluation of the gain involves applying exactly the same techniques as used in the experimental evaluation (see chapter 3). The reference bias is taken to be 50V for the reach through devices. The indirect measurement refers to the use of APDGAIN (see chapter 4), which evaluates the gain of the device numerically. Both sets of modelled data show satisfactory agreement with the experimental data.

However it is clear from the plot that there is a discrepancy between the two methods in calculating the model gain. The gain evaluated directly, i.e. applying the experimental method, is consistently higher than the numerical evaluation. The experimental method assumes that the detection of the incident light peaks at a low bias before the gain becomes significant. This is suggested by a plateau in the measured photocurrent at low bias, (see section 3.3.2). In reality, for a typical reach through APD, full depletion does not occur until after the device has 'reached through'. At this point any increase in the light detected is hidden by the rapid increase in the gain. This leads to an over-calculation of the gain due to the under-

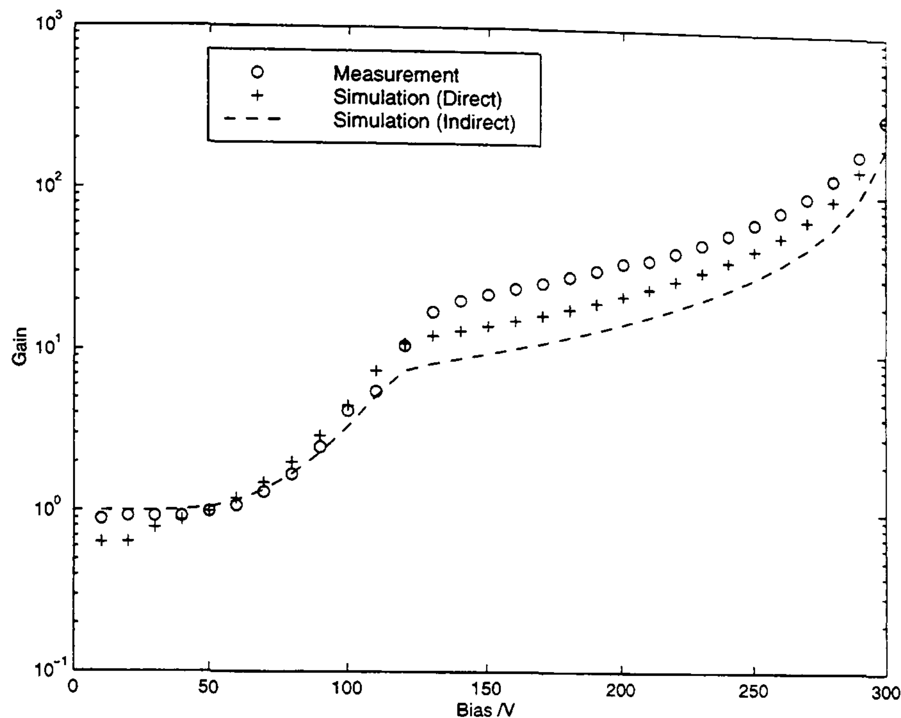

Figure 5.17: Comparison of the gain measured from an EG&G C30916E reach through APD and the predicted gain from the reach through model, evaluated directly and indirectly.

estimation of the un-multiplied photocurrent.

The gain calculated directly from the model can be considered to represent the gain measured experimentally, whereas the gain measured indirectly, i.e. via numerical analysis of the electric field, represents the actual multiplication a charge carrier undergoes when traversing the gain region. The complementary methods used to calculate the gain from the APD model allow us to see the relationship between the measured gain and the 'multiplication factor' i.e. the true multiplying power of the gain region.

Figure 5.18 shows the corresponding plot which compares the gain, calculated both directly and indirectly, from the reverse reach through APD model with the gain measured for a C30719F reverse reach through APD. The qualitative agreement between the measured and simulated gain is good, although the C30719F 'reaches through' at a higher reverse bias than the model.

The direct and indirect methods used to calculate the model gain produce more

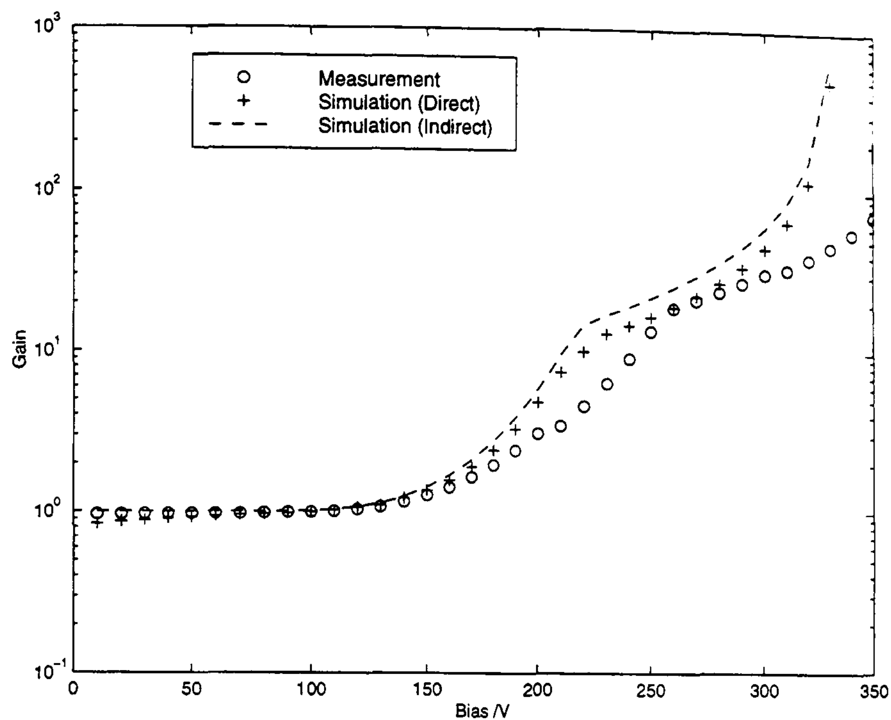

Figure 5.18: Comparison of the gain measured from an EG&G C30719F reverse reach through APD and the predicted gain from the reverse reach through model, evaluated directly and indirectly.

consistent results in this case. This is due to the design of the reverse reach through APD, where the gain region is situated near to the front of the device. At low bias the spread of depletion in this diode, figures 5.8 to 5.11, is sufficient in the narrow region in front of the gain region to collect the incident light efficiently. When the device 'reaches through', any light collected beyond the gain region does not contribute significantly to the overall signal.

Thus the assumptions made in the experimental method appear to be fulfilled more satisfactorily for the reverse reach through structure than for the reach through structure. This is true at shorter wavelengths, where the light is absorbed completely in front of the gain region. For longer wavelengths a large fraction of the light may be absorbed past the gain region. The holes generated by the incident light drift to the gain region, and these undergo less multiplication than the injected electrons. Now the condition exists whereby only the charge carriers generated in the small region in front of the gain region are subject to the full gain or 'multiplication factor'

of the device. Consequently the gain will appear to fall with increasing incident wavelength. This effect is investigated in section 5.2.7.

5.2.6 Excess Noise Factor

The measurement and evaluation of the experimental and simulated excess noise factors are described in sections 3.3.4 and 4.3.3 respectively. The experimental evaluation assumes a simple form for the relation between the excess noise factor and the gain, which is valid for gains greater than about 10. A single value of k_{eff}, the weighted average of the ionisation co-efficients, is used to evaluate the excess noise factor. k_{eff} varies with the applied bias but can be assumed to be constant when the gain is appreciably greater than unity. Figures 5.19 and 5.20 show how the calculated values of k_{eff} vary with the gain, for the reach through and reverse reach through models respectively. The plots demonstrate that the value of k_{eff} does tend to become constant when the gain approaches a value of 10, although in the simulation the value of k_{eff} is calculated at each gain value

Figure 5.21 compares the excess noise factor measured for the C30916E APD with the predictions from the reach through APD model. Figure 5.22 shows the same comparison for the C30719F APD and the reverse reach through APD model. There is good agreement between the measured and simulated data for both device types although the simulated data for the reverse reach through model are slightly higher than the measured data. This suggests that the gain region in the reach through model utilises higher average field strength than present in the C30719F APD. At high electric fields the ratio of the ionisation coefficients, i.e. k, tends to increase resulting in an increase in the excess noise factor.

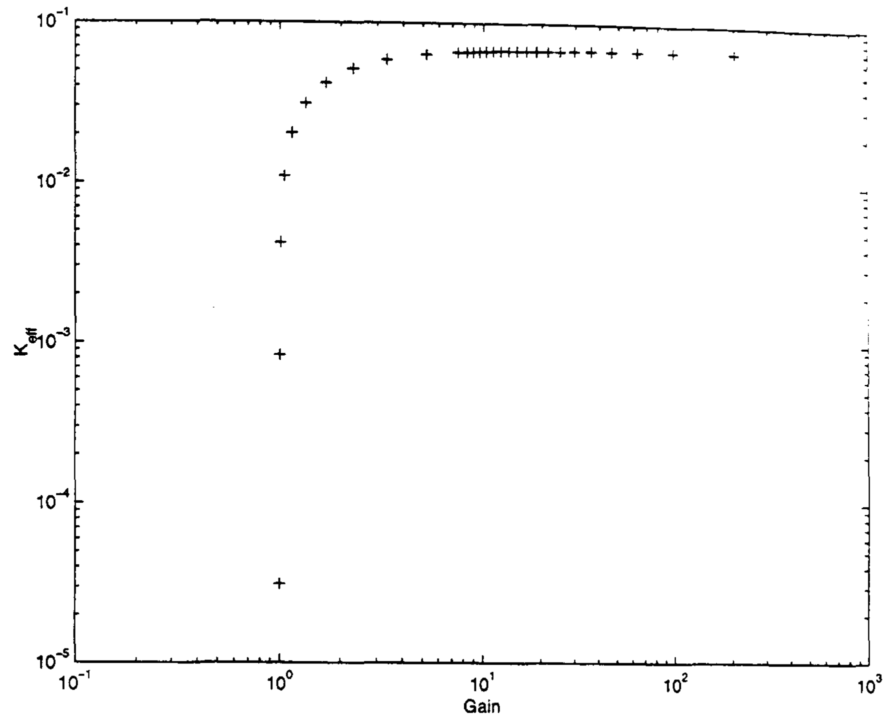

Figure 5.19: Plot showing the simulated variation in k_{eff} with gain for a reach through model.

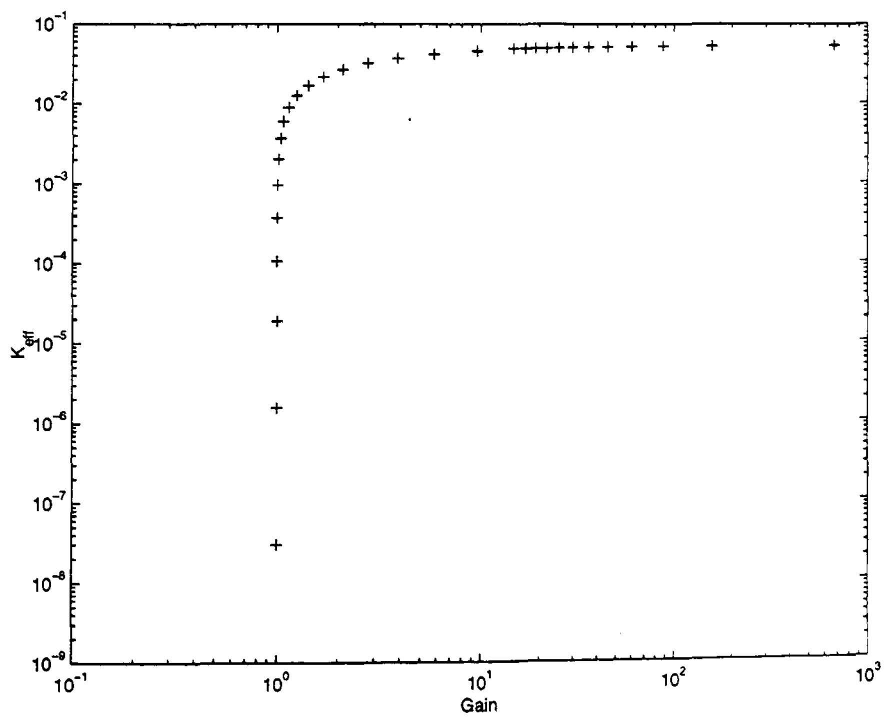

Figure 5.20: Plot showing the simulated variation in k_{eff} with gain for a reverse reach through model.

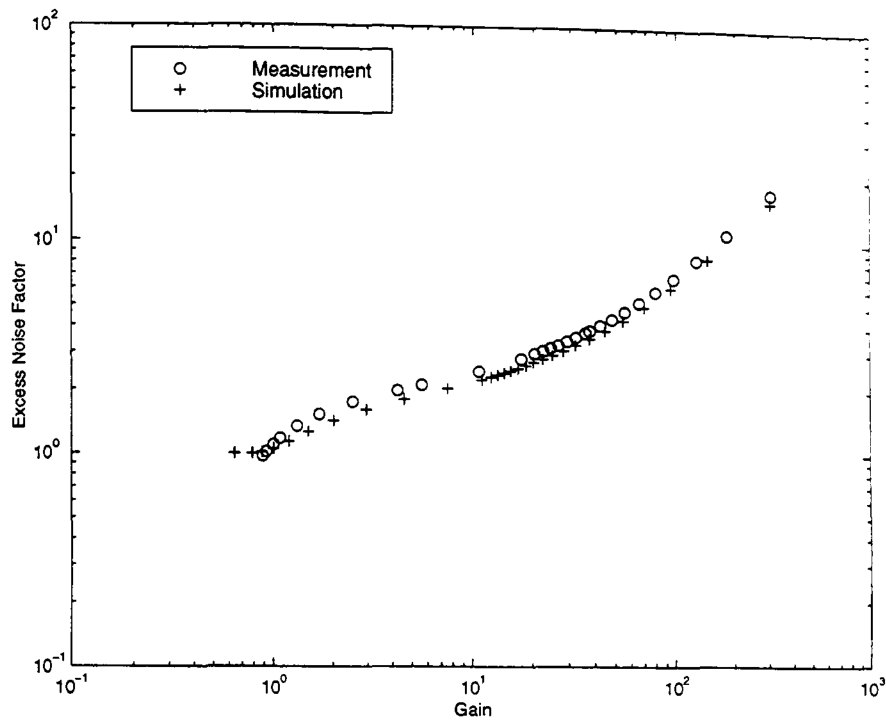

Figure 5.21: Comparison of the excess noise factor measured for a C30916E APD and the predicted excess noise factor from the reach through APD model.

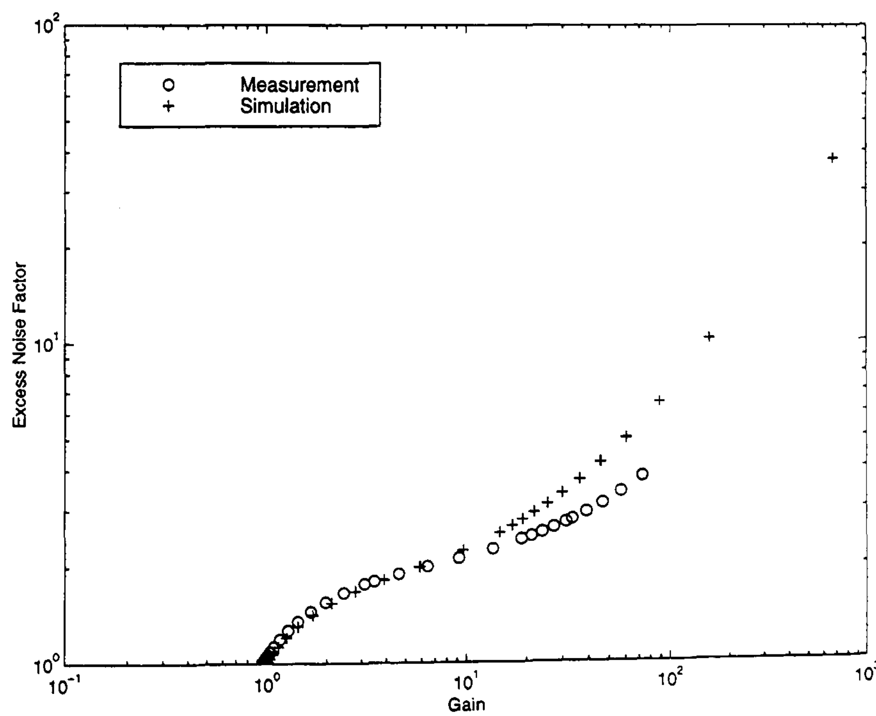

Figure 5.22: Comparison of the excess noise factor measured for a C30719F APD and the predicted excess noise factor from the reverse reach through model.

The value of k_{eff}, hence the excess noise factor, is not solely dependent on

the ratio of the ionisation coefficients, but also the structure of the gain region. Comparison of the calculated excess noise factors for the reach through and reverse reach through models show that the excess noise factor calculated for the reverse reach through model is comparable, if not higher, than for the reach through model. One would expect, if only considering k, that the excess noise factor for the reach through model should be greater, as the peak electric field is higher. This is a result of the contrasting structures of the devices, and can be explained in terms of the weighting factor, $M(x)^2$, in the definition of k_{eff} (see equation 4.43).

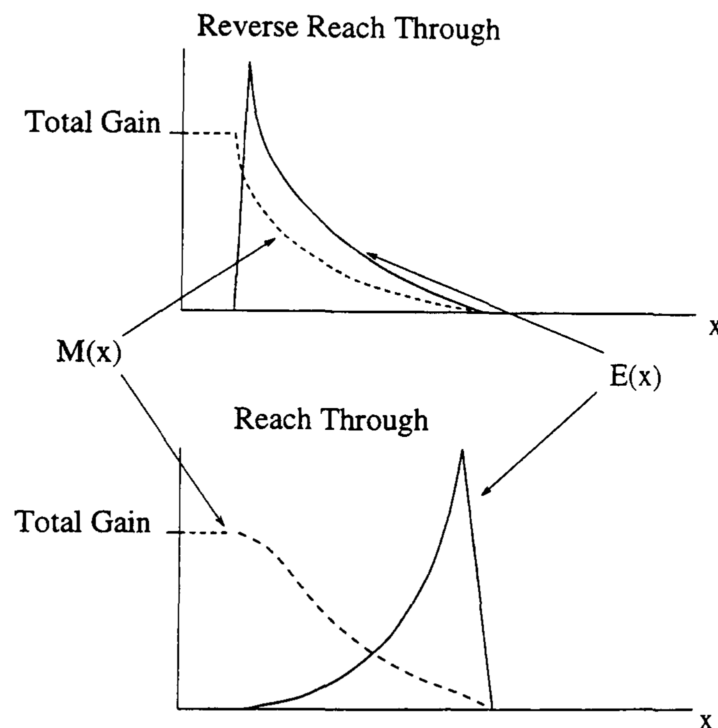

Figure 5.23: Schematic showing the variation of the gain with position for a reach through and reverse reach through structure superimposed on the peak electric field region.

Figure 5.23 shows schematically the variation of gain with position through the models superimposed on the electric field profile. The incident electron will see a rapidly rising electric field, that slowly falls in a reverse reach through device (cf. figure 5.12), and the converse for the reach through structure (cf. figure 5.7). This results from the levels of doping used in the junctions, and hence is structure dependent. When the variation in gain through the device, shown schematically in

figure 5.23, and the value of k_{eff}, which approximates to k_2 (see equation 4.45), are consisdered then the noise performance of the devices can be explained. In the reverse reach through device the value of $M(x)$ is highest in the high electric field region, thus increasing the weighting of the high k values in k_{eff}. Conversely for the reach through device, the gradual increase in the electric field results in a low value of $M(x)$ at the peak field, thus reducing the weighting in that region. The consequence is that the reverse reach through APD will exhibit a worse noise performance, compared to the reach through device, for the same peak field, as suggested by the simulated data.

5.2.7 Photosensitivity

The photosensitivity of a device is defined as the ratio of the photocurrent per watt of optical power incident on the device. The measurement of the photosensitivity is described in detail in section 3.3.3. The photosensitivity of the simulated devices is easily determined from the ratio of the photocurrent and the incident power. The wavelength and photon flux are parameters in the simulation, hence the incident power was easily calculated.

Figure 5.24 compares the photosensitivity measured from a C30916E APD with the calculated photosensitivity from the reach through APD model. The broad spectral response of the reach through structure results in an almost linear response, in the measured and simulated data, over the range of wavelengths investigated.

Figure 5.25 shows the same comparison using measurements from the C30179F APD and data from the reverse reach through APD model. The difference between the response of the reach through and reverse reach through APD structures is clearly visible and is replicated by the simulated data. The C30917F APD has a much narrower response than the C30916E APD. The peak photosensitivity is at 600nm, this falls by 25% at 450nm and 800nm.

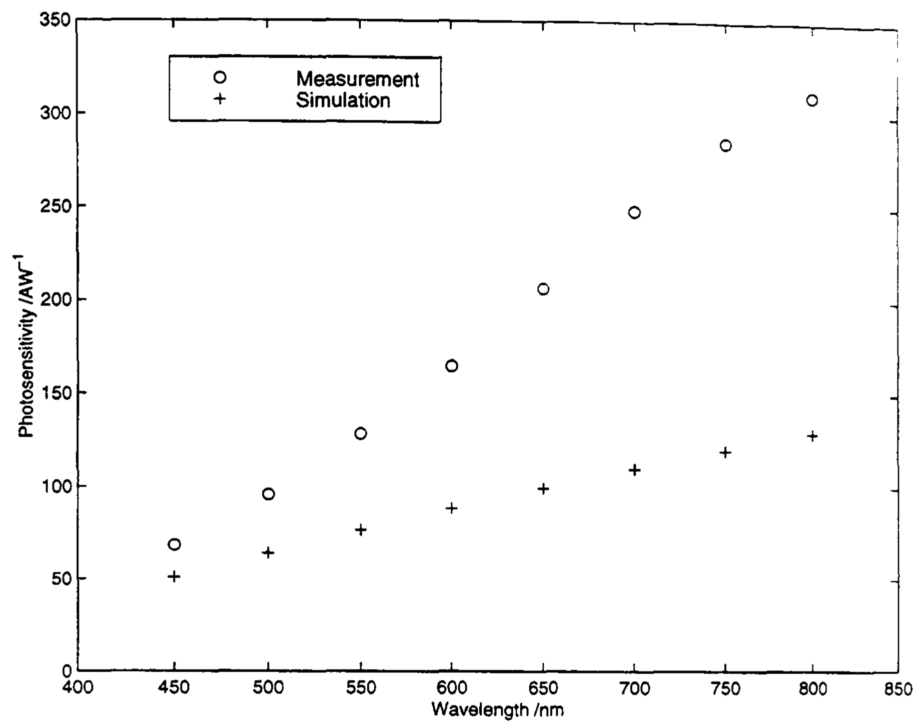

Figure 5.24: Comparison of the photosensitivity measured for a C30916E APD and the predicted photosensitivity from the reach through model at 300V.

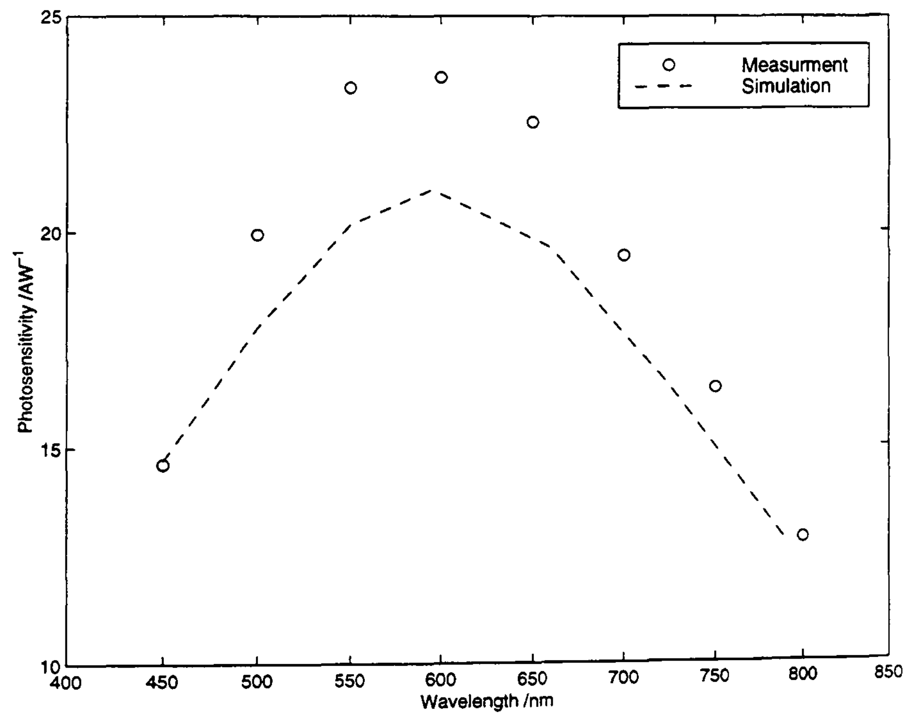

Figure 5.25: Comparison of the photosensitivity measured for a C30719F APD and the predicted photosensitivity from the reverse reach through model at 300V.

The photosensitivity is affected by variation in the gain. Figure 5.26 shows the gain measured for the C30916E APD and predicted by the reach through APD model. Both the measurements and the predictions remain un-affected by variation in the incident wavelength. Figure 5.27 shows the same plot for the C30719F APD and the reverse reach through model. Now the gain falls dramatically as the incident wavelength increases, this effect has been measured in similar devices [96]. The fall is due to incident light being absorbed in, or even beyond the gain region, as described in section 5.2.5. The fall in the measured gain is essentially a mis-calculation of the gain. The multiplying power of the gain region is not affected by the change in incident wavelength, there is simply less of the initial photo-generated charge being multiplied.

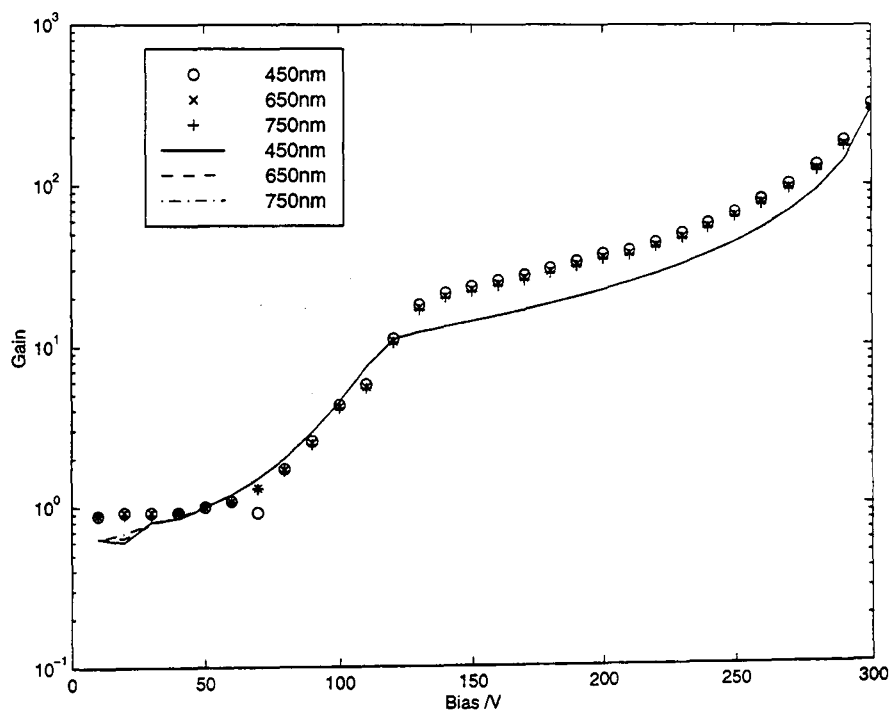

Figure 5.26: Plot showing the variation in gain with incident wavelength measured for a C30916E APD and predicted by the reach through model. The data points show the measurements and the lines show the model's predictions.

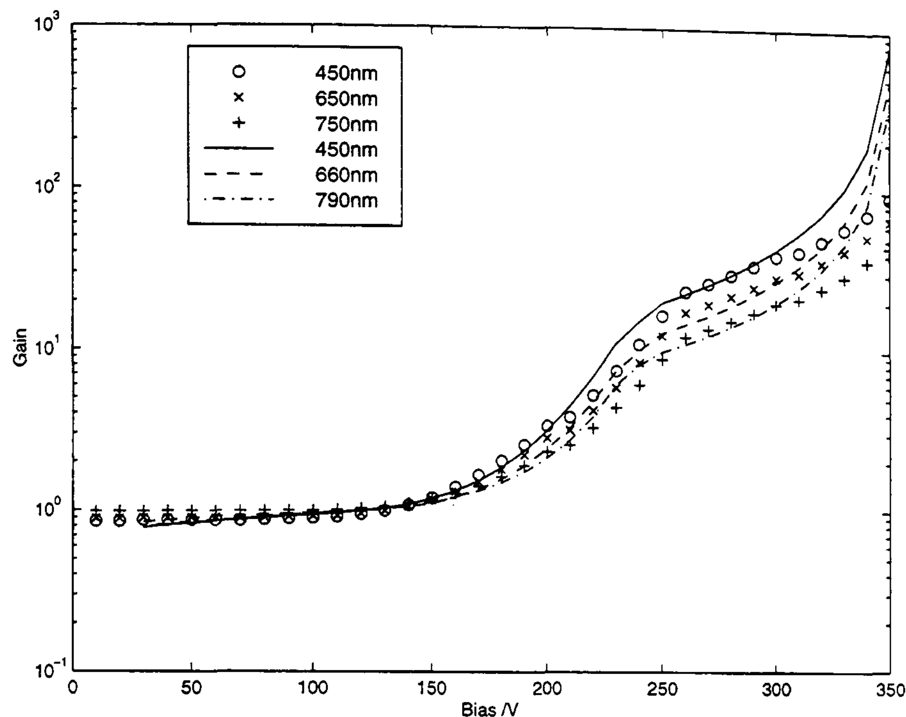

Figure 5.27: Plot showing the variation in gain with incident wavelength measured for a C30719F APD and predicted by the reverse reach through model. The data points show the measurements and the lines show the model's predictions.

5.3 Post-Irradiation

The devices were irradiated at the Rutherford Appleton Laboratory's ISIS facility (see section 3.3.6). To allow useful comparison between the dose received at different neutron irradiation facilities, it is common to express the flux in terms of 1Mev neutrons. This is achieved by multiplying the integrated flux over a specific energy range e.g. > 10KeV, by the hardness parameter. The hardness parameters are available for most facilities, for the ISIS facility the hardness parameter is 1.02 [97],[98]. Thus the integrated flux provided by ISIS can immediately be converted into the 1MeV equivalent. The following results report all the neutron fluences in terms of the 1MeV equivalent.

5.3.1 Reach Through APD

The effect of neutron irradiation on the internal structure of the reach through APD can be investigated using the simulation. At 50V the increase in the thermal

generation is clearly visible in the reach through structure, figures 5.28 and 5.29. This is due to the presence of traps, introduced by the irradiation. When fully depleted the large depletion region gives rise to increased thermal generation across the whole device, figures 5.30 and 5.31. This leads to a significant rise in the dark current.

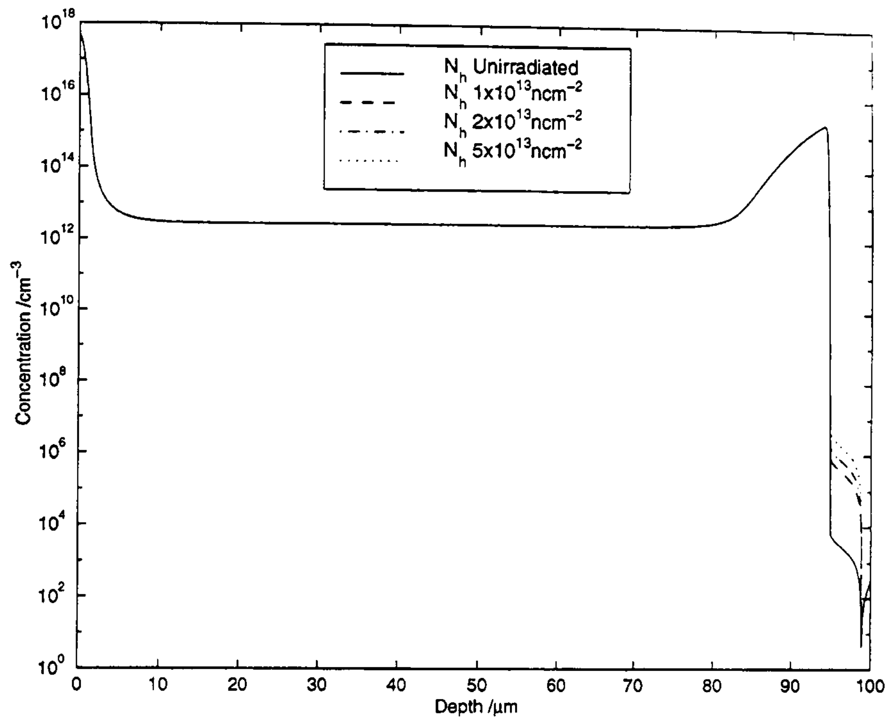

Figure 5.28: Plot showing the free hole concentration through the reach through APD model at 50V for several neutron fluences.

One of the principle aims of the model was to investigate the effect of the traps on the device performance, in particular the effects caused by the introduction of deep acceptors. Figure 5.32 plots the change in the potential from the un-irradiated value, for several neutron fluences predicted by the reach through APD model. The negative charge distribution due to the filled deep acceptors, causes a small shift in the potential profile across the device. The distribution of filled deep acceptors through the device is plotted in 5.33. When fully depleted there is a uniform concentration of filled acceptors through almost the whole device.

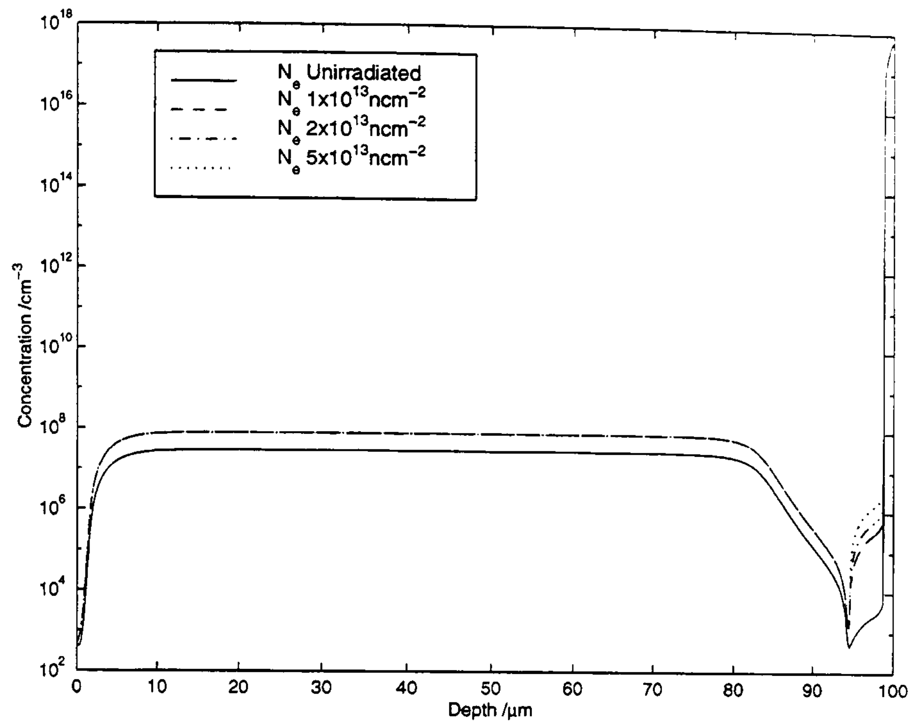

Figure 5.29: Plot showing the free electron concentration through the reach through APD model at 50V for several neutron fluences.

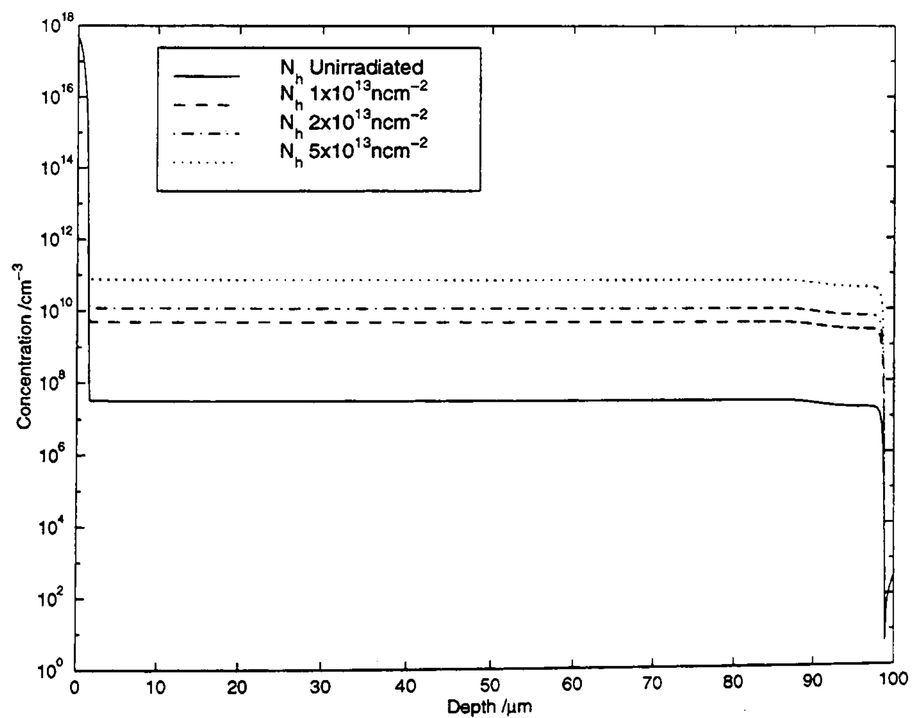

Figure 5.30: Plot showing the free hole concentration through the reach through model at 300V for several neutron fluences.

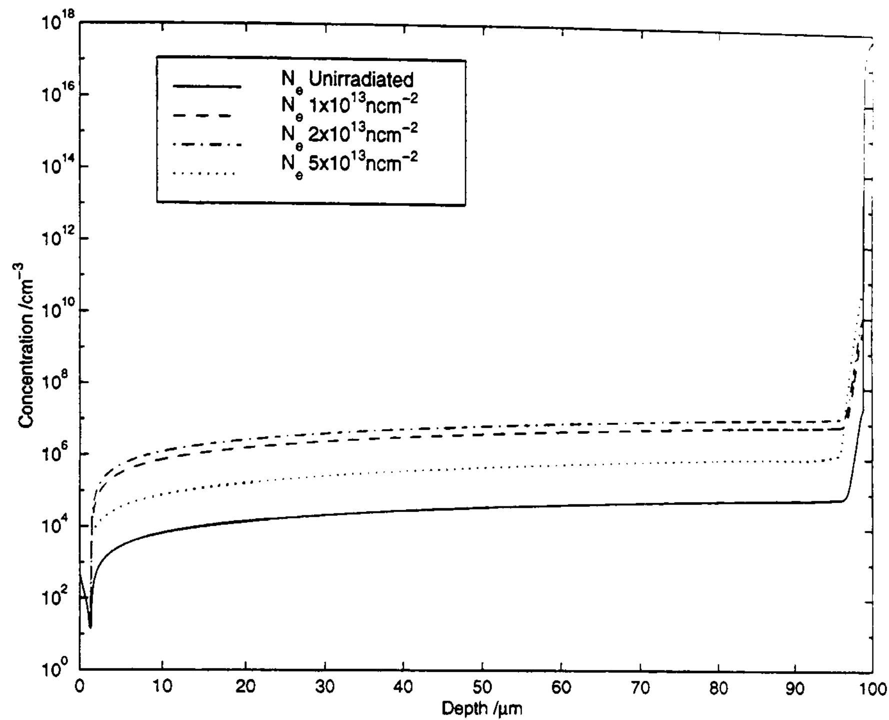

Figure 5.31: Plot showing the free electron concentration through the reach through model at 300V for several neutron fluences.

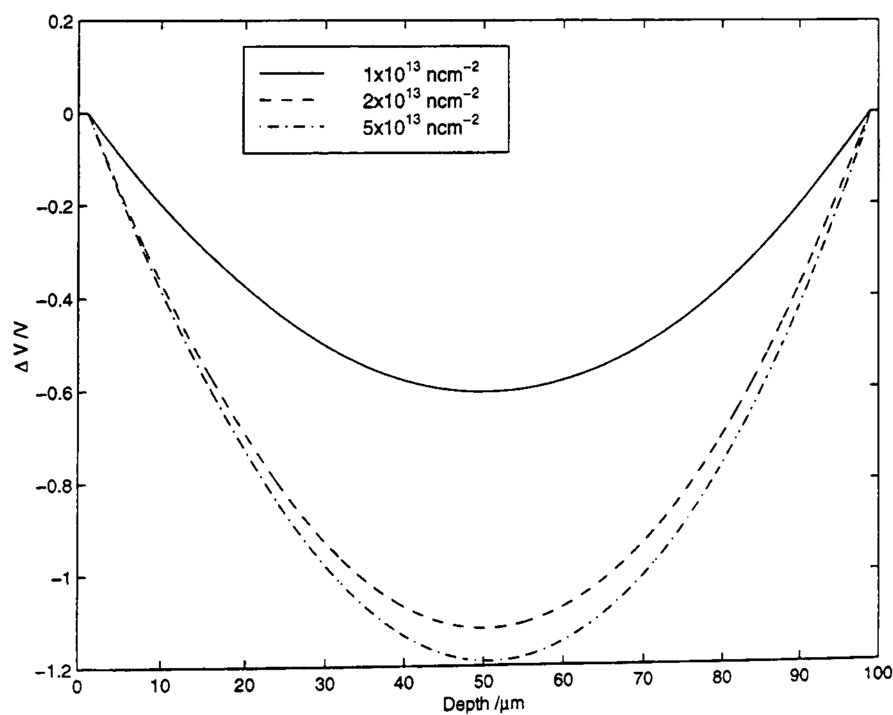

Figure 5.32: Plot showing the change in potential through the reach through APD model for several neutron fluences at 300V.

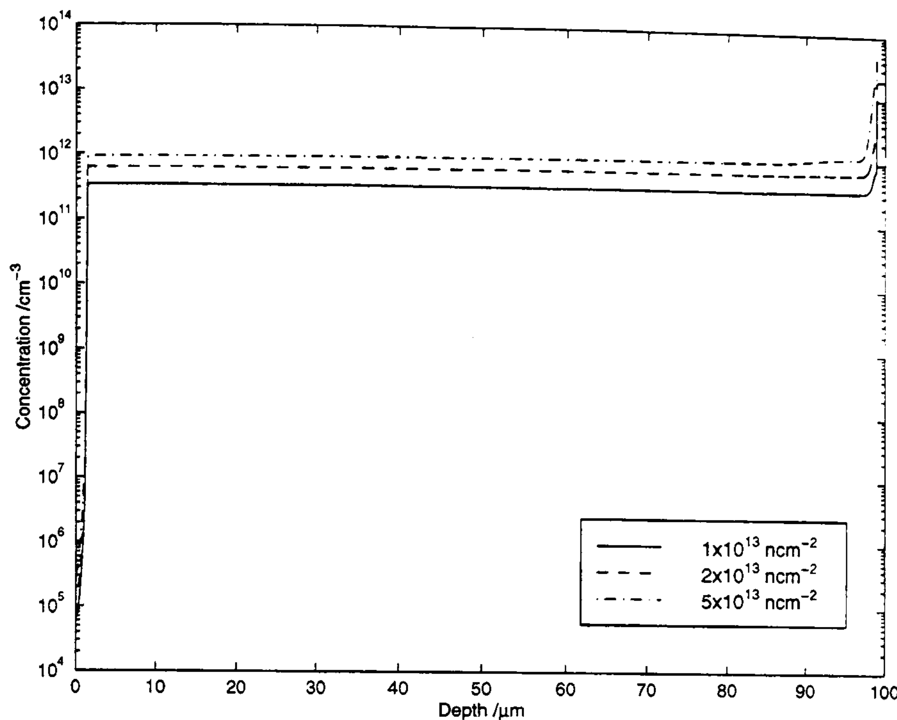

Figure 5.33: Plot showing the distribution of filled acceptors through the reach through model for several neutron fluences.

To describe qualitatively the macroscopic effects due to the introduction of the filled deep acceptor levels, the distribution of the filled traps should be considered. Figure 5.33 shows that the majority of the deep acceptors occur on the p side of the junction region. Thus the large build up of negative charge increases the potential drop across the reverse biased junction. This will have the effect of increasing the electric field in the gain region.

5.34 shows the simulated effect of the introduction of filled deep acceptors on the multiplication factor of the reach through APD. The multiplication factor of the device is predicted to increase after irradiation with neutrons. This effect has not been experimentally verified. There are several reasons for the lack of experimental verification.

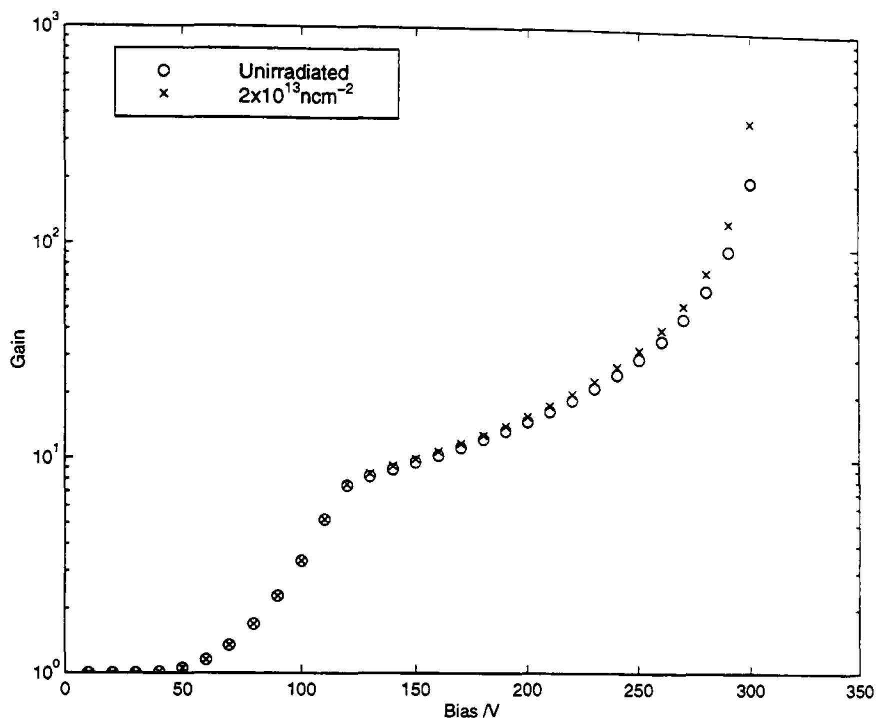

Figure 5.34: Plot showing the multiplication factor in the reach through model before and after neutron irradiation.

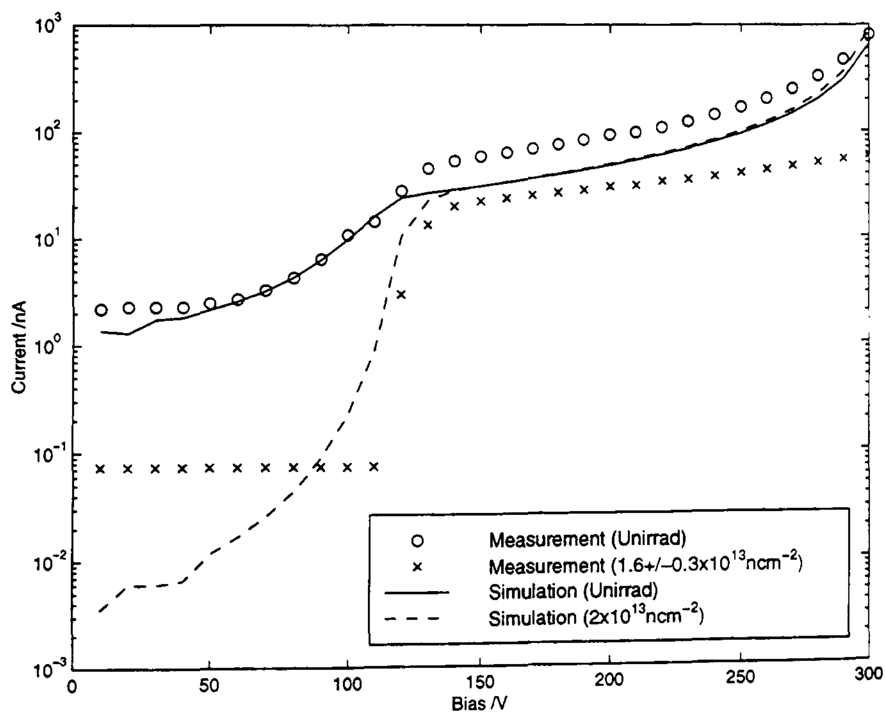

Figure 5.35: Plot showing the measured photocurrent in a C30916E APD and predicted by the reach through APD model before and after neutron irradiation.

Firstly, as figure 5.17 demonstrates, the exact evaluation of the multiplication factor is not a trivial process. This is particularly relevant in the case of the C30916E APD. Figure 5.35 shows the C30916E photocurrent measured before and after neutron irradiation. The photocurrent predicted by the reach through APD model is also shown. Both the predictions and the measurements show a severe degradation in the detection of light at low bias. This can be attributed to the increased recombination due to the traps introduced by the neutron radiation; a similar effect is observed in irradiated solar cells [99].

The model predicts this behaviour well, but does not explain the overall fall in the measured photocurrent or the flatter profile that occurs at higher bias. The discrepancies can be explained as follows. The uniform fall in the measured photocurrent can be attributed to surface damage in the device from the gamma background present during the irradiation. Surface effects are not included in the model, and hence cannot be re-produced. The C30916E APD is housed in a hermetically sealed TO package where the actual device is in limited contact with the case. After neutron irradiation and at high reverse bias, the total current can exceed $1\mu A$. Controlling self-heating in the device becomes difficult under these conditions. An increase in APD temperature will reduce the ionisation coefficients and hence the gain, even though the electric field may have increased in the gain region. Accurate evaluation of the gain, from the photocurrent measurements, is not possible because of the reduced charge collection at low bias. The un-multiplied photocurrent cannot be determined.

The measured change in the photosensitivity for the C30619E is dominated by the surface damage from the γ background present during the irradiation [100]. At 300V the fall is significant, figure 5.36. The model which excludes surface effects, due to its one dimensional nature cannot predict these effects. Although the model predicts the change in response at low bias, at high bias surface damage and self-heating become dominant in the C30916E performance.

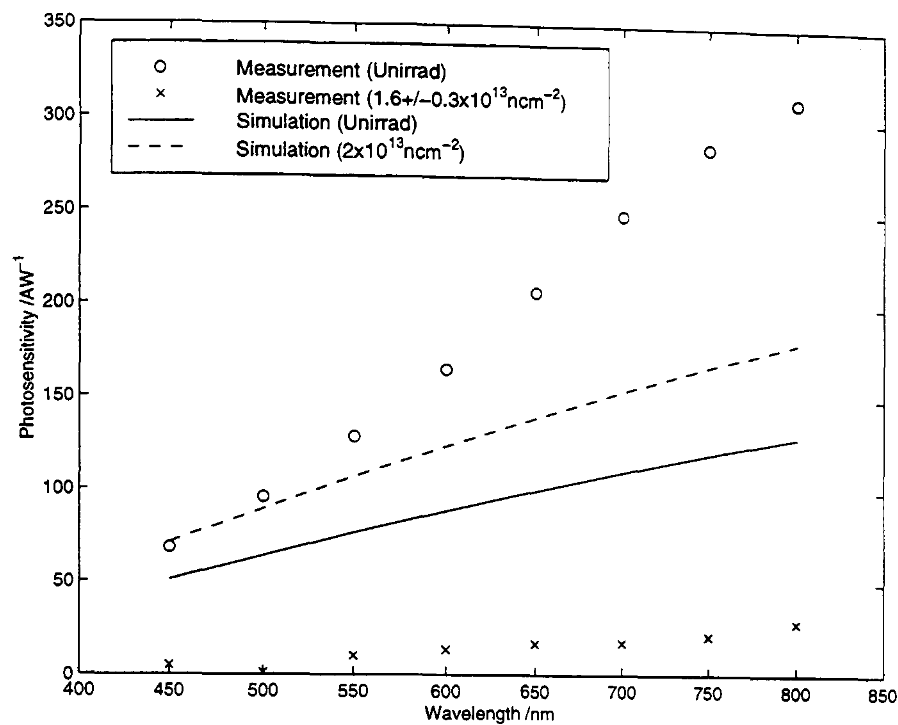

Figure 5.36: Plot showing the measured photosensitivity in a C30916E APD and predicted by the reach through model before and after neutron irradiation.

5.3.2 Reverse Reach Through APD

Figures 5.37 and 5.38 show the affect of neutron irradiation on the free hole and electron concentration in the reverse reach through APD model at 50V. As with the reach through APD a large increase in the thermal generation is visible in the depleted region at the front of the device. At 300V, figures 5.39 and 5.40, there is a uniform increase in the thermal generation across the majority of the device, which is almost completely depleted.

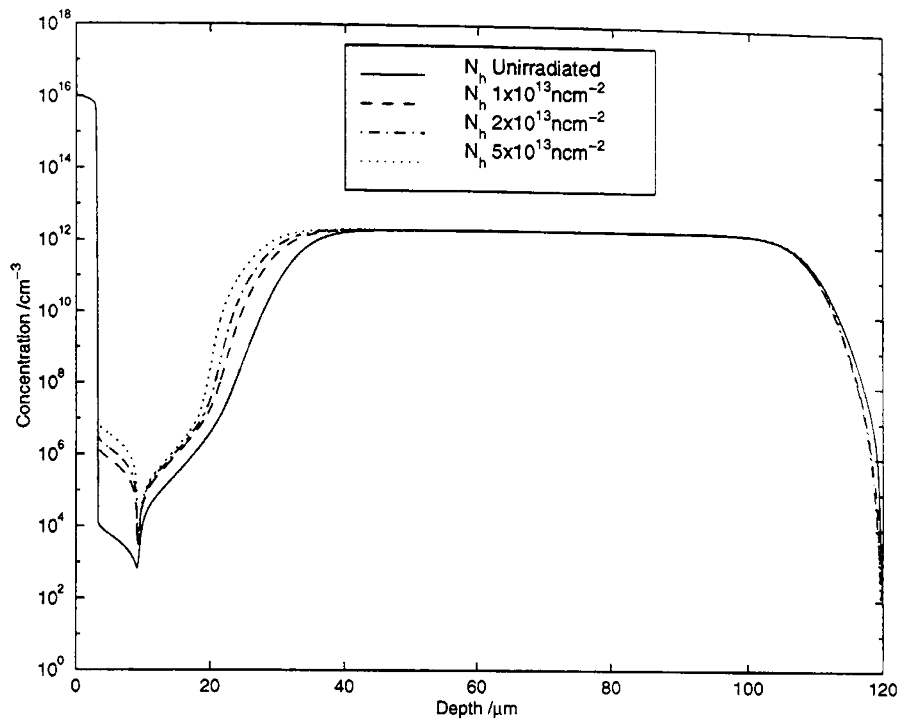

Figure 5.37: Plot showing the free hole concentration through the reverse reach through model at 50V for several neutron fluences.

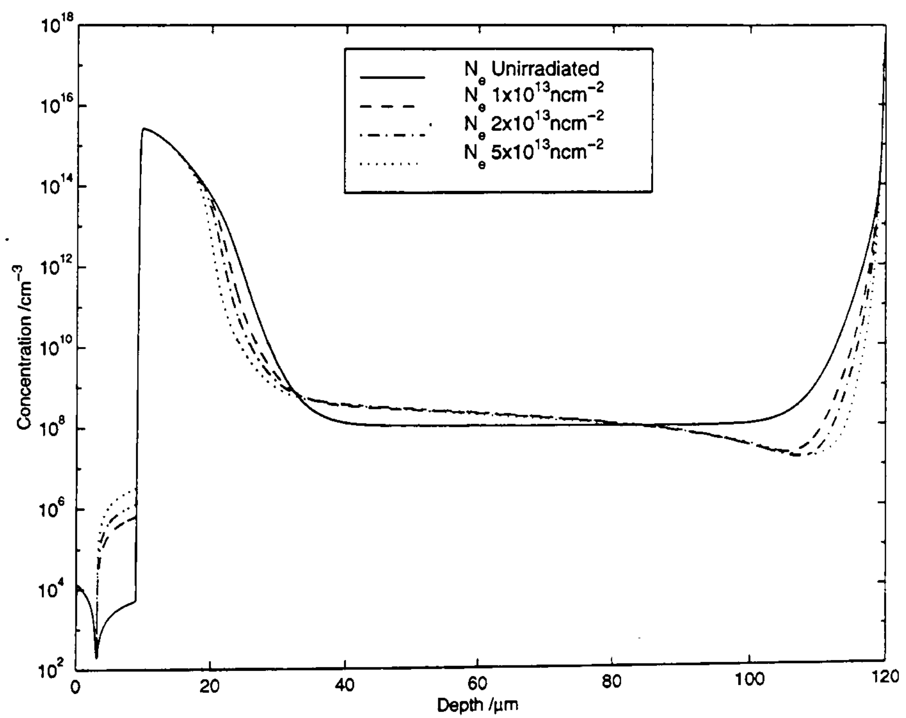

Figure 5.38: Plot showing the free electron concentration through the reverse reach through model at 50V for several neutron fluences.

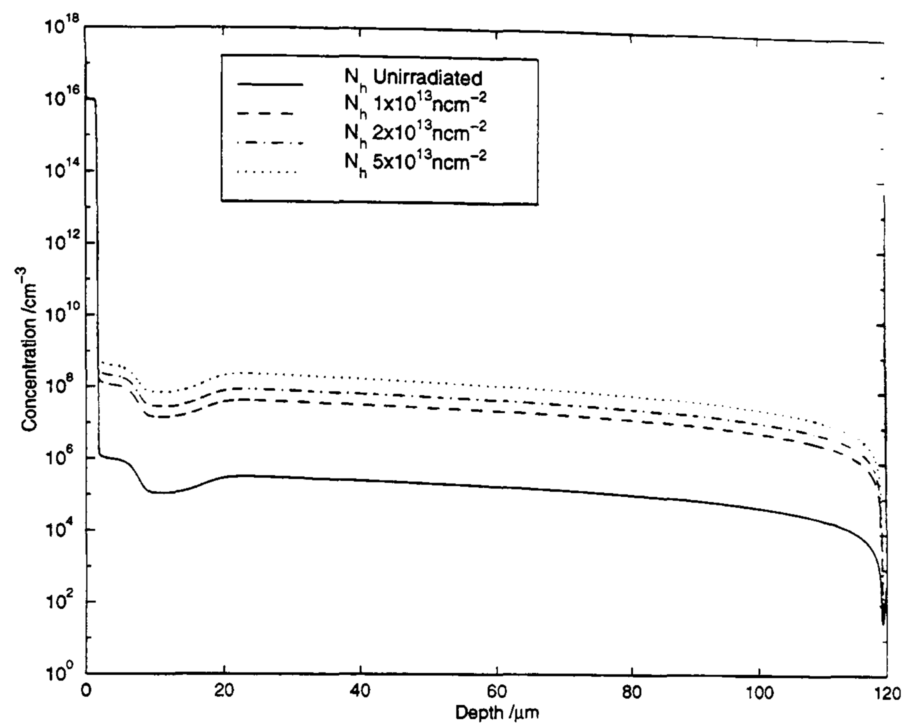

Figure 5.39: Plot showing the free hole concentration through the reverse reach through model at 300V for several neutron fluences.

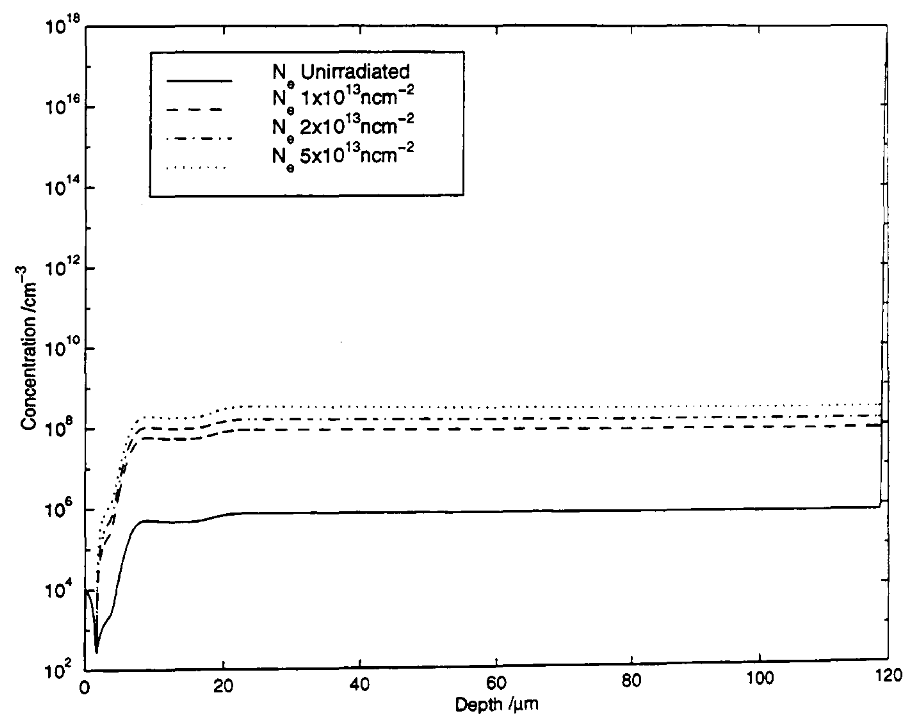

Figure 5.40: Plot showing the free electron concentration through the reverse reach through model at 300V for several neutron fluences.

Figure 5.41 shows the predicted shift in the potential through the reverse reach through APD. The plot is very similar to figure 5.32 but the magnitude of the shift is much greater for the reverse reach though APD. When the potential through the reverse reach through APD is plotted for several neutron fluences, figure 5.42, the shift is clearly visible. The similarity can be understood by comparing figures 5.43 and 5.33. The uniform distribution of filled acceptors through the reverse reach through APD, figure 5.43, is similar to that in the reach through APD.

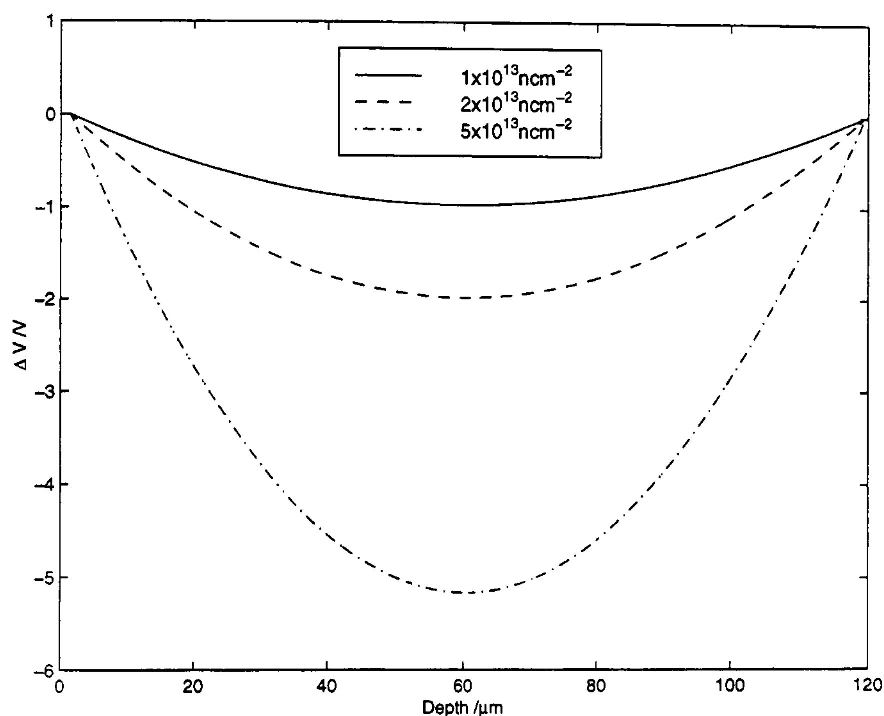

Figure 5.41: Plot showing the change in potential across the reverse reach through model for several neutron fluences at 300V.

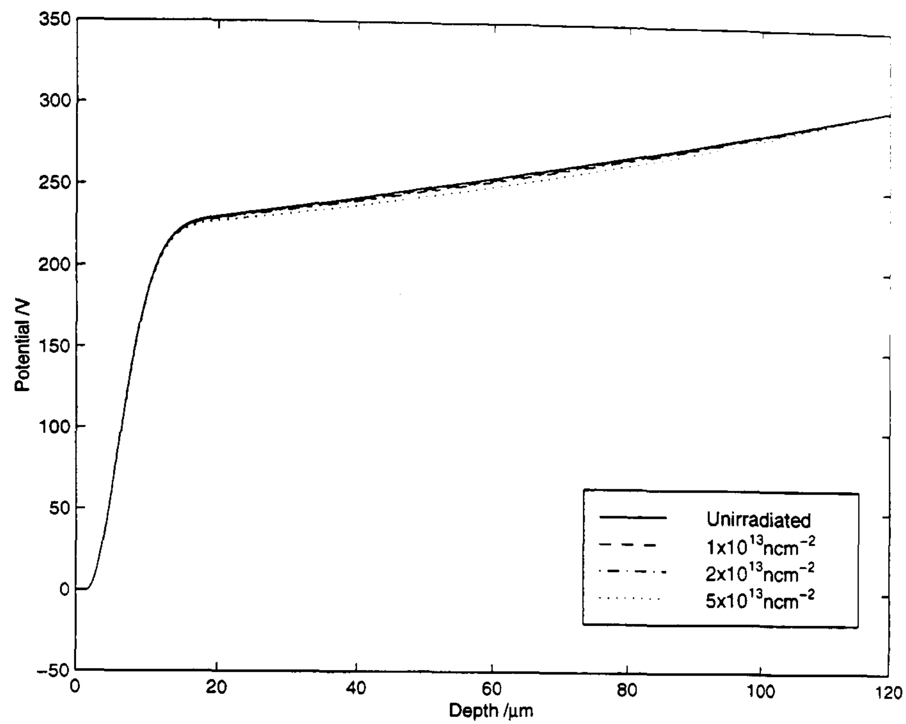

Figure 5.42: Plot showing the potential across the reverse reach through model at 300V before and after neutron irradiation.

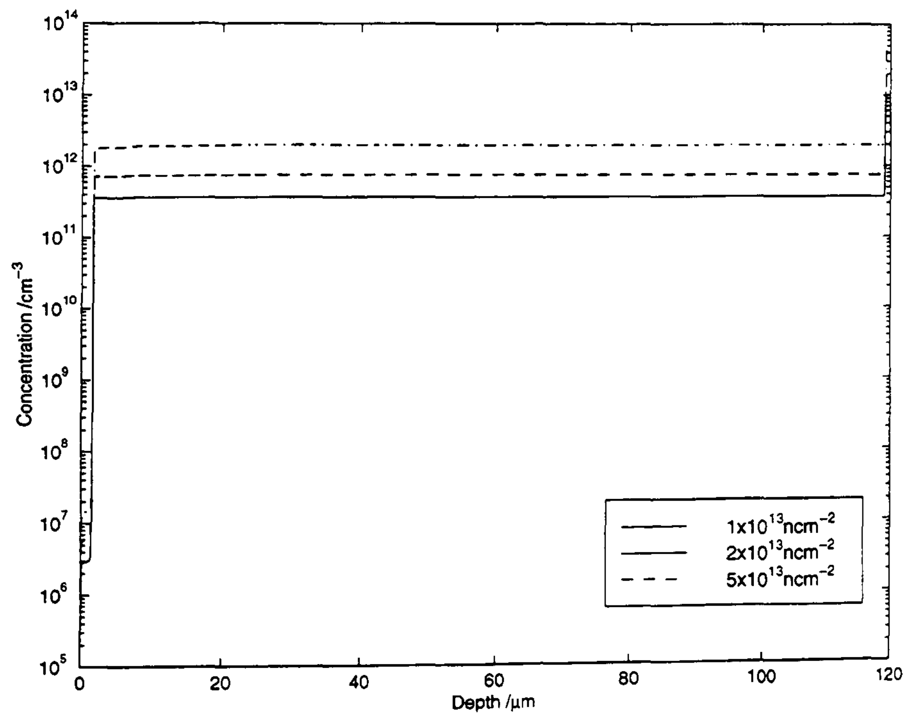

Figure 5.43: Plot showing the distribution of filled acceptors through the reverse reach through model for several neutron fluences.

The multiplication factor predicted by the reach through APD model, figure 5.34, showed an increase after neutron irradiation. The change in the multiplication factor with neutron fluence, predicted by the reverse reach through model, is shown in figure 5.44. In contrast to the reach through APD model the multiplication factor reduces after neutron irradiation. This is also due to the presence of negative space charge caused by the filled deep acceptors. The design of the reverse reach through APD results in the majority of the space charge forming on the n side of the junction. This has the opposite effect to that observed in the reach through model. The potential difference across the gain region is reduced, resulting in a drop in the electric field and the gain.

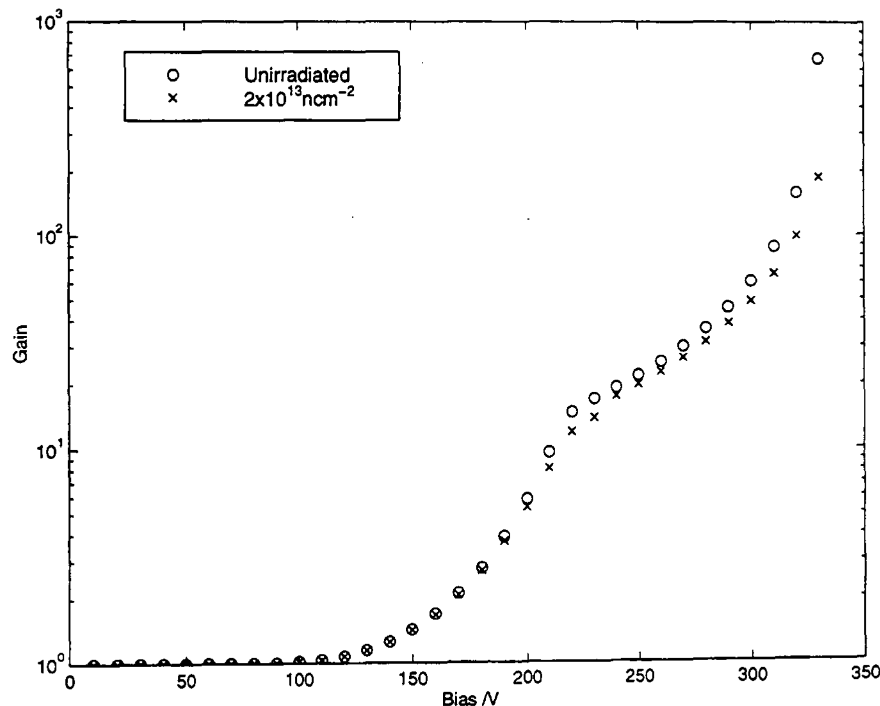

Figure 5.44: Plot showing the multiplication factor predicted by the reverse reach through model before and after neutron irradiation.

Figure 5.45 shows the measured photocurrent for a C30719F, before and after neutron irradiation. The photocurrent predicted by the reverse reach through APD model is also shown. Unlike the C30619E, the C30719F does not show any significant degradation in the low bias charge collection. This is due to the position of the gain region, whereby the majority of the signal charge is still generated in the depleted

region. There is a uniform fall in the measured photocurrent, not predicted by the model, again this is attributed to surface damage introduced during the irradiation.

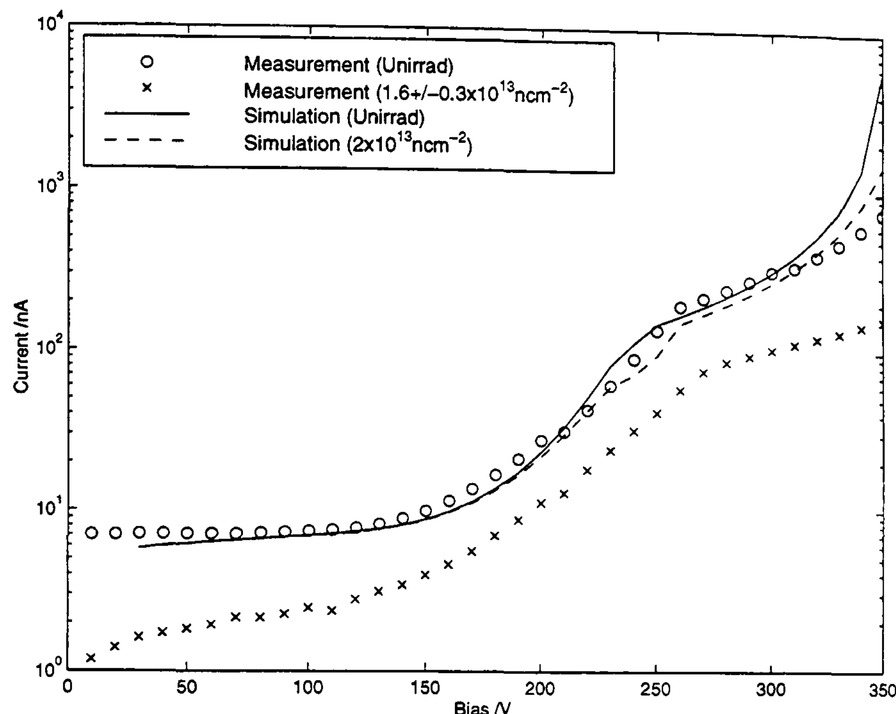

Figure 5.45: Plot showing the measured photocurrent in a C30719F APD and predicted by the reverse reach through model before and after neutron irradiation.

Figure 5.46 compares the gain measured for the C30719F with the gain predicted by the reverse reach through APD model, both before and after neutron irradiation. The predicted gain has been shifted along the x-axis to aid the comparison. The experimental results show a fall in the gain, that is replicated well by the model. It can be considered that after neutron irradiation the gain curve is actually shifted along the bias axis. This idea was suggested by Y. Musienko et al, when presenting results after the irradiation of C30626E reverse reach through APDs [15]. The effect only becomes significant when the device is depleted and the re-arrangement of free carriers cannot cancel the effect of the filled acceptors. The shift in the gain is seen to occur, both experimentally and from the model's predictions, just before the device 'reaches through'. At very high reverse bias the role of self-heating may play a small part in the reduction of the gain, although the packaging of the C30719F in *flatpacks* allowed much better temperature control.

The photosensitivity of the C30719F measured before and after neutron irradiation is shown in figure 5.47. The predictions from the reverse reach through APD model are also shown. The model predicts that the reduced photosensitivity is completely described by the fall in gain. The measured fall in the photosensitivity is also affected by surface damage, which is not included in the model. Thus the measured fall in the photosensitivity is not completely predicted by the model.

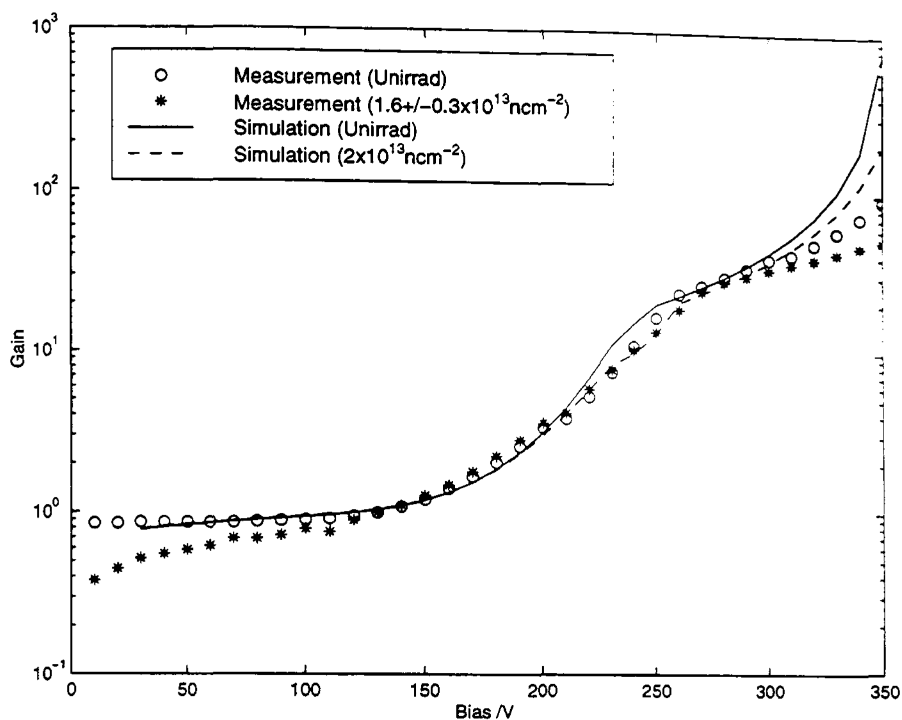

Figure 5.46: Plot showing the change in the measured gain for the C30719F APD and predicted by the reverse reach through model before and after neutron irradiation.

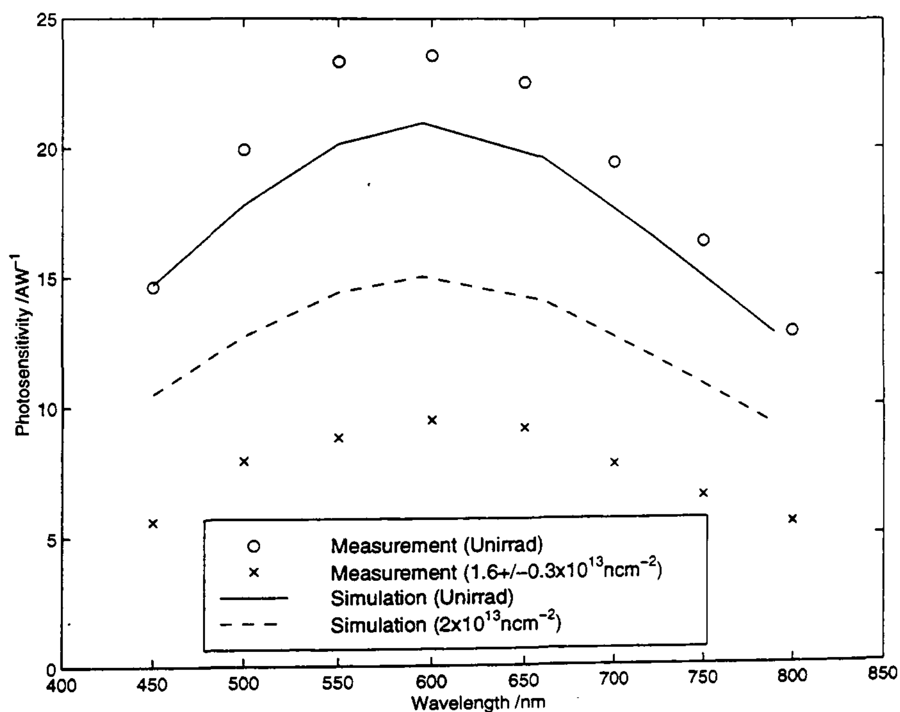

Figure 5.47: Plot showing the change in the photosensitivity measured for a C30719F APD and predicted by the reverse reach through model.

Chapter 6

Conclusions

A one-dimensional drift-diffusion simulation has been developed incorporating impact ionisation, illumination and neutron radiation damage effects. Impact ionisation is included via a term in the continuity equations. The ionisation coefficients in silicon are described using a modified form of the three parameter theory. This method has been successfully used to simulate temperature dependent effects in silicon avalanche photodiodes [93]. Illumination is accounted for using a parameterisation of the absorption coefficients in silicon, measured by Dash et al [85]. The effects of neutron irradiation damage are included via the introduction of deep acceptor levels. The occupancy of the defects is described by Shockley-Read-Hall statistics; quasi-Fermi statistics were found to cause severe convergence problems.

The simulation software was used to generate two complementary silicon avalanche photodiode models; a reach through structure and a reverse reach through structure. The predictions from the models were compared with measurements performed on two commercial silicon avalanche photodiodes; the EG&G C30916E reach through APD and the EG&G C30719F reverse reach through APD. The structures of the commercial devices were not known in detail, this proved a major hurdle, allowing only qualitative comparison with the predicted data.

The simulation allows investigation of the microscopic structure of the devices during operation, as well as providing macroscopic information. Good agreement was found between the predicted and measured behaviour under reverse bias for both

models. The 'reach through' process was described by the models; both microscopically, by the distribution of free carriers, and macroscopically from the predicted photocurrent.

Complementary methods were used to calculate the gain from the models, directly from the predicted photocurrent and indirectly from analysis of the electric field profile. This allowed the models to predict the gain that would be measured experimentally and to compare this with the multiplication factor of the devices, i.e. the actual gain experienced by a charge traversing the gain region. The use of the DC gain measurement was shown to overestimate the gain for reach through structures, as light is absorbed in an un-depleted region prior to 'reach-through'. The fall in gain at longer wavelengths, for the reverse reach through structure, was predicted by the model. This effect is caused by the absorption of light in, or beyond, the gain region. Only the electrons generated in front of the gain region are fully multiplied. This results in a fall in the measured gain, although the multiplication factor of the device is un-affected.

The excess noise factor was calculated from the models using the Mcintyre theory; measurements of the excess noise factor were achieved using the Webb method. The predicted excess noise factor compared well with the measured data, although no post-irradiation comparison was available.

The photosensitivity was calculated from the models and compared with the measured data. The reach through structure exhibits a broad spectral response, due to the wide depletion region available for the absorption of the incident light. The smaller region available in the reverse reach through structure results in a much narrower response. The simulation predicted the measured response well, for both structures.

The effects of neutron irradiation were investigated. To facilitate comparison with experimental data the C30916E and C30719F devices were irradiated at the RAL ISIS facility. The reach through APD model predicted an increase in the multiplication factor after neutron irradiation. This was not confirmed experimentally

because the method used to measure the gain could not be successfully applied to the C30916E device after irradiation. The measured photocurrent data implied a reduction in the gain after irradiation for the C30916E device. This was attributed to self-heating in the C30916E device due to the increased bulk dark current and limitations in the temperature control imposed by the C30916E packaging.

The gain of the reverse reach through model was seen to fall after neutron irradiation. The gain measured from the C30917E device showed a similar reduction. This effect has also been observed in measurements of EG&G C30626E reverse reach through avalanche photodiodes during evaluation for the CMS ECAL .

The observed shift in the gain is attributed to the presence of ionised deep acceptor levels, which alter the potential through the device; this in turn modifies the electric field profile. The gain is extremely sensitive to changes in the electric field and a small shift in the high field region, where the gain originates, will result in a significant change in the gain.

The measured photosensitivity of the C30916E and C30719F devices fell significantly after neutron irradiation. This trend was reproduced by the models, but the fall was not described completely. The gamma background during the irradiations introduced surface damage to the devices, resulting in a fall in the quantum efficiency and hence photosensitivity. Surface damage was not included in the model and hence the effects could not be completely described.

A general-purpose simulation tool has been introduced, which allows complex photodiodes to be built and tested, both before and after neutron irradiation [101],[102]. Two complementary silicon avalanche photodiode models have been compared with measured data from commercial devices with similar structures. The models showed good qualitative agreement with the measured data for a wide range of conditions. and indicated areas where further development would be beneficial. The results show that the simulation software is a useful tool in the analysis of silicon photodetectors, and could be applied to the development of future devices, especially in HEP where radiation tolerant devices are essential.

The simulation package provides an excellent platform for further development. The two primary areas of interest for expansion are, simulation of multiple spatial dimensions and the solution of the time-dependent equations. Simulation of two or three-dimensional structures would allow much more complete modelling of device behaviour including surface effects and lateral non-uniformities, which lead to *micro-plasma* formation. The solution of the time-dependent equations would allow the investigation of transient effects, e.g. the formation of avalanches as a result of particle interaction. These developments are not mutually exclusive, a multi-dimensional time-dependent simulation would be an extremely versatile tool in the analysis of avalanche photodiode behaviour.

Bibliography

[1] J Gower," Optical Communication Systems", Prentice Hall, 1993, UK

[2] S L Miller," Avalanche Breakdown in Germanium", *Phys. Rev*, **Vol. 99**, 1955, pp 1234-1241.

[3] T shima and Y Nagai," Development of a Photomultiplier Tube with high Quantum Efficiency. ", *Nucl. Instr. and Meth.*, A **431**,no.1-2, 11 July (1999), pp. 224-227.

[4] J A Correia et al ,"Development of a Small Animal PET Imaging Device with Resolution Approaching 1 mm.", *IEEE Transactions on Nuclear Science*,**Vol. 46**, no. 3, pt. 2, Jun 1999, pp. 631-635.

[5] Suzuki A et al," Improvement of 20 in. Diameter Photomultiplier Tubes. ", *Nucl. Instr. and Meth.*, A **329**,no.1-2, 15 May (1993), pp. 299-313.

[6] K D Kramer et al," An Optical MEMS-Based Fluorescence Detection Scheme with Applications to Capillary Electrophoresis.",*Proceedings of SPIE*, vol. **3515**, 1998, pp.76-85. USA.

[7] R Farrell et al," Advances in Semiconductor Photodetectors for Scintillators. ", *Nucl. Instr. and Meth.*, A **387**, (1997), pp. 194-198.

[8] K M James et al," Performance Evaluation of New Large-Area Avalanche Photodiodes for Scintillation Spectroscopy. ", *Nucl. Instr. And Meth.*, A **313**, (1992), pp. 196-202.

[9] S M Sze," Physics of Semiconductor Devices", John Wiley & Sons . USA. 1981.

[10] J Zhang et al ,"Military Avionics Optical Fiber Data Buses with Active-Coupler Configurations.", *IEEE Aerospace and Electronic Systems Magazine* ,**Vol. 14**, no. 7, July 1999, pp. 27-33.

[11] *Proceedings of SPIE*, **vol. 3000**, 1997, pp.55-59. USA.

[12] R Lecomte et al ,"Performance Characteristics of BGO-Silicon Avalanche Photodiode Detectors for PET.", *IEEE Transactions on Nuclear Science*,**Vol. NS-32**, no. 1, Feb 1985, pp. 482-6.

[13] P Cushman et al," Multi-Pixel Hybrid Photodiode Tubes for the CMS Hadron Calorimeter. ", *Nucl. Instr. and Meth.*, A **387**,no.1-2, 1 Mar, (1997), pp. 107-112.

[14] G Organtini ,"Avalanche Photodiodes for the CMS Electromagnetic Calorimeter. ", *IEEE Transactions on Nuclear Science*,**Vol. 46**, no. 3, pt. 1, Jun 1999, pp. 243-9.

[15] The CMS Collaboration, " The Electromagnetic Calorimeter Project Technical Design Report", CERN/LHCC 97-33(1997).

[16] The CMS collaboration, " The Compact Muon Solenoid letter of Intent", CERN/LHC 92-3 LHCC/I1(1992)

[17] The CMS collaboration, " The Compact Muon Solenoid Technical Proposal", CERN/LHC LHCC/9438(1994).

[18] J P Ernenwein, " Overview of the CMS Electromagnetic Calorimeter ". CMS CR/99/006.

[19] K Dieters et al," Comparison of Photomultiplier and Avalanche Photodiode Readout of $PbW0_4$. ", *Nucl. Instr. and Meth.* , A **387**, (1997), pp. 211-213.

[20] R J McIntyre, P P Webb and H Dautet," A Short Wavelength Selective Reach Through Avalanche Photodiode", *IEEE Transactions on Nuclear Science*, **Vol. 43**, June 1996, No 3, pp. 1341-1346.

[21] E Longo," Avalanche Photodiodes for the CMS Electromagnetic Calorimeter", CMS CR1998/002, 1998.

[22] J P Pansart," Avalanche Photodiodes for Particle Detection", *Nucl. Instr. and Meth.*, A **387** (1997), pp. 186-193.

[23] J Matheson, M Robbins and S J Watts," A Microscopic Explanation for Type Inversion and the Annealing Behaviour of Radiation Damaged Silicon Detectors ", BRU/PH/202, 19 May 1995.

[24] J Matheson et al," The Effect of Radiation Induced Defects on the Performance of High Resistivity Silicon Diodes", RD20/TN/36, Jan 1995.

[25] D Pusseri et al," Comprehensive modelling of Silicon Microstrip Detectors ", CMS CR/97/004, 1997.

[26] For example see M J Morant," Introduction to Semiconductor Devices", Harrap, 1970

[27] W Shockley ," The Theory of p-n Junctions in Semiconductors and p-n Junction Transistors", Bell Systems Tech. Jour. 28, 1949, p-435

[28] R N Hall, *Phys. Rev*, **Vol. 87**, 1952, p-387.

[29] W Shockley and W T Read, *Phys. Rev*, **Vol. 87**, 1952, p-835.

[30] A G Chenowyth, *Phys. Rev*, **Vol. 109**, 1958, p-1537.

[31] S M Sze and G Gibbons," Avalanche Breakdown Voltages of Abrupt and Linearly Graded p-n Junctions", *Applied Physics Letters*, **Vol. 8**, No. 5, 1966, p-111.

[32] J Conradi," The Distribution of Gains in Uniformly Multiplying Avalanche Photodiodes ", *IEEE Transactions on Electron Devices*, **Vol. 19**,Jul 1972, No. 6, pp. 713-718.

[33] P P Webb, R J McIntyre and J Conradi, " Properties of Avalanche Photodiodes", *RCA Review*, **Vol. 35**, June 1974, p-234.

[34] R J McIntyre " Multiplication Noise in uniform Avalanche Photodiodes ", *IEEE Transactions on Electron Devices*, **Vol. 13**,Jan 1966, No. 1, p-164.

[35] K Roze et al," Temperature Dependence of Impact Ionisation Co-efficients in P-Si ", *Journal of Applied Physics*, **Vol. 83**, no. 9, May 1998, p-4988.

[36] A Pacelli et al," Impact Ionisation in Silicon: A Microscopic View ", *Journal of Applied Physics*, **Vol. 83**, no. 9, May 1998, p-4760.

[37] J Y Tang and K Hess " Impact Ionisation of Electrons in Silicon(Steady State) ", *Journal of Applied Physics*, **Vol. 54**, no. 9, Sep 1983, p-5139.

[38] a good list is provided by W Meas, K DE Meyer and R Vanoverstraeten, " Impact Ionisation in Silicon: A Review and Update ", *Solid State Electronics*,**Vol. 33**, No. 6, 1990, pp 705-718.

[39] P Bhattacharya," Semiconductor Optoelectronic Devices", Prentice Hall International Editions, USA, 1994

[40] J E Bateman and R Stephenson," Charge Storage Effects in Some Avalanche Photodiodes Proposed for use in the CMS ECAL", RAL-TR-95-061, 1995

[41] N Bacchetta et al ," MRS Detectors with High Gain for Registration of Weak Visible and UV Fluxes ", *Nucl. Instr. and Meth.*, A **387**, 1997, pp. 225-230.

[42] A V Akindinov ," New Results on MRS APDs", *Nucl. Instr. and Meth.*, A **387**, 1997, pp. 231-234.

[43] EG&G Inc. 43 William Street, Wellesley, Maassachusetts. USA. www.eg+g.com .

[44] Y Benhammou ," Investigation of Avalanche Photodiodes", CMS TN/96/052, 1996.

[45] F Cavallari ," Progress on avalanche Photodiodes as Photon Detectors for $PBWO_4$ Crystals in the CMS Experiment", CMS CR/97/10, 1997

[46] E Bartolome et al, "Development of a Compact high Density Luminosity Monitor for ALEPH at LEP-II based on a Tungsten-Scintillator Calorimeter read out by Avalanche Photodiodes",*Nucl. Instr. and Meth.*, A **387**, 1997, pp. 216-219.

[47] J Troska, "Neutron, Proton and γ Radiation Effects in Candidate InGaAs Photodiodes for the CMS Tracker Optical Link", CMS TN/97/102, 1997

[48] Th. Kirn et al , " Properties of the Most Recent Hamamatsu Avalanche Photodiodes", *Nucl. Instr. and Meth.*, A **387**, 1997, pp. 199-201.

[49] B MacEvoy et al ," Defect Evolution in Silicon Detector Material",*Nucl. Instr. and Meth.*, A **388**, 1997, pp. 365-369.

[50] R Wunstorf et al, "Radiation Damage of Silicon Detectors by Mono-Energetic Neutrons and Electrons", Large Hadron Collider Workshop, v.3, Aachen, Germany, 4-9 October, 1990. (CERN 90/10 p.706)

[51] S J Watts, " Overview of Radiation Damage in Silicon Detectors - Models and Defect Engineering",*Nucl. Instr. and Meth.*, A **386**, 1997, pp. 149-155.

[52] F M Lemeilleur et al ," Electrical Properties and Charge Collection Efficiency for Neutron-Irradiated p-type and n-type Si Detectors", *Nucl. Instr. and Meth.*, B **387**, (1993), pp. 415-424.

[53] R Wunstorf et al, " Results on Radiation Hardness of Silicon Detectors up to Neutron Fluences of 10^{15}n/cm^{2}",*Nucl. Instr. and Meth.*, A **315**, 1992, pp. 149-155.

[54] K Gill, G Hall and B MacEvoy," Divacancy Clustering and the Origin of Leakage Current in Bulk Damaged Silicon Detectors ", CMS/TN/96/17, 1996.

[55] K Gill, G Hall and B MacEvoy," Bulk Damage Effects in Irradiated Silicon Detectors Due to Clustered Divacancies", CERN-PPE/97/11, Feb 1997.

[56] M Moll et al ," Comparison of Defects Produced by Fast Neutrons and ^{60}Co-gammas in High Resistivity Silicon Detectors using Deep Level Transient Spectroscopy", HH/96/01, 1996

[57] S J Watts et al," A New Model for Generation-Recombination in Silicon Depletion Regions after Neutron Irradiation", *IEEE Transactions on Nuclear Science*, **Vol. 43**,No. 6, Dec 1996.

[58] D C Imrie, "Results of Initial Tests on EG&G APDs", Internal memo, Brunel University, 10 May 1995.

[59] P R Hobson and C W Selby, " A Stabilised Blue-Violet LED for VPT Photocathode Evaluation", CMS TN/00/023, 2000.

[60] CAL Controls LTD, Bury Mead Road, Hitchin, Herts SG5 1RT,UK.

[61] see for example A Karar et al ," Investigation of Avalanche Photodiodes for EM Calorimeter at LHC", CMS TN/95/095, 1995.

[62] Canberra Industries, 800 Research Parkway, Meriden, CT 06450, USA.

[63] J P Bardet al," APD Calibrations at Saclay", CMS TN/95/077, 1995.

[64] J E Bateman et al," Gain and Noise Measurements on Two Avalanche Photodiodes Proposed for the CMS ECAL", CCL-TR-95-001, 1995.

[65] A Karar et al, "Investigation of Avalanche Properties for EM Calorimeter at LHC", CMS TN/95-135, 1995.

[66] D C Imrie, "Further Tests on APDs", Internal Memo, Brunel University, 4 June 1995.

[67] J E Bateman and R Stephenson, " The Response of Some avalanche Photodiodes To Fast Neutron Irradiation", RAL-TR-96-009, 1996.

[68] F Cavallari," Progress on Avalanche Photodiodes as photon detectors for $PbWO_4$ Crystals in the CMS Experiment", CMS CR 1997/10, 1997.

[69] P P Webb," An Intrinsic Method for the Gain and k Factor Characterisation of Silicon Photodiodes", VEO-TR-94-012, EG&G Optoelectronics, Canada.

[70] M Edwards and D R Perry," The Radiation Hardness Test Facility at RAL", RAL-90-065, 1990.

[71] J E Bateman et al," A Note on the Commissioning of the Long-Term Irradiation Facility on ISIS", CMS IN/97/031, 1997.

[72] J E Bateman et al," Fast Neutron Irradiation of Some APDs Proposed for Application in the CMS ECAL", CMS IN/98/016, 1998.

[73] D Renker et al," Neutron Irradiation Damage of APDs Using ^{252}Cf",*Nucl. Instr. and Meth.*, A **394**, (1997), pp. 199-210.

[74] D Renker et al," Neutron Irradiation Studies of Avalanche Photodiodes using Californium 252", *Nucl. Instr. and Meth.*, A **387**, (1993), pp. 214.

[75] A Spinelli and A Lacaita," Physics and Numerical Simulation of Single Photon Avalanche Photodiodes", *IEEE Transactions on Electron Devices*, Vol. 44, No. 11, Nov 1997.

[76] M Valdinoci et al," Analysis of Conductivity Degradation in Gold/Platinum Doped Silicon", *IEEE Transactions on Electron Devices*, **Vol. 43**,No. 12,Dec 1996.

[77] D Passeri, M Baroncini and P Ciampolini," TCAD-Based Analysis of Radiation Hardness in Silicon Detectors", CMS CR/98/011, 1998.

[78] W H Kent ," Charge Distribution in Buried-Channel Charge-Coupled Devices",Bell Systems Tech. Jour. 52,No. 6, July 1973.

[79] M Kurata," Numerical Analysis for Semiconductor Devices",Lexington Books, USA, 1985.

[80] D L Scharfetter and H K Gummel," Large Signal Analysis of a Silicon Read Diode Oscillator", *IEEE Transactions on Electron Devices*,**Vol. 16**, Jan 1969, pp. 64-77.

[81] P L Devries, "A First Course in Computational Physics", John Wiley and Sons Inc., USA, 1994.

[82] C R Crowell and S M Sze," Temperature Dependence of Avalanche Multiplication in Semiconductors", *Applied Physics Letters*, **Vol.** 9, 1966, pp. 242-244.

[83] G A Baraff," Distribution Functions and Ionisation Rates for Hot Electrons in Semiconductors", *Phys. Rev*, **Vol. 128**, 1962, pp. 2507-2517.

[84] C A Lee, R A Logan et al," Ionisation Rates of Electrons and Holes in Silicon", *Phys. Rev*, **Vol. 134**, 1964, A761-A773.

[85] W C Dash and R Newman," Intrinsic Optical Absorption in Single Crystal Germanium and Silicon at 77K and 300K", *Phys. Rev*, **Vol. 99**, 1955, pp. 1151-1157.

[86] J Matheson, M S Robbins, S J Watts," The Effect of Radiation Induced Defects on the Performance of High Resistivity Silicon Diodes", *Nucl. Instr. and Meth.*, A **377** (1996), pp. 224-227.

[87] J Matheson et al," A Microscopic Explanation for Type inversion and the Annealing behaviour of Radiation Damaged Silicon Detectors", *Nucl. Instr. and Meth.*, A **371** (1996), pp. 575-577

[88] B C MacEvoy, G Hall and K Gill," Defect Evolution in Irradiated Silicon Detector Material",*Nucl. Instr. and Meth.*, A **374** (1996), pp. 12-26.

[89] G Messenger," A Two Level Model for Lifetime Reduction Processes in Neutron Irradiated Silicon and Germanium", *IEEE Transactions on Nuclear Science*, **Vol. 14**,Dec 1967, No. 6, pp. 88-102.

[90] S M Sze," Semiconductor Devices and Physics", John Wiley & Sons , USA, 1985.

[91] B Tuck," Introduction to Diffusion in Semiconductors", Peter Pereguinus Ltd, UK, 1974

[92] A D Sutherland," An improved Fit to Baraff's Universal Curves for the Ionisation Coefficients of Electron and Hole Multiplication in Semiconductors", *IEEE Transactions on Electron Devices*, **Vol. 27**,Jul 1980, No. 7, pp. 1299-1301.

[93] J Conradi,"Temperature Effects in Silicon Avalanche Photodiodes", *Solid State Electronics*,**Vol. 17**, 1974,pp 705-718.

[94] H W Reugg," An Optimised Avalanche Photodiode", *IEEE Transactions on Electron Devices*, **Vol. 14**, No. 5, May 1967.

[95] T Kanada et al," Excess Noise in Silicon Avalanche Photodiodes", *Journal of Applied Physics*, **Vol. 47**, 1996, pp. 1605-1607.

[96] T Kirn et al," Wavelength dependence of avalanche photodiode (APD) Parameters",*Nucl. Instr. and Meth.*, A **387** (1997), pp. 202-204.

[97] T Angelescu," Radiation Hardness Studies on Silicon Detectors in Fast Neutron Fields",*Nucl. Instr. and Meth.*, A **357** (1995), pp. 55-63.

[98] T Angelescu and A Vasilesu," Comparative Radiation Hardness Results Obtained from Various Neutron Sources and the NIEL Problem", *Nucl. Instr. and Meth.*, A **374** (1996), pp. 85-90.

[99] W C Cooley and R J Janda," Handbook of Space-Radiation Effects in Solar-Cell Power Systems", NASA SP-3003, 1963.

[100] S Baccaro," Radiation Damage Effect on Avalanche Photodiodes", CMS CR/98/10, 1998.

[101] M Osborne et al, " A Device Model Simulation of Neutron Radiation Effects in Avalanche Photodiodes", CMS TN/99/005, 1999

[102] M Osborne et al, " Numerical Simulation of Neutron Radiation Effects in Avalanche Photodiodes", *IEEE Transactions on Electron Devices*, **Vol. 47**, 2000, pp. 529-536

Appendix A

The method employed to solve the Poisson and continuity equations ensures that the equations are fully coupled, the solution to the equations is provided simultaneously using equation (4.15), where A,B and C represent 3×3 matrices. The individual cells are listed here.

$$a_{11} = -\frac{1}{qh'(N)}\frac{\delta J_p^0(M-1)}{\delta p(N-1)} - \frac{\delta G^0(N)}{\delta p(N-1)} \tag{A.1}$$

$$a_{12} = -\frac{\delta G^0(N)}{\delta n(N-1)} \tag{A.2}$$

$$a_{13} = -\frac{1}{qh'(N)}\frac{\delta J_p^0(M-1)}{\delta \psi(N-1)} - \frac{\delta G^0(N)}{\delta \psi(N-1)} \tag{A.3}$$

$$a_{21} = \frac{\delta G^0(N)}{\delta p(N-1)} \tag{A.4}$$

$$a_{22} = -\frac{1}{qh'(N)}\frac{\delta J_n^0(M-1)}{\delta n(N-1)} - \frac{\delta G^0(N)}{\delta n(N-1)} \tag{A.5}$$

$$a_{23} = -\frac{1}{qh'(N)}\frac{\delta J_n^0(M-1)}{\delta \psi(N-1)} + \frac{\delta G^0(N)}{\delta \psi(N-1)} \tag{A.6}$$

$$a_{31} = 0 \tag{A.7}$$

$$a_{32} = 0 \tag{A.8}$$

$$a_{33} = \frac{1}{h(M)h'(N)} \tag{A.9}$$

$$b_{11} = \frac{1}{qh'(N)} \left[\frac{\delta J_p^0(M)}{\delta p(N)} - \frac{\delta J_p^0(M-1)}{\delta p(N)} \right] - \frac{\delta G^0(N)}{\delta p(N)} + \frac{\delta U^0(N)}{\delta p(N)} \tag{A.10}$$

$$b_{12} = -\frac{\delta G^0(N)}{\delta n(N)} + \frac{\delta U^0(N)}{\delta n(N)} \tag{A.11}$$

$$b_{13} = \frac{1}{qh'(N)} \left[\frac{\delta J_p^0(M)}{\delta \psi(N)} - \frac{\delta J_p^0(M-1)}{\delta \psi(N)} \right] - \frac{\delta G^0(N)}{\delta \psi(N)} \tag{A.12}$$

$$b_{21} = -\frac{\delta G^0(N)}{\delta p(N)} - \frac{\delta U^0(N)}{\delta p(N)} \tag{A.13}$$

$$b_{22} = \frac{1}{qh'(N)} \left[\frac{\delta J_n^0(M)}{\delta n(N)} - \frac{\delta J_n^0(M-1)}{\delta n(N)} \right] + \frac{\delta G^0(N)}{\delta n(N)} - \frac{\delta U^0(N)}{\delta n(N)} \tag{A.14}$$

$$b_{23} = \frac{1}{qh'(N)} \left[\frac{\delta J_n^0(M)}{\delta \psi(N)} - \frac{\delta J_n^0(M-1)}{\delta \psi(N)} \right] + \frac{\delta G^0(N)}{\delta \psi(N)} \tag{A.15}$$

$$b_{31} = \frac{q}{\epsilon} \tag{A.16}$$

$$b_{32} = -\frac{q}{\epsilon} \tag{A.17}$$

$$b_{33} = -\frac{1}{h'(N)}\left[\frac{1}{h(M-1)} + \frac{1}{h(M)}\right] \tag{A.18}$$

$$c_{11} = -\frac{1}{qh'(N)}\frac{\delta J_p^0(M)}{\delta p(N+1)} - \frac{\delta G^0(N)}{\delta p(N+1)} \tag{A.19}$$

$$c_{12} = -\frac{\delta G^0(N)}{\delta n(N+1)} \tag{A.20}$$

$$c_{13} = -\frac{1}{qh'(N)}\frac{\delta J_p^0(M)}{\delta \psi(N+1)} - \frac{\delta G^0(N)}{\delta \psi(N+1)} \tag{A.21}$$

$$c_{21} = \frac{\delta G^0(N)}{\delta p(N+1)} \tag{A.22}$$

$$c_{22} = -\frac{1}{qh'(N)}\frac{\delta J_n^0(M)}{\delta n(N+1)} - \frac{\delta G^0(N)}{\delta n(N+1)} \tag{A.23}$$

$$c_{23} = -\frac{1}{qh'(N)}\frac{\delta J_n^0(M)}{\delta \psi(N+1)} + \frac{\delta G^0(N)}{\delta \psi(N+1)} \tag{A.24}$$

$$c_{31} = 0 \tag{A.25}$$

$$c_{32} = 0 \tag{A.26}$$

$$c_{33} = \frac{1}{h(M)h'(N)} \tag{A.27}$$

Where J^0 represents the currenty density term (e.g. equation 4.8), G^0 the generation term for impact ionisation (equation 4.33) and U^0 the Shockley-Read-Hall thermal generation-recombination term (equation 2.35).

Appendix B

The simulation was written using Fortran 77; a DIGITAL Fortran 77 compiler was used which generated object files in DIGITAL UNIX Alpha extended coff format. No external libraries were required, all matrix manipulation was included in the code. A series of optimisations were available from the compiler including; software pipelining, loop transformation optimisation and byte-vectorisation. These were implemented, via the switch '-05', to maximise the efficiency of the code, although no tests were performed to verify any improvement.

Generation and investigation of a particular model is simple, involving only the creation of two ASCII files of parameters. To *build* a device using the DIFFUSE code a file with the following parameters is required:

- total device depth in cm, e.g. 100×10^{-4}
- depth junction required in cm, e.g. 3×10^{-4}
- area of device in cm^2, e.g. 0.25
- depth of first acceptor dopant in cm, e.g. 17.5×10^{-4}
- first acceptor dopant concentration (peak) in cm^{-3}, e.g. 1.4×10^{16}
- depth of donor dopant in cm, e.g. 5×10^{-4}
- donor dopant concentration (peak) in cm^{-3}, e.g. 7.4×10^{17}
- flag for second acceptor dopant (0/1)

- second acceptor dopant concentration (peak) in cm^{-3} if required
- depth of second acceptor dopant in cm if required
- level of substrate doping in cm^{-3}, e.g 2.5×10^{12}
- filename of output file.

Once the doping profile is created then this is copied into the same directory as the APDSIM executable. Another ASCII file is required to set the run parameters for APDSIM, these are shown below:

- temperature in Kelvin, e.g. 300
- initial bias in V, e.g. 1
- final bias in V, e.g. 400
- calculation bias step size typically 1V
- output file bias step size i.e. number of calculation steps between storage e.g. 10
- initial neutron fluence in ncm^{-2}, e.g. 1×10^{13}
- final neutron fluence in ncm^{-2}, e.g. 5×10^{13}
- calculation fluence step size in ncm^{-2}, e.g. 1×10^{13}
- energy level of deep donor (below conduction band) in eV, e.g. 0.5
- energy level of deep acceptor (below conduction band) in eV, e.g. 0.5
- ratio of capture co-efficients for deep donor, e.g. 1
- ratio of capture co-efficients for deep acceptor, e.g. 1
- donor introduction rate in cm^{-1}, e.g. 0.96

- acceptor introduction rate in cm^{-1}, e.g. 0.96
- number of steps before non-convergence, e.g. 250
- residual, e.g. 5×10^{-9}
- unirradiated minority carrier lifetime in s, e.g. 100×10^{-6}
- wavelength of incident light in s, e.g. 100×10^{-6}
- photon flux in $cm^{-2}s^{-1}$, e.g. 5×10^{11}
- side device illuminated from (L)eft/(R)ight
- flag to switch impact ionisation on/off
- flag to switch Auger recombination on/off

The multiplication factor and the excess noise factor, evaluated using APDGAIN, did not require a run-file as the code was interactive.

Appendix C

$\alpha_{e/h}$ - electron/hole ionisation co-efficient.

β - optical absorption co-efficient.

c - speed of light in a vacuum.

$C_{n/p}$ - electron/hole capture rate.

δ - secondary electron co-efficient.

$D_{n/p}$ - electron/hole diffusivity constant.

$e_{n/p}$ - electron/hole emission rate.

ϵ_i - activation energy.

ε_o - permittivity of free space.

ε_r - mean energy loss per phonon collision.

E_c - conduction band energy.

E_i - intrinsic Fermi energy level.

E_g - bandgap energy.

E_v - valence band energy.

$f(E)$ - Fermi function at energy E.

F - excess noise factor.

Φ_n - neutron fluence.

G - Generation rate.

Γ - $N_d - N_a$

h - Planck constant.

η - external quantum efficiency.

ψ - potential.

$J_{n/p}$ - electron/hole current density.

k_τ - lifetime damage constant.

λ - wavelength.

$\lambda_{n/p}$ - electron/hole optical phonon mean free path

$M_{e/h}$ - electron/hole multiplication factor.

n - free electron concentration.

n_i - intrinsic carrier concentration

$\mu_{n/p}$ - electron/hole mobility.

$N_{d/a}$ - ionised donor/acceptor concentration.

$\sum N_{D/A}$ - ionised deep donor/acceptor concentration.

N_T - trap density

p - free hole concentration.

q - electronic charge.

ρ - charge density.

U - recombination rate.

$\sigma_{n/p}$ - electron/hole capture cross section.

$\tau_{n/p}$ - electron/hole minority carrier lifetime.

T - absolute temperature.

v_{th} - thermal velocity.

ν - frequency of EM wave.